Sensitivity and Accuracy Limits of Molecular Imaging in Fluorescence Guided Surgery



A dissertation presented for the degree of Master of Science (By Research)

By

Sam Fry

Nuffield Department of Surgical Sciences

University of Oxford

College

Christ Church

Supervisors

Professor Borivoj Vojnovic

Professor Freddie Hamdy

Michaelmas Term 2020



Covid-19 Mitigation Statement

The Covid-19 pandemic (2020) has prevented access to the lab facilities in which I have been working. In light of this, work planned for contribution to this dissertation could not be completed since it required physical access to said lab facilities. This statement has therefore been written in line with departmental advice to summarise work that was planned during this period.

The first piece of work impacted by the pandemic was in contribution to the FGS calibrator project as detailed in Chapter 2. This work involved an experiment to demonstrate the function of the FGS calibrator detector module by measuring the detection limits of an in-house developed FGS imager. The experiment aimed to quantify the detection limits (sensitivity) of the in-house developed FGS imager at various wavelengths. This experiment had been conducted shortly before the Covid-19 lockdown. However, it was realised afterwards that I could not present the data obtained from this experiment due to discrepancies in the images acquired during the initial experiment. Therefore, it was planned that the experiment would be repeated to reobtain the images, although this was not possible due to Covid-19 restrictions. For more information, the details of the experimental method has been described in the data section of Chapter 2 in place of the originally acquired images to provide specifics of how the data can be acquired.

Furthermore, as a result of the pandemic, the *ex-vivo* imager, discussed in Chapter 3, could not be developed further since this again required access to the lab. Work planned for this period involved developing a working first prototype of the *ex-vivo* imager and initial testing of the device before commencing pre-clinical and clinical work with the imager. As a result of being unable to progress the project further,

Chapter 3 provides datils of the work completed up to the point at which the Covid-19 lockdown was first put in place detailing the design considerations that contributed to the development of the *ex-vivo* imager.

Abstract

Fluorescence guided surgery (FGS) is an emerging imaging modality seeking to improve optical contrast in the near infrared (NIR). FGS offers real time imaging capabilities to help surgeons identify tissues of interest with higher precision and specificity during surgery. The increased contrast is provided by fluorescence emission from non-specific or specific fluorescent markers.

Many commercial imagers have been developed for FGS, with several achieving FDA approval for clinical use. However, little information is available regarding absolute sensitivity of the detection systems or amount of excitation light produced in physical units. In light of this, attempts have been made to formulate a calibration standard. Previously published calibration methods have involved the use of composite phantoms, which require chemical preparation, may suffer from inner filter effects* and have a limited shelf life. This work outlines a new electronic calibration device for FGS, consisting of a light emitting module and a light detection module. Their purpose is to measure the detection sensitivity to NIR photons for various NIR wavelengths (in SI units of photons/s/cm^2) and to measure the excitation light available as a function of working distance (in SI units of mW/cm^2).

The second part of this work is concerned with the development of a novel *ex-vivo* FGS imager. This *ex-vivo* imager seeks to potentially improve outcomes of FGS surgical procedures by evaluating surgical margins following tissue resection. This will help the surgeon to quickly determine whether further surgery is needed.

* Inner filter effects involve the process of absorption of fluorescence emission within the composite phantom following excitation by the FGS imager being calibrated.

The *ex-vivo* imager uses a custom designed excitation light source to maximise fluorophore excitation at numerous wavelengths and employs a low readout noise chilled NIR-sensitive camera. Furthermore, spectral unmixing approaches may be explored to remove confounding autofluorescence signals. These features of the imager are designed to maximise imaging contrast and tumour-to-background ratio.

Contents

Acknowledgments 1
List of Figures 2
List of Tables 12
List of Abbreviations 14
List of Symbols 16
Introduction 18
Project Aims 20
1. Background 22
1.1 An Overview of Imaging Techniques in Surgery and Oncology 22
1.1.1 Conventional Imaging Techniques 22
1.1.2 Molecular and Functional Imaging 26
1.1.3 Optical Imaging 31
1.2 Fluorescence Guided Surgery 36
1.2.1 Markers Used for FGS Imaging 40
1.2.2 FGS Imaging Technology 44
2. FGS Calibrator 50
2.1 Introduction 50
2.2 FGS Calibrator Design 52
2.2.1 Detector Module Design 52
2.2.2 Emitter Module Design 57
2.2.3 Control Module and Software Design 61
2.3 Calibration of the LED Emitter 68
2.4 FGS Calibrator Testing 70
2.4.1 Detector Module Sensitivity Calibration 70
2.4.2 LED Emitter Module Testing and Calibration 72
2.5 Calibration of an in-house Developed FGS Imager 81
2.5.1 Excitation Calibration 81
2.5.2 Sensitivity Calibration 83
2.6 Chapter 2 Summary 88
3. *Ex-vivo* Imager 89
3.1 Introduction 89
3.2 Initial Illuminator Design 94
3.3 Towards a Laser Diode Excitation Illumination System 103
3.3.1 Laser Fibre Coupling 106
3.3.2 Homogenisation and Beam Shaping 108

3.3.3 Additional Details 118
3.4 CCD Camera and NIR Lens 120
3.5 Filtering 122
3.6 Spectral Unmixing 127
3.7 Experimental Testing Results 129
3.7.1 Camera Performance Testing 129
3.7.2 LED Array Experiments 133
3.7.3 Illuminator Testing 135
3.8 Chapter 3 Summary 137
4. Conclusion 141
Additional Information 145
Appendices 146
References 157

Acknowledgments

Firstly, I would like to thank my supervisors Professor Borivoj (Boris) Vojnovic and Professor Freddie Hamdy for giving me the opportunity to work in what I believe to be an important area of science. Their enthusiasm for science and much needed help when times have been difficult has been crucial in helping me to complete the work detailed in this dissertation. I also extend my thanks to Cancer Research UK (CRUK) for providing the crucial funding for this work. I also wish to acknowledge the patients that have participated in the FGS work that is supported by CRUK; without the patients' consents none of this work could be done.

Furthermore, I wish to extend my thanks to colleagues in the Advanced Technology Development Group of the Department of Oncology. Particular thanks go to Iain Tullis for all of his help with the technical aspects of the work and for his useful suggestions. Furthermore, many an interesting lunchtime discussion took place regarding all manner of obscure subjects that has taught me a great deal.

I would like to thank all of the staff in the Department of Oncology workshop: John Prentice, Gerry Shortland and Kyle Hallett for fabricating the various mechanical parts required for my project. Particular thanks also go to Robert Newman for all of his help with various aspects of the electronics required in the devices discussed in this dissertation, his considerable expertise regarding electronics and firmware has been invaluable.

Finally, I thank my friends and family for keeping me going and believing in my capabilities. I wish to dedicate this work to them.

List of Figures

Figure 1: Image from (Hemmer, E. *et al*. 2016). *Top*: Optical loss coefficient for human skin including both scattering and absorption for all three near infrared windows. *Bottom*: Effective attenuation coefficient for whole blood, skin and fat as a function of wavelength, note the minima at near infrared wavelengths. 32

Figure 2: *Left*: Fluorescence Guided Surgery (FGS) for open surgery (image adapted from Vahrmeijer, A. L., *et al*., 2013). *Right*: FGS for laparoscopic (keyhole) surgery reproduced from Long Island Surgery, P. C., 2015 (from http://www.longislandsurgery.org/laparoscopic.html). 37

Figure 3: Jablonski diagram for a single fluorescence cycle reproduced from Llères, D., Swift, S., and Lamond, A. I. (2007). Upon absorption of a photon the ground state electron transitions to the excited state, this process takes femtoseconds. Following excitation, the electron loses energy over time as a result of non-radiative transitions in the excited state. The mean time spent in the excited state is the fluorescence lifetime, this timescale can vary between fluorophores from picoseconds to nanoseconds (the environment may also affect the fluorescence lifetime)..... 38

Figure 4: ICG spectra for absorption and fluorescence emission reproduced from Topaloglu, N., Gulsoy, M., and Yuksel, S. (2013). The shift between the two spectra is the Stokes shift for ICG..... 39

Figure 5: Completed photodiode detector module..... 53

Figure 6: Calibrated responsivity spectrum of the FDS100-CAL, provided by Thorlabs® for the specific device used. 54

Figure 7: Block diagram demonstrating how the detector works as a current to voltage convertor to measure the light level incident on the photodiode. A 10^6:1 dynamic range is achieved through 16:1 feedback resistances in the transimpedance amplifier circuit. The output signal is digitised using a 16-bit analogue-to-digital convertor (ADC) in the control module (described later)..... 55

Figure 8: Simplified block diagram demonstrating the key internal components of the LED emitter module, designed to ensure linearity of the LED light output with increasing setpoint input. 58

Figure 9: Schematic demonstrating how the case of the emitter allows for the insertion of diffusive optics into a mount situated above the LED. The above layout of optical components is merely an example of what may be used, although any number or combination of filters and diffusive optics may be placed in front of the LED depending on the needs of the system. By introducing these optics after the LED, the emission becomes quasi-hemi-isotropic ensuring that the emission intensity does not vary as a function of angle. 60

Figure 10: *Left*: The completed emitter module (of dimensions: 55 mm × 81.5 mm). *Right*: LED driver circuit board with feedback photodiode and thermometer. The feedback photodiode monitors the LED output and compares it to the user defined setpoint to ensure that the brightness can be varied in a linear manner..... 60

Figure 11: Block diagram demonstrating the interface between the host PC and the calibrated photodiode detector module and LED emitter module..... 61

Figure 12: The completed control module connected to the measurement modules.61

Figure 13: Front panel of the graphical user interface of the FGS calibrator software (operated from the host PC). 64

Figure 14: Emitter calibration setup (schematic). The detector module is attached to the emitter module with the diffusive optics in place and the detector calculates the intensity at various LED outputs to determine the photon flux produced by the LED module at a certain working distance (in this case 57 mm). 68

Figure 15: Plots used to determine the FGS calibrator detector module output voltage ratios between adjacent sensitivity ratings (see Table 3), the error bars denote the standard deviation in *x* and *y* (the error in *y* is not visible on this scale), with each reading being generated by the mean of 5 measurements. *Top left*: Plot used to determine the ratio between sensitivity range 6 and range 5. *Top right*: Plot used to determine the ratio between sensitivity range 5 and range 4. *Middle left*: Plot used to determine the ratio between sensitivity range 4 and range 3. *Middle right*: Plot used to determine the ratio between sensitivity range 3 and range 2. *Bottom left*: Plot used to determine the ratio between sensitivity range 2 and range 1. Note: The scale on the bottom left plot is different from the other plots since the emitter module could not produce enough light to use the full dynamic range at these sensitivities. 71

Figure 16: *Top*: Photodiode output signal voltage as a function of the LED setpoint voltage for 690 nm LED in linear space. *Middle*: Photodiode output signal voltage as a function of the LED setpoint voltage for 780 nm LED in linear space. *Bottom*: Photodiode output signal voltage as a function of the LED setpoint voltage for 880 nm LED in linear space. Note: The error bars are defined by the standard deviation, with each reading being generated by the mean of 5 measurements. 74

Figure 17: *Top*: Photodiode output signal voltage as a function of the LED setpoint voltage for 690 nm LED in log-log space. *Middle*: Photodiode output signal voltage as a function of the LED setpoint voltage for 780 nm LED in log-log space. *Bottom*: Photodiode output signal voltage as a function of the LED setpoint voltage for 880 nm LED in log-log space. Note: the error bars have been omitted from these plots to make it easier for the reader to see the data points. 75

Figure 18: *Top*: 690 nm LED non-linearity calculated as the percentage difference from the ideal linear fit. *Middle*: 780 nm LED non-linearity calculated as the percentage difference from the ideal linear fit. *Bottom*: 880 nm LED non-linearity calculated as the percentage difference from the ideal linear fit. Note: The error bars are defined by the standard deviation, with each reading being generated by the mean of 5 measurements. 77

Figure 19: *Top*: Photon flux as a function of LED setpoint input voltage for 690 nm LED. *Middle*: Photon flux as a function of LED setpoint input voltage for 780 nm LED. *Bottom*: Photon flux as a function of LED setpoint input voltage for 880 nm LED. Note: The error bars are defined by the standard deviation, with each reading being generated by the mean of 5 measurements. 79

Figure 20: Measurement setup for characterisation of an FGS imager excitation beam (set to a wavelength of 660 nm). 81

Figure 21: *Top*: Power density as a function of working distance for the excitation system of an in-house developed FGS imager. *Bottom*: Power density as a function of $1/d^2$ for the excitation system of an in-house developed FGS imager. Note: The error bars in *x* are determined from the error in the precision in the rule used to

measure working distance, the errors in *y* are defined by the standard deviation with each reading being generated by the mean of 5 measurements. The noise floor has not been included as the detector module can detect power densities much lower than would be visible on the sale of the above plots. 82

Figure 22: Measurement setup for the calibration of the FGS imager sensitivity to fluorescence emission (not to scale). The working distance is matched to that of the calibration of the LED emitter module using the detector described earlier. 84

Figure 23: Main components that constitute the *ex-vivo* imager, shown from the side of the "short" axis of the excitation beam illumination. 92

Figure 24: LED package available from Roithner GmbH, initially chosen as the light source for the excitation system/illuminator. This LED package, part of the SMB1N Series (http://www.roithner-laser.com/led_highsingle_smd.html) was chosen for its narrow emission angle. This is compared to the other available LED packages not supplied with a lens, that exhibit much wider-angle emission profiles. Wider angle emission profiles are not desirable as they would require much more involved optics designs to maximise light collection for small area illumination. 95

Figure 25: *Top*: LED model developed in Zemax from the manufacturer's data sheet (from Roithner Lasertechnik GmbH); *Bottom Left*: Relative radiant intensity as a function of angle for the LED as measured by the manufacturer; *Bottom Right*: Relative radiant intensity as a function of angle for the LED model as measured with an angular distribution detector in Zemax. 96

Figure 26: Rectangular arrangement of LEDs designed to achieve a rectangular emission profile. The 6 mm dimension is the minimum distance that this type of LED can be separated by when mounted. 98

Figure 27: Zemax model consisting of a 2 × 3 array of LEDS based on the model in Figure 23 and a single common lens (of focal length 160 mm) placed 55 mm from the LED array (not to scale). The distance from the lens to the screen is 600 mm. .. 99

Figure 28: Results of simulations in Zemax. *Upper left*: Illumination profile produced by the 6 LED array with a 160 mm focal length lens (of diameter 40 mm) placed at a distance of 55 mm away from the LED array. *Upper right*: Illumination profile produced by the 6-LED array with an 80 mm focal length lens (of diameter 40 mm) placed at a distance of 20 mm away from the LED array. *Bottom left*: Power density at the screen as a function of the horizontal distance from the centre of screen for the profile produced in the upper left of the figure. *Bottom right*: Power density at the screen as a function of the horizontal distance from the centre of screen for the profile produced in the upper right of the figure. 99

Figure 29: Radiation characteristics of several LEDs, of wavelengths: 690 nm (*top left*), 760 nm (*top right*), 810 nm (*bottom left*) and 830 nm (*bottom right*)..... 101

Figure 30: Exploded view of the *ex-vivo* imager light source, produced in Solid Works®. The output of each individual laser diode (LD) is brought together with the outputs of the other laser diodes in a 7-to-1 optical fibre. 104

Figure 31: 400 µm 7-to-1 optical fibre from Thorlabs. 104

Figure 32: 2.5 × 2.5 mm^2 input face, 100 mm length, 5 × 5 mm^2 output face trapezoidal light guide. 105

Figure 33: Optical setup of the excitation illuminator system. 105

Figure 34: Laser diode-optical fibre coupling optical arrangement with lens spacings labelled. The design was developed in Zemax as with other optical designs include in this dissertation. 108

Figure 35: Results of Zemax simulations to qualitatively assess the homogenisation introduced by two different tapered light pipes. *Upper panels/plots*: Homogenisation induced by a 50 mm length tapered light guide. *Lower panels/plots*: Homogenisation induced by a100 mm length tapered light guide. Both tapered light guides possess 2.5 × 2.5 mm^2 input and 5 × 5 mm^2 output faces. *Top patterns*: The particular fibre output switched on for the simulation. The laser wavelength used in these particular simulations was 750 nm. Other wavelengths result in similar output patterns. The light pipe geometry is depicted at the top. 110

Figure 36: Zemax model setup to stretch 5 × 5 mm^2 beam into a 90 × 90 mm^2 illumination beam at the screen. 112

Figure 37: Performance of system with a single 30 mm focal length lens, resulting in a 90 × 90 mm^2 illumination field. *Left*: working distance = 575 mm; *middle*: working distance = 590 mm; *right*: working distance = 605 mm. Bottom plots show field flatness at the various working distances. 114

Figure 38: Diagonal beam profiles to accompany the horizontal beam profiles included at the bottom of Figure 37. By including the diagonal and horizontal beam profiles it provides a more complete picture of beam flatness. 114

Figure 39: Zemax model setup to stretch 5 × 5 mm^2 beam into a 120 × 90 mm^2 illumination beam at the screen by adding a cylindrical lens. Both lens are treated as a combined lens of focal length f_C. 115

Figure 40: Performance of system with spherical and cylindrical lenses, resulting in a 120 × 90 mm^2 illumination field. *Left*: working distance = 575 mm; *middle*: working distance = 590 mm; *right*: working distance = 605 mm. *Bottom*: plots show field flatness at the various working distances. 117

Figure 41: Diagonal beam profiles to accompany the horizontal beam profiles included at the bottom of Figure 40. 117

Figure 42: Outline of the design of the excitation illuminator system. 118

Figure 43: Optical layout designed to achieve a 16:9 aspect ratio. 118

Figure 44: Beam shape at the screen. 119

Figure 45: *Left*: Beam profile in the horizontal direction. *Right*: Beam profile in the diagonal direction. 119

Figure 46: Data for the graphs are provided by Semrock (filters), RPMC Lasers Inc. and LDX Optronics Inc. (lasers). *Top Left*: 645 nm laser filtering; *Top Right*: 690 nm laser filtering; *Middle Left*: 750 nm laser filtering; *Middle Right*: 780 nm laser filtering; *Bottom Left*: 808 nm laser filtering. Indicated on each graph are the nominal laser emission wavelengths (black arrow), the laser bandwidths (orange box) and the laser tolerances (blue box). 123

Figure 47: Data for the graphs are provided by Semrock (filters), RPMC Lasers Inc. and LDX Optronics Inc. (lasers). *Top Left*: 645 nm laser filtering in OD space; *Top Right*: 690 nm laser filtering; *Middle Left*: 750 nm laser filtering in OD space; *Middle*

Right: 780 nm laser filtering in OD space; *Bottom Left*: 808 nm laser filtering in OD space. Indicated on each graph are the nominal laser emission wavelengths (black arrow), the laser bandwidths (orange box) and the laser tolerances (blue box). 124

Figure 48: Filter wheel used to select different filters for the emission channel of the *ex-vivo* imager to accommodate for switching of excitation wavelength during imaging. 125

Figure 49: Data for the graphs are provided by Semrock. *Top Left*: 645 nm laser emission filtering; *Top Right*: 690 nm laser emission filtering; *Middle Left*: 750 nm laser emission filtering; *Middle Right*: 780 nm laser emission filtering; *Bottom Left*: 808 nm laser emission filtering..... 126

Figure 50: Experimental setup to measure the conversion gain of the camera. A 690 nm LED was used as the light source, a variable current supply enabled a range of outputs from the LED. A diffuser located in front of the CCD chip ensures that even illumination of the CCD chip can be achieved. 131

Figure 51: Variance as a function of the mean signal for an exposure of 2 ms calculated in ImageJ from images acquired with the Starlight Xpress CCD camera. 132

Figure 52: Experimental setup for LED experiments. The LED could be adjusted in the *x* (side to side) and *y* (up and down) directions. The screen was a paper sheet and was imaged by the camera. The camera is placed at a distance of 900 mm from the screen and positioned at a slight angle to the LED-screen optical axis to prevent the LED mount from appearing in the field of view. A 1˚ diffuser was introduced to the setup to scatter the LED output, as it was discovered that the LED chip bonding

wires were being brought into focus at the screen, causing unwanted shadows adding to uneven illumination profiles. A neutral density filter (OD = 2, nominal) was also added to reduce the intensity of the LED beam to avoid camera saturation. 133

Figure 53: Composite images produced in the image processing software ImageJ demonstrating how LED outputs combine to produce a beam profile at the screen. 134

Figure 54: Beam pattern achieved for a working distance of 600 mm. Note: the dark patch in the top left hand corner is due to the trapezoidal light pipe becoming chipped during testing, the replacement part is to be tested with the rest of the device. The test here was conducted merely as proof of principle. 136

Figure 55: NA of an arbitrary plano-convex lens. 150

Figure 56: Geometry of the used to define the étendue of a ray traversing a medium of refractive index, *n*. The vector $\mathbf{n}_A$ defines the normal to the element of area denoted by δA. 152

Figure 57: *Top*: Circuit diagram of a forward biased LED. *Bottom*: LED p-n junction. 154

List of Tables

Table 1: Summary of key clinical imaging techniques employed in medical imaging and cancer diagnosis and treatment. Data included in this table is collated from James and Gambhir (2012) and Vandenberghe, S, *et al*. (2016). The resolutions for clinical imaging and pre-clinical imaging are quoted separately as in many cases the achievable resolution is higher in pre-clinical imaging. 29

Table 2: Firmware data sampling and communication schedule in the PIC of the control module. 63

Table 3: Output ratios between each range, used to calculate the sensitivity in A/V for each sensitivity range. 72

Table 4: LEDs used in the emitter module of the FGS calibrator during calibration of the emitter and their maximum current ratings as well as the maximum currents the LEDs were operated at. 73

Table 5: LED setpoint voltage to current conversion coefficients for each LED, calculated from the graphical data in Figure 16. 76

Table 6: LED setpoint voltage to photon flux conversion coefficients for each LED, calculated from the graphical data in Figure 19. 80

Table 7: Fluorophores being investigated using the first iteration of the *ex-vivo* imager, including the wavelengths selected for excitation. 90

Table 8: Laser diodes to be used in the *ex-vivo* imager excitation system. The data in this table is supplied by RPMC lasers Inc. and LDX Optronics Inc. 103

Table 9: Total noise calculated for the FGS calibrator detector module according to the Burr-Brown note describing the process of analysing the noise produced in a transimpedance amplifier circuit. 148

Table 10: Equivalent input flux of photons needed to achieve a signal to noise ratio of 1 for a wavelength of 780 nm. 149

List of Abbreviations

WHO	World Health Organisation
FGS	Fluorescence Guided Surgery
NIR	Near infrared
EM	Electromagnetic
CT	Computerised tomography
MRI	Magnetic Resonance Imaging
US	Ultrasound
PET	Positron Emission Tomography
RF	Radio Frequency
SR	Super Resolution
SPION	Superparamagnetic Iron Oxide Nanoparticles
MPIO	Microparticles of Iron Oxide
VCAM-1	Vascular Cell Adhesion Molecule 1
SPECT	Single Photon Emission Computerised Tomography
OCT	Optical Coherence Tomography
DOT	Diffuse Optical Tomography
FDOT	Fluorescence Diffuse Optical Tomography
ICG	Indocyanine Green
EPR	Enhanced Permeability and Retention Effect
MB	Methylene Blue
FDA	Food and Drug Administration
5-ALA	5-aminolevulinic acid
Pp-IX	Protoporphyrin IX
Folate-FITC	Folate Fluorescein Isothiocyanate
PSMA	Prostate Specific Membrane Antigen

EGFR	Epidermal Growth Factor Receptor
HER2	Human epidermal growth factor receptor 2
gGlu-HMRG	γ-glutamyl hydroxymethyl rhodamine green
LED	Light Emitting Diode
FOV	Field of View
FWHM	Full Width at Half Maximum
DU	Digital Unit
CCD	Charge Coupled Device
emCCD	Electron Multiplied CCD
CMOS	Complementary Metal Oxide Semiconductor
PIC	Programmable Intelligent Controller
ADC	Analogue-to-Digital Convertor
EEPROM	Electrically Erasable Programmable Read-Only Memory
GUI	Graphical User Interface
SNR	Signal-to-Noise Ratio
NA	Numerical Aperture
ILT CCD	Interline Transfer CCD
FT CCD	Frame Transfer CCD

List of Symbols

Q_Y	Quantum Yield
$f/\#$	f-number
I	Intensity
$\Re$	Responsivity
A	Area
i_{PD}	Photodiode Current
φ	Photon Flux
a	Calibration Coefficient
$V_{setpoint}$	LED Setpoint Voltage
$\varphi_{Emitter}$	LED Emitter Photon Flux
$I_{Emitter}$	LED Emitter Intensity
λ	Wavelength
h	Planck's Constant
c	Speed of Light in Vacuum
I_{in}	Intensity incident on CCD chip
V	Voltage/grey level after gamma correction
γ	Gamma Factor
f	Focal Length
u	Object Distance
v	Image Distance
M	Magnification
i	Image Height
o	Object Height
u_c	Combined Lens Object Distance
v_c	Combined Lens Image Distance
f_c	Combined Lens Focal Length
d	Distance

$\varphi_{spectrum}$	Spectrum Detected by the Imager
c_N	Constant
σ_{total}	Total (*r.m.s.*) Noise
σ_{read}	Total (*r.m.s.*) Read Noise of the Camera,
σ_{shot}	is the photon shot noise
σ_{FPN}	fixed pattern noise.
S	Camera Signal
K_{ADC}	Conversion Gain of the Camera
P_N	Fixed Pattern Noise Quality Factor
$\sigma_{read+shot}$	Total *r.m.s.* noise present in the signal
n	Refractive index of the medium in which light is traversing
θ	Acceptance angle of an optical component
r	Rayleigh criterion of resolution
$\delta\varepsilon$	Infinitesimal element of étendue
δA	Infinitesimal element area
$\delta\omega$	Infinitesimal element of solid angle

Introduction

Cancer is a major health concern worldwide with an estimated 9.6 million deaths in 2018 attributed to the disease (equating to 1 death in every 6). This makes cancer one of the leading causes of death worldwide, as reported by the World Health Organisation (WHO)[1, 2].

As the world population grows in size and the proportion of elderly people rises with time as a result of increased life expectancy, it is predicted that the number of new cancer diagnoses will rise. Specifically, it is expected that, by the year 2040, the incidence of cancer will have risen by 62% from that reported in 2018, with the number of new cases increasing to 27.5 million per year[3]. However, despite this predicted rise in the number of new cases of cancer being diagnosed, survival has been improving with survival rates doubling over the last 40 years[4]. This can be expected to increase if the diagnosis time becomes shorter and treatment becomes more sophisticated.

Following diagnosis, three main treatments are used to treat the cancer: chemotherapy, radiotherapy and surgery. A patient may receive one type of treatment or a combination of multiple treatments depending on the location of the cancer and its stage of advancement[5]. Of these three treatment options, surgery is perhaps the most popular method of treatment, since a large tumour can be quickly debulked or even removed entirely in a single procedure. Chemotherapy and radiotherapy, on the other hand, usually require repeat procedures to shrink the tumour over time. Furthermore, in the case of radiotherapy the patient is exposed to ionising radiation,

which can induce damage in other tissues in proximity to those targeted during treatment[6].

Surgery aims to achieve complete resection of a tumour with a margin of healthy tissue (resection with negative margins). The margin of healthy tissue is crucial if the patient is to achieve good prognosis[7, 8]. During a procedure, the surgeon typically relies on visual inspection and palpation (feel) to delineate tumours from healthy tissue[†]. In most surgical procedures, the only visual cues that alert the surgeon to the presence of cancerous tissues are differences in colour and shape compared to surrounding healthy tissues[9, 10]. Since these identifiers are arbitrary and represent macroscopic features of tissue, tumours may go undetected, resulting in residual cancer in the patient, which ultimately leads to the need for repeat surgeries (or other treatments) and poorer prognosis for the patient.

Fluorescence Guided Surgery (FGS) is an emerging intraoperative imaging modality which aims to improve surgical outcomes by acting as a real time visual guide for the surgeon. Specifically, visual cues from FGS imaging allows the surgeon to more easily identify tissues of interest which require resection or sparing during the resection of malignant tumours. FGS acts as a visual guide by providing greater contrast than that achievable with white light reflectance imaging, using near infrared (NIR) electromagnetic (EM) radiation.

The first documented used of fluorescence in surgery was in 1948, where the clinical use of fluorescein aided in the detection of intracranial neoplasms[11]. After this initial

[†] The surgeon is entirely restricted to visual inspection in the case of robot-assisted surgery.

interest in FGS, further uses of the technique were not reported and the number of new publications fell to zero. However, over the course of the last 30 years, interest in the technique has increased dramatically with the number of publications/year increasing from near zero in 1990 to 853 in 2018[Ref. 12]. This increased interest can be attributed to the increase in the number of available markers and commercially developed FGS imagers, such as the Flare™, Fluobeam® and NOVADAQ Spy-Elite™ imaging devices (many of which have been used in the operating room in various clinical trials).

Project Aims

The aim of this dissertation is to describe new technology that aims to improve on some of the limitations of FGS. Specifically, this work is focussed primarily on the technical aspects of developing new devices for imaging and quantification of FGS imager performance. In summary, the aims of this project are:

- To develop a novel opto-electrical calibration standard against which commercial FGS imagers can be characterised in terms of their sensitivity to fluorescence photons (in units of photons/second/cm^2) and in terms of the delivered excitation power to the sample (in units of mW/cm^2) as a function of working distance. Little information is available regarding FGS imager performance characteristics, for this reason this FGS calibrator will be used to determine the performance characteristics of FGS imagers. The results from imager calibration can be used to enable surgeons to compare the performance of different imagers and make informed decisions regarding the best imager to use in their FGS procedures. Furthermore, data from

calibration of FGS imager performance could potentially be used to inform a model of imager performance after different environmental conditions (such as pH, temperature and solvent) have affected the emission of the target fluorophore.

- To develop a novel *ex-vivo* imager for analysing resected tissue samples in the operating room. This imager aims to provide quick feedback to the surgeon allowing the surgeon to decide whether or not further surgery is needed (i.e. whether or not negative margins have been achieved). The imager aims to be more sensitive than currently available commercially available FGS imagers, particularly laparoscopic/robotic systems.
- This study ultimately seeks to continue the work done to test new FGS imaging technology in clinical and pre-clinical environments to ascertain how useful it is to clinicians and surgeons and to demonstrate that it fits seamlessly into the workflow of surgery.

1. Background

1.1 An Overview of Imaging Techniques in Surgery and Oncology

Fluorescence guided surgery is a relatively new technique available to surgeons, which is utilised during surgery to improve patient outcomes. However, FGS is not the only imaging technique that is available to surgeons, there are a variety of techniques that are used in the diagnosis and treatment of cancer which will be briefly discussed before moving on to the principles of FGS that make it such a potentially useful tool for surgeons.

1.1.1 Conventional Imaging Techniques

Conventional imaging techniques include the standard X-ray, computed tomography (CT), magnetic resonance imaging (MRI), ultrasound (US) and positron emission tomography (PET). These imaging techniques can be described as conventional (at least in the first world) since they are well established techniques used in a variety of medical applications in mainstream patient treatment. All of these techniques can be described as either absorptive or emissive imaging techniques since the method of achieving contrast is the detection of absorbed and/or transmitted waves/energy (although in the case of US, reflection is utilised to achieve contrast).

We begin with the standard X-ray or radiograph, which is commonly used for anatomical imaging, specifically in the diagnosis of broken bones and dentistry to image the jaw. However, the X-ray is also utilised in oncology to diagnose bone lesions and lung cancer[13, 14].

The technique is an absorptive imaging technique which involves exposing the target tissue(s) with a high energy X-ray beam produced by an X-ray source[(ref. 15), ‡]. The X-rays are absorbed by dense tissues (such as bone or dense lesions) and pass almost uninterrupted through less dense tissues (such as skin and muscle). The X-rays that have not been absorbed in the tissue of the patient are absorbed in a detector which is either a photographic plate or a digital X-ray detector/recorder. The difference in the absorptive properties between different tissues is the contrast mechanism that generates the image. The difference in tissue density is largely what causes the difference in absorption. Typically, the resolution achievable with the conventional X-ray can be of the order of ∼100 μm – 1 mm in the pre-clinical environment and ∼500 μm – 1 mm in the clinical environment[(ref. 16)]. This is a higher resolution than that achievable with the other aforementioned imaging techniques, which is impressive considering the fact that the X-ray was discovered much earlier.

A conventional X-ray scan is used to generate a high contrast 2-D image. When 3-D information is required, computerised tomography (CT) is used. Initially, a CT scan involved rotating a fan shaped X-ray beam and a detector around the patient to generate a series of 2-D ‘slices’ that are pieced together to produce a complete 3-D image of the patient[17, 18]. In more modern CT imaging, helical X-ray scans are used to generate the image[19].

‡ An X-ray generator consists of a cathode (electron source); an anode target, which is typically made of tungsten (X-ray source) and a vacuum tube. Electrons boiled off from the cathode are accelerated towards the anode. Upon collision with the anode these high energy electrons produce X-rays.

The main drawback of the X-ray is the ionisation of tissues induced during exposure. A CT scan can lead to higher exposure due to the size of the volume scanned and the quality of the X-ray beam[20]. Furthermore, since X-rays penetrate easily through soft tissue there is little soft tissue contrast, limiting the usefulness of CT in soft tissue imaging applications. Despite these drawbacks, CT imaging has numerous advantages such as fast acquisition time, high spatial resolution and cost effectiveness amongst others[21].

MRI does not involve exposing the patient to ionising radiation and so does not represent a harm to the patient. MRI instead utilises magnetic resonance to achieve contrast. Specifically, MRI manipulates protons using magnetic fields (typically of the order of 1.5 – 3T or higher). The magnetic fields cause the protons, present in the patients' tissues, to align along the magnetic field lines. Radiofrequency (RF) radiation is then used to excite the protons, which reemit the absorbed radiation as they relax back to their original orientations[22]. The emitted radiation caused by relaxation provides the data for generating the image of the patient. Computer software interprets the data to generate a detailed 3-D image.

Protons are abundant in water, which is present in every soft tissue of the human body and as such, huge amounts of detail can be generated from MRI scans. However, MRI is generally limited to using hydrogen ions since other elements such as carbon are much less detectable[21]. The highest resolution achievable in the preclinical environment with MRI is on the order of 100 μm. In the clinical environment, the highest resolution achievable with MRI is of the order of 1 mm However, super resolution (SR) algorithms[23] can be used to increase the resolution

beyond these limits[§]. MRI is used to image a variety of different cancer types, such as prostate cancer and breast cancer amongst others[24, 25].

Ultrasound (US) is another example of a widely used conventional imaging modality that does not rely on the use of ionising radiation. US imaging instead uses a transducer to emit ultrasound frequencies (1 – 20 MHz) into the human body, which are reflected at the interface between tissues of different density. An image is formed from determining the arrival times and intensities of the reflected ultrasound waves[21, 26]. US is typically used in prenatal imaging of the developing foetus but can be used in other applications such as monitoring blood flow and gathering diagnostic information on organs such as the liver, gallbladder, kidneys, spleen and bladder (amongst others). The limitation of ultrasound imaging is that it cannot be used to image within or beyond anatomical features that are of high density such as bone. Although ultrasound waves are reflected at the interface between soft tissue and bone, the transmitted ultrasound waves are attenuated (so imaging beyond this interface cannot be performed). Furthermore, US cannot be used to image organs that may contain large volumes of gas such as the lungs or bowel[27] for the same reason as described for bone.

The techniques described above all provide a wealth of anatomical information which can serve as a guide with which surgeons and physicians can use to plan treatment. These imaging techniques can be used to diagnose cancer if suspected and

[§] Introduced in the 1980s, super resolution algorithms combine a set of low-resolution samples to generate a much denser sampling grid, forming a much more detailed image than achievable with a single sample obtained in a conventional MRI scan.

are used in the management of the disease as it progresses. However, one issue that connects all these techniques is lack of specificity which prevents probing into the biomechanical processes that govern carcinogenesis[28].

1.1.2 Molecular and Functional Imaging

To increase specificity, attempts have been made to adapt the techniques for molecular targeted imaging thereby improving the contrast in the target tissues of interest. As well as adapting conventional techniques for molecular targeted imaging, functional imaging (which includes positron emission tomography or PET[29]) also provides greater specificity by probing specific processes occurring in the target tissue such as changes in blood flow or metabolism, for example.

In the case of MRI, increased specificity and therefore contrast has been provided by using iron oxide nanoparticles, in particular superparamagnetic iron oxide nanoparticles (SPIONs). Although the presence of SPIONs in tissue leads to some loss of signal, their unique magnetic properties cause an improvement in contrast when they are present in the strong magnetic field applied by an MR machine[30].

One specific example of contrast enhanced imaging using iron oxide particles includes the use of microparticles of iron oxide (MPIOs) in the brain. Specifically, MPIOs used to target VCAM-1[(ref. 31), **] expression in pre-clinical brain metastasis[32].

** VCAM-1 (vascular cell adhesion molecule 1) is a glycoprotein that is expressed on the cell surface membranes that has the function of mediating the adhesion of lymphocytes (amongst others) to the vascular endothelium.

Targeted nanoparticles have also been utilised in preclinical CT imaging, with gold nanoparticles being utilised to increase contrast and allow the detection of cancerous lesions not visible with anatomical CT[33].

Increased contrast in ultrasound imaging is provided using targeted microbubbles which are injected intravenously and burst in the target tissue increasing the signal to noise ratio above that possible with conventional ultrasound (US)[34]. However, due to the size of the microbubbles its use becomes limited to preclinical research[35].

PET is a functional imaging technique which provides increased specificity by injecting a radioactive tracer (such as ^{15}O, ^{13}N, ^{11}C and ^{18}F) into the patients' blood stream, which is allowed to circulate and accumulate in the target tissue. Typically, PET tracers are conjugated to analogues of glucose molecules (the most common being fluorodeoxyglucose[36]), which are taken up by cells undergoing metabolism. Positrons emitted from the tracer annihilate with electrons, with each annihilation event resulting in the emission of two γ-rays that travel in approximately opposite directions to each other. PET imaging can be paired with CT to provide additional anatomical information that PET cannot provide on its own. However, the use of CT is a drawback of the technique, since the patient receives a dose of ionising radiation[21]. For improved image quality and reduced image acquisition time, a technique known as time-of-flight PET is utilised. Time-of-flight PET involves determining the arrival times of emitted γ photons to determine the most likely origin of the annihilation event[37].

Alongside PET, single photon emission computerised tomography (SPECT) is another functional imaging technique used clinically[38]. SPECT is essentially the same as PET, except that it involves the use of a single detector that detects single γ-ray emission from the radionuclide. Like PET, the involvement of ionising radiation in SPECT is a drawback of the technique. Another drawback is the high cost and relatively poor clinical spatial resolution of SPECT, of the order of 8-12 mm, compared to 4-6 mm for clinical PET[39, 40].

The relatively poor spatial resolution afforded by PET and SPECT is undesirable as small tumours (<1 mm) go undetected. Early detection of tumours is desirable as they can be treated much earlier. This is in part due to the fact that small tumours have not undergone the angiogenic switch, when the tumour has begun to develop its own vasculature to facilitate further growth[41, 42].

Molecular and functional imaging affords greater specificity over conventional imaging techniques. However, it is desirable to observe multiple biological processes simultaneously, to gain more information regarding the underlying mechanisms and interactions tacking place in cancer and other diseases[21].

The advantages and disadvantages of the imaging techniques discussed above are summarised in Table 1[(Ref. 21)].

Imaging Technique	Pre-clinical Resolution	Clinical Resolution	Advantages	Disadvantages	Molecular Imaging Possible?
X-ray/Computerised tomography (CT)	~100 μm – 1 mm	~500 μm – 1 mm	Low cost; high contrast; short image acquisition time (CT)	Involves ionising radiation	No
Magnetic resonance imaging (MRI)	~100 μm	~1 mm	Non-ionising; produces highly detailed images	Expensive; long image acquisition time	Yes
Ultrasound (US)	0.01 – 0.1 mm (<1 mm depth) 1-2 mm (>1 mm depth)	0.01 – 0.1 mm (<1 mm depth) 1-2 mm (>1 mm depth)	Low cost; non-ionising	Handheld probes are unsuitable for use during surgery	Yes
Positron emission tomography (PET)	~1-2 mm	~4-6 mm	Specificity; technique can be applied at any depth in any location in the body	Expensive; involves ionising radiation; requires CT to provide anatomical reference data	Yes
SPECT	~1-2 mm	~8-12 mm	Specificity; cheaper than PET	Involves ionising radiation	Yes

Table 1: Summary of key clinical imaging techniques employed in medical imaging and cancer diagnosis and treatment. Data included in this table is collated from James and Gambhir (2012) and Vandenberghe, S, *et al.* (2016). The resolutions for clinical imaging and pre-clinical imaging are quoted separately as in many cases the achievable resolution is higher in pre-clinical imaging.

In summary, each of the conventional imaging modalities listed in Table 1 can be used to provide important diagnostic data which can serve as an anatomical reference to be used to plan treatment and manage disease progression. Traditionally, these imaging modalities are limited in their specificity but as discussed in this section a variety of options exist to improve on this lack of specificity. Specifically, by targeting biomarkers with contrast agents, structures that would otherwise be undetectable can be identified. Examples include the use of radioactive tracers in PET; the use of iron oxide nanoparticles in MRI; the use of gold nanoparticles in

preclinical CT imaging and the use of microbubbles in ultrasound imaging. However, despite the possibility for improved specificity, none of these imaging modalities are convenient for use in surgery as a real time intraoperative imaging tool due to such reasons as relatively long image acquisition times (longer than that needed for real time imaging), use of ionising radiation and large imaging devices (such as an MRI machine).

1.1.3 Optical Imaging

Beyond the conventional, established medical imaging techniques discussed above, optical imaging is a field of imaging that is receiving more attention due to the increased specificity it can provide. Optical imaging involves using ultraviolet/UV (100-400 nm), visible/VIS (380-740 nm), near infrared/NIR (800-2500 nm) and infrared/IR (2500 nm-1 mm) light to probe tissues. High contrast can be achieved in optical imaging by exploiting the intrinsic properties of the tissues being imaged, specifically scattering and absorption. Contrast can also be achieved using a dye or fluorescent marker. Specific biomarkers are employed to achieve high specificity and molecular sensitivity[43].

There are several notable advantages of optical imaging[44], specifically:

- optical imaging does not involve exposing the patient to ionising radiation, which is beneficial to patient care
- optical imaging is particularly useful for the imaging of many soft biological tissues as many different tissues can easily be distinguished from one another as a result of the great variability in the optical properties of different tissues (i.e. refractive index, scattering and absorption)
- optical imaging can utilise a broad range of different wavelengths within the electromagnetic spectrum to probe different anatomical features and molecular processes
- many optical imaging techniques can be performed at low cost

Furthermore, high resolution can be obtained, although imaging depth is sacrificed as scattering becomes reduced at lower imaging depths.

Despite the notable advantages, optical imaging suffers from limited depth penetration due to increasing optical absorption and scattering at depth. Since many structures of clinical interest lie several millimetres beneath the surface of human tissues, limited depth penetration is undesirable. As a result, near-infrared wavelengths are the most useful area of the electromagnetic spectrum for clinical optical imaging applications due to the biological window of reduced absorption and scattering. This biological window is exploited to enable imaging at increased depth without sacrificing resolution[45]. The NIR biological window is highlighted in Figure 1.

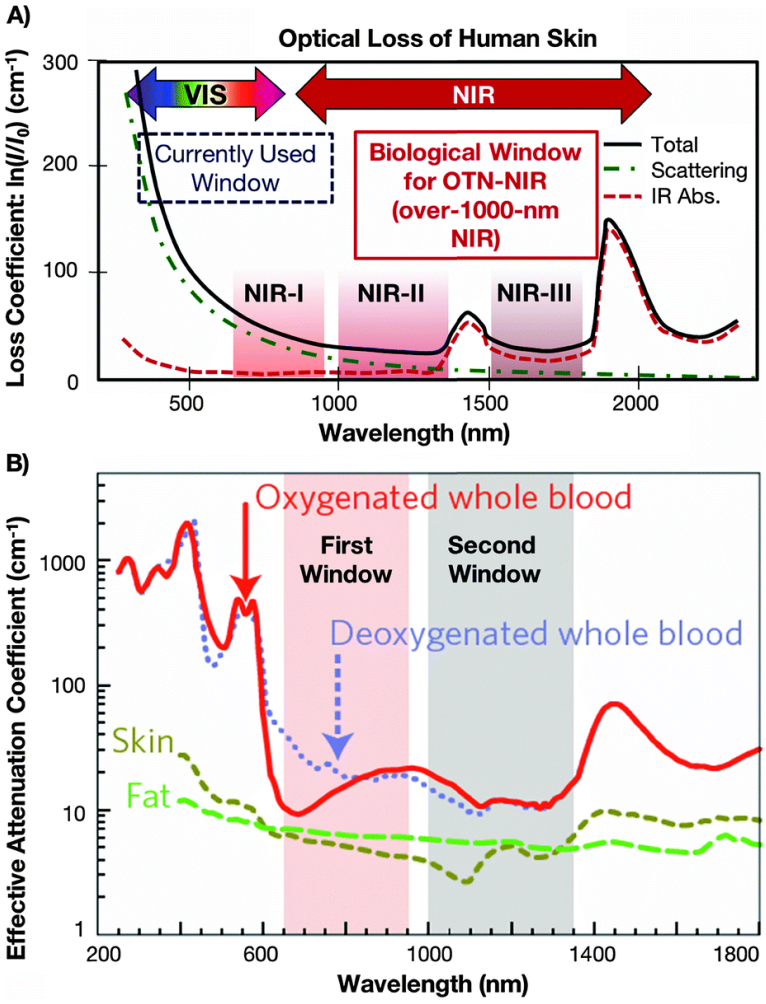


Figure 1: Image from (Hemmer, E. *et al*. 2016). *Top*: Optical loss coefficient for human skin including both scattering and absorption for all three near infrared windows. *Bottom*: Effective attenuation coefficient for whole blood, skin and fat as a function of wavelength, note the minima at near infrared wavelengths.

A number of techniques have been developed for optical imaging[44]. The first to be discussed here is endoscopy, which is the oldest and perhaps the simplest optical imaging technique included. Endoscopy relies on the use of an endoscope, which is a flexible tube that houses imaging optics as well as a light delivery system to illuminate the field of view of the endoscope. The technique is used in a variety of clinical applications in both disease diagnosis and minimally invasive surgery. Endoscopy is useful as it can be used to image tissues that would otherwise be accessible only by surgery. The technique is primarily limited to tissue surface reflectance imaging which makes it difficult to image structures that may be hidden beneath the surface. Techniques such as optical coherence tomography and NIR fluorescence have been used in conjunction with endoscopy to improve the imaging depth penetration[46].

The next optical imaging technique to be described is optical coherence tomography (OCT). OCT is a technique that uses low coherence interferometry, with a typical setup consisting of a low coherence broadband light source coupled into a (Michelson) interferometer. Using a beam splitter, the emission from the low coherence light source is scanned across both a moving reference mirror and the tissue sample to be investigated. Light scattered from the mirror and the tissue sample is recombined and detected by a camera. Interference induced in the detected light by differences in the scattering properties of the sample and reference media infers the structural details of the tissue sample. The acquired data is interpreted by computer software, which forms a 2-D or 3-D image. Images generated by OCT can have micrometre resolution[47, 48]. OCT is most widely used to generate detailed

images of the retina in ophthalmology due to the inherent transparency of tissues in the eye[49]. The technique is also used in a variety of other clinical applications such as cardiology, to image the microstructure and morphology of the vessel wall lumen of coronary arteries, in the context of treating heart disease[50].

Photoacoustic imaging is another optical imaging technique that is becoming more prominent in the clinical environment. The technique involves using a laser to induce localised heating of tissues of interest. The thermal radiation perturbs the tissues, which subsequently emit ultrasound waves, which are detected by ultrasound transducers. The resolution and imaging depth are proportional to the ultrasonic bandwidth[51]. It is reported that sub-millimetre resolution is achievable at a depth of 1 cm; sub-100 μm resolution is achievable at a depth of millimetres and sub-10 μm resolution is achievable at depths of a few hundred microns for a fixed bandwidth of 10 MHz[52]. Photoacoustic imaging is used for a number of different clinical applications such as tumour angiography, imaging skin melanomas and blood oxygenation monitoring in tissues[44].

Diffuse optical tomography (DOT), is an imaging technique which has been applied to clinical applications such as brain imaging, breast cancer imaging as well as muscle, peripheral circulation and joint imaging (amongst others). The technique involves illuminating the target area with pulsed, near infrared light (typically from a laser) that traverses the skin and other layers of tissue below (in the case of brain imaging, the laser illumination traverses the scalp to reach the brain). The contrast mechanism is the scattering and absorption properties of the target tissue, which is used to piece the details of the image together[53]. FDOT (fluorescence diffuse

emission tomography), utilises emission from fluorescent contrast agents to improve tumour detection and characterisation. With fluorescent contrast agents, FDOT also improves the molecular specificity of diffuse optical tomography to probe information otherwise inaccessible through conventional DOT such as tissue pH (for example)[54]. However, DOT can suffer from slow image acquisition time, particularly in the case of time domain DOT[55, 56].

Another technique which exploits the scattering properties of biological tissue is Raman spectroscopy which utilises the scattering of (near) UV, visible and near infrared light. Each scattering event causes the wavelength of the incident photon to either increase (Stokes shift) or decrease (anti-Stokes shift), with the spectrum providing a fingerprint of the biomolecules present in the tissue being analysed[57].

Many of the aforementioned imaging techniques offer advantages over traditional imaging techniques such as higher resolution, lower cost and no ionising radiation. However, one major disadvantage of all of the techniques described thus far is the difficulty in transferring the technology to surgical theatre where they may be utilised to guide surgical decision making in real time. In the case of techniques that rely on the use of ionising radiation, the reason is obvious, in the case of other techniques unwieldy instrumentation and long image acquisition time are required to generate the images. The aim of fluorescence guided surgery (FGS), is to overcome this obstacle and offer surgeons the advantages of other imaging modalities in theatre to potentially improve surgical outcomes.

1.2 Fluorescence Guided Surgery

Fluorescence guided surgery (FGS) serves as a real time intraoperative aid for the surgeon. Fluorescence emission in the NIR, either from fluorophores by themselves (non-specific FGS) or from fluorophores conjugated to a particular targeting agent (specific FGS) [58, 59] is utilised to increase contrast. In non-specific FGS, emission from non-specific fluorophores provides useful anatomical guidance for the surgeon. In the case of specific FGS, the specific (molecularly targeted) fluorescence emission provides the necessary contrast required for the surgeon to delineate healthy and diseased tissues. By exciting and imaging fluorophores using NIR wavelengths allows for greater imaging depth, due to reduced absorption and scattering. Furthermore, exciting fluorophores in the NIR also reduces confounding signals from autofluorescence[††], thus improving the signal to noise ratio compared to fluorescence excitation with shorter wavelengths. FGS is utilised in a variety of different cancer surgeries such as prostate cancer, breast cancer and head and neck cancer amongst others[60]. In the case of these particular cancers, FGS is extensively used for sentinel lymph node mapping. Sentinel lymph node mapping traces the drainage of lymphatic fluid containing fluorescence from diseased tissue into the lymphatic system. Sentinel lymph nodes that are fluorescing are resected as part of the surgical treatment provided to the patient[61, 62].

FGS is primarily used to identify diseased tissues but is particularly useful when the surgeon is required to preserve key anatomical structures, such as the ureters (for

[††] Autofluorescence is natural fluorescence emission from biological tissues, most commonly caused by NADPH and flavins.

example), which are at risk of injury during colorectal surgery[63, 64] or the neurovascular bundles during radical prostatectomy[65].

FGS is unique in that it can be applied to both open surgery and laparoscopic procedures[66] as shown in Figure 2.

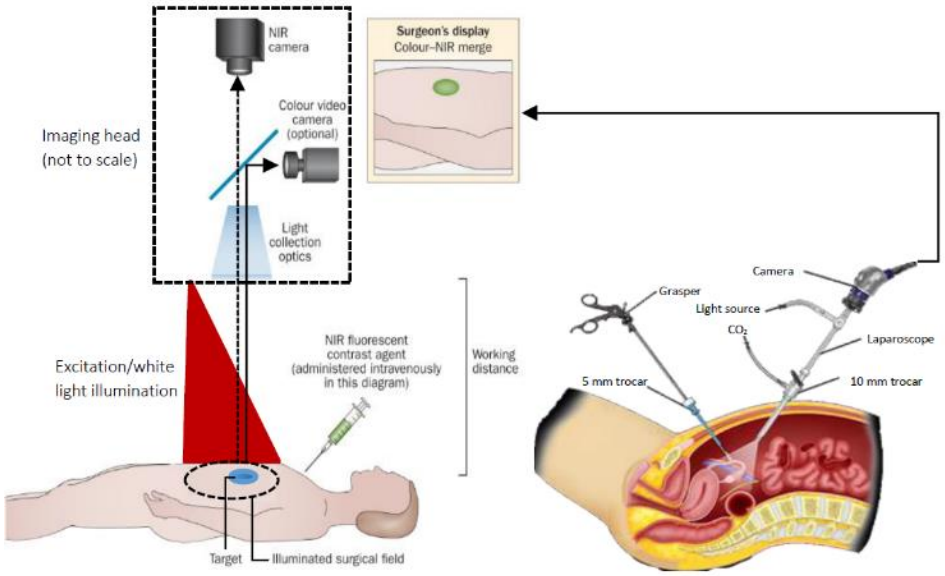


Figure 2: *Left*: Fluorescence Guided Surgery (FGS) for open surgery (image adapted from Vahrmeijer, A. L., et al., 2013). *Right*: FGS for laparoscopic (keyhole) surgery reproduced from Long Island Surgery, P. C., 2015 (from http://www.longislandsurgery.org/laparoscopic.html).

The physical process of fluorescence that provides the necessary contrast in FGS imaging has been well studied. The phenomena can, at its most basic level, be split into three distinct phases: excitation, excited state and emission. The excitation phase involves the absorption of photons by electrons in the ground state of fluorophores present in the tissue of the patient. These photons are provided by the excitation light source of the particular FGS imager. These photons excite the electrons into excited states of higher energy, the so-called singlet states. After spending a short amount of time in the excited state (typically ranging between picoseconds and nanoseconds),

an electron will transition back to the ground state, emitting a photon of reduced energy and longer wavelength (compared to the original excitation photon)[67]. The cause for this loss in energy is non-radiative processes that occur, either when the electron is occupying the excited state or during the transition back to the ground state. Fluorescence excitation and emission is commonly described using Jablonski diagrams such as the one shown in Figure 3(ref. 68).

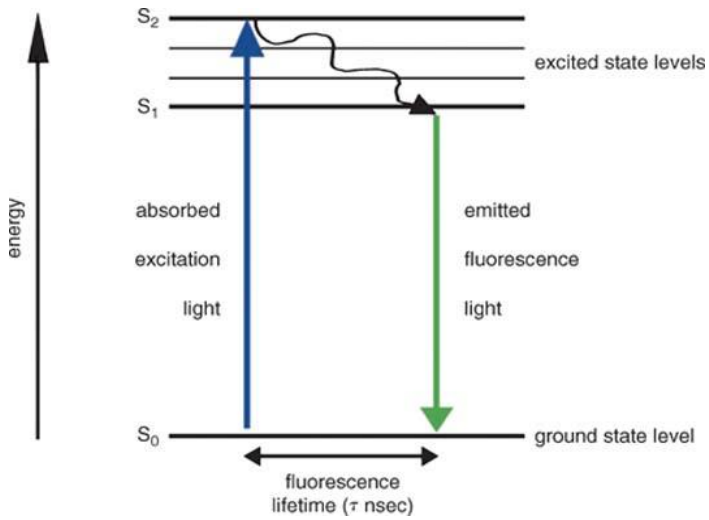


Figure 3: Jablonski diagram for a single fluorescence cycle reproduced from Llères, D., Swift, S., and Lamond, A. I. (2007). Upon absorption of a photon the ground state electron transitions to the excited state, this process takes femtoseconds. Following excitation, the electron loses energy over time as a result of non-radiative transitions in the excited state. The mean time spent in the excited state is the fluorescence lifetime, this timescale can vary between fluorophores from picoseconds to nanoseconds (the environment may also affect the fluorescence lifetime).

The wavelength shift between the excitation and emission photon is called the Stokes shift and is a result of the energy lost in the excited state phase, which cannot be avoided since the fluorophore must vibrate as a result of thermal energy[67]. An exemplar fluorescence spectrum of the fluorophore indocyanine green (ICG) is included in Figure 4, showing the Stokes shift[69].

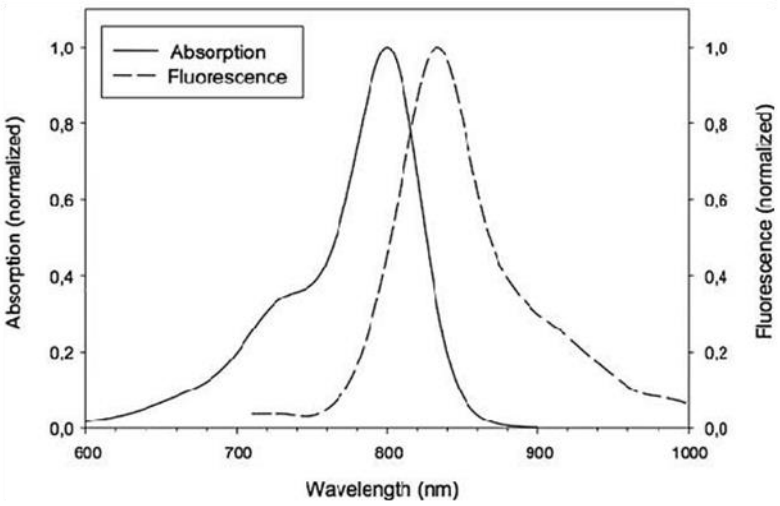


Figure 4: ICG spectra for absorption and fluorescence emission reproduced from Topaloglu, N., Gulsoy, M., and Yuksel, S. (2013). The shift between the two spectra is the Stokes shift for ICG.

The Stokes shift is a useful aspect of fluorescence as this separation of excitation and emission spectra allows for (usually) straightforward filtering out of unwanted excitation light in the emission detection channel of an imager.

The amount of light a fluorophore produces following excitation is related to a physical characteristic of the fluorophore, known as the quantum yield (Q_Y). The quantum yield is simply defined as the ratio of the number of photons emitted to number photons absorbed[67]. The quantum yield can never be unity (100 %) due to the non-radiative processes involved in the process. In the case of many NIR fluorophores used in FGS, this ratio is quite low with some quantum yields being of the order of a few percent[70]. The quantum yield is an important consideration when developing imaging technology as it determines how much light a fluorophore will produce for a given excitation power. If the fluorophore has a low quantum yield then larger concentrations of the fluorophore or more excitation light may be required to generate sufficient emission to be detected by an FGS imager.

1.2.1 Markers Used for FGS Imaging

Non-specific Markers

The two most widely used non-specific markers are indocyanine green (ICG) and methylene blue (MB) (which are widely available at relatively low cost compared to specific markers)[‡‡].

In the case of ICG, its rapid acceptance as a useful marker for clinical imaging is due to several factors. The most notable being its absorption (excitation) peak, which lies in the NIR region of the spectrum at 800 nm; its confinement in the vasculature surrounding cells (through binding of ICG to plasma proteins present in the blood), its low toxicity[71, 72] (which makes the risk to patients minimal) and its rapid excretion into the bile[73, 74]. ICG has been used extensively in the mapping of sentinel lymph nodes in many different cancers including breast cancer, gastric cancer, vulvar cancer, lung cancer, head and neck cancer and colorectal cancer, amongst others[60]. Interestingly, despite its lack of specificity, it is reported that ICG can accumulate in lesions that have received a direct injection of the marker into the tumour. This is due to the enhanced permeability and retention effect (EPR)[§§] and the size of the molecule[75, 76].

The use of ICG has been widely reported in many applications other than FGS but ultimately, as a non-specific marker, its lack of specificity is a major drawback. This

[‡‡] Developed in 1955 by Kodak Research Laboratories for NIR photography, ICG is notable as being the first NIR fluorophore to be approved by the FDA for use in the clinic.
[§§] The EPR effect is the uptake and retention of small molecules by a tumour that is caused by leaking vasculature due to damaged endothelial cells and pores in the walls of the blood vessels.

ultimately limits the clinical usefulness of the marker in FGS[77], particularly as specific markers are becoming more widely available.

Although not as widely used as ICG, MB is another non-specific dye that has been adopted as a fluorophore in a variety of FGS applications, these include breast cancer imaging[78] and sentinel lymph node mapping[79] amongst others. As an aside, MB has also been used as a medication to treat malaria and methemoglobinemia[***].

MB has an absorption (excitation) peak at a wavelength of 670 nm and an emission peak at 690 nm and is primarily excreted in the urine[60]. Due to its shorter peak excitation wavelength, compared to 800 nm for ICG, the marker has reduced penetration in tissues and greater autofluorescence is present meaning reduced signal to noise ratio when using methylene blue. Since MB is primarily cleared in the urine, it is ideal for imaging the ureters, as reported in the literature[63, 80]. Generally speaking, MB does not induce adverse reactions in patients but it has been reported that it can cause cardiac arrhythmias, decrease cardiac output and reduce renal blood flow amongst other harmful side effects when present in high concentrations[81].

Besides ICG and MB there are other non-specific probes that are employed in FGS applications. Such probes include 5-aminolevulinic acid (5-ALA) and fluorescein sodium. 5-ALA is a molecule that is administered to the patient either orally or topically. 5-ALA is interesting in that it induces the accumulation of protoporphyrin IX (Pp-IX) in epithelia or neoplastic tissues[82, 83]. Pp-IX is a fluorophore which is reported to have a variable absorption peak primarily depending on the pH of its

[***] Methemoglobinemia is a blood disorder characterised by the increased methemoglobin production.

microenvironment, its emission peaks being 634 nm and 620 nm for acidic and alkaline microenvironments respectively (the absorption peak lies in the visible light spectral region of 380-440 nm). 5-ALA has been implemented in bladder and prostate cancer FGS imaging[84, 85, 86] although use is limited overall due to its method of administration and high cost of production[82]. Furthermore, since the marker requires excitation at shorter wavelengths, it is difficult to image at depth (depending on the manner of excitation light delivery). Also, the patient is sensitive to light for hours afterwards and must be kept in the dark until the symptoms lessen.

Fluorescein sodium is another available non-specific probe, although the only recorded use of the fluorophore in a surgical context being the imaging of intracranial neoplasms[87]. The probe absorbs at a peak wavelength of 494 nm emitting at 512 nm and can even be observed with the naked eye with high enough doses (20 mg/kg)[88, 89].

Specific Markers

Whilst non-specific fluorescent markers have achieved success in the clinic, FGS requires the need for greater specificity afforded by specific markers if it is to reach its full potential as a useful intraoperative guide to surgeons. Several probes are currently in development to exploit overexpressed biomarkers that are linked to particular cancers. A typical specific probe consists of a fluorophore conjugated to an antibody, minibody, nanobody or antibody fragment, peptide or some other molecule. Current developments include folate targeted markers, monoclonal antibody-based probes and activatable probes[82].

The folate receptor is a cell surface antigen that is reported to be upregulated on the surface of tumour cells[90, 91]. By targeting this receptor with a probe that readily binds to it, fluorophores can readily accumulate increasing tumour to background ratio. One such probe is the folate fluorescein isothiocyanate (folate-FITC) probe which has been reported to have been utilised in the treatment of lung and ovarian cancer patients[92]. The probe works by circulating in the blood stream, attaching to tumour cells using the folate receptor and then becoming internalised inside the cell. Whilst inside the cell, the marker remains intact for some time allowing for continuous fluorescence throughout this process[93, 94]. One drawback of the probe, however, is its peak excitation and emission wavelengths, being 495 nm and 520 nm respectively[82]. This limits the depth at which imaging can be achieved using this probe.

Monoclonal antibody-based fluorophores are another type of targeted probe that are receiving attention. Like the folate receptor several over receptors have been identified for targeting. These include prostate specific membrane antigen in prostate cancer (PSMA, folate hydrolase) and the epidermal growth factors (EGFR) and EGFR type 2 (HER2) in breast cancer[95, 96]. In the case of PSMA, the cell surface antigen is not explicitly linked to prostate cancer but nonetheless is particularly useful as it is almost exclusively expressed in prostate tissues[97]. Probes used to target these cell surface antigens are administered systemically. To ensure that a sufficient signal to noise ratio can be achieved, a delay is introduced after administration. This ensures that probe that has not bound to the target tissue is excreted from the body leaving only the marker bound to the target, reducing the background significantly[98].

Activatable fluorescent probes are another method of achieving high specificity and tumour to background ratio. Activatable probes are so named for their ability to be non-fluorescent (switched off) when not bound to the target molecule and become fluorescent (switched on) when they become bound to the target molecule/cell[99]. One example of an activatable probe is γ-glutamyl hydroxymethyl rhodamine green (gGlu-HMRG)[100]. gGlu-HMRG is administered topically via a spray but other activatable probes can be administered intravenously.

Due to the fact that activatable probes only become fluorescent when they are attached to the target, they can offer higher tumour to background ratios. Despite this positive there are drawbacks. For example, activatable probes target enzymes which are not specific to any particular tissue type or cancer. Furthermore, the enzymes that activatable probes target are able to move freely in the extracellular space. This may lead to the marker diffusing away from the intended target site, reducing the signal in the specific area of interest. Perhaps the biggest drawback, however, is the question mark around patient safety which has not been fully determined in the case of activatable probes which limits their use in humans[76].

1.2.2 FGS Imaging Technology

Inevitably, as FGS has expanded and its clinical use demonstrated, industry has become interested in developing imagers specifically for FGS. A number of these imagers have become adopted for a variety of procedures for both open and keyhole surgery. Due to the availability of ICG for clinical imaging, many imagers have been developed for use with this marker. Notable examples include the Flare™, Fluobeam® and NOVADAQ Spy-Elite™.

The key features that constitute a clinical FGS imager are the excitation light delivery system, the camera and the instrument software, which handles the camera controls and excitation light delivery system, as well as image processing.

The excitation light delivery system typically (but not always) consists of a light source of wavelength that corresponds to the absorption spectrum of the marker the imager is designed for. Filters may be introduced to remove unwanted wavelengths from the emission spectrum of the excitation light source if needed. For systems that require illumination over a defined area, a series of optical components may be included in the system to manipulate the shape of the beam to one more appropriate to the application.

The most commonly used light sources for fluorescence imaging applications are filtered broadband lamps, laser diodes and light emitting diodes (LEDs). LEDs and laser diodes are most commonly used because they possess favourable optical characteristics. Filtered broadband lamps tend not to be utilised as much due to their low efficiency, large spectral bandwidth and large emission solid angle. Low efficiency results in the delivery of less than optimal power density to the tissue surface, resulting in reduced signal to background ratio. A large spectral bandwidth makes filtering non-trivial with excitation light leaking into the emission channel a likely outcome. Furthermore, filtering of these broadband lamps would likely result in the rejection of a large number of output photons. This would lead to the transfer of large amounts of the heat to the filters resulting in high device operating temperatures[101], which is undesirable for a clinical instrument.

LEDs and laser diodes offer much more optimal optical characteristics for the light source of an FGS imager. Specifically, both LEDs and laser diodes are much more efficient and, in the case of laser diodes, the spectral bandwidth is narrow which allows for easier filtering and higher selectivity of the peak excitation wavelength. However, LEDs are generally less expensive than laser diodes.

The detection system of an FGS imager typically consists of a light collection system (consisting of a series of lenses), filters and a camera. The specific lenses chosen in the light collection system are based on the field of view (FOV) of the camera, the working distance from the sample, the desired magnification and the depth of field required. A dichroic beam splitter can be inserted into the detection system optics when requiring separate visible and fluorescence channels which are each detected by a separate camera. Filters are an important part of the detection system as they ensure that excitation light being reflected from the surface of tissues is prevented from entering the camera (thereby preventing confounding signals from being presented in acquired images)[101].

A variety of options exist for camera selection in FGS. A widely used camera type is a charge coupled device (CCD) camera (see Appendix C). Even though CCDs are widely used in FGS imagers, their responsivity drops off as the wavelength shifts further into the infrared[102]. Furthermore, CCD readout noise is an issue as it can reduce the signal to noise ratio of the detected fluorescence, although cooled CCD cameras are available, which have reduced readout noise. A range of other CCD cameras are available for increased gain such as the emCCD (electron multiplied CCD) , for example, which offer gains much higher gain than that of standard CCDs,

albeit with increased noise[103]. CMOS (complementary metal oxide semiconductor) cameras have been used as well but CMOS sensors typically have higher noise than CCDs. However, advances in CMOS technology has yielded the scientific CMOS camera which has high read out rates (compared to slow readouts of CCD cameras) and notably higher resolution[104]. Currently CMOS cameras are the most widely used camera technology in medical imaging with CCDs being used primarily in astronomy applications.

In order for FGS imagers to reach their full potential as a useful intraoperative guidance tool, a number of features are desired, as reported in the literature. The first of these is the ability to overlay fluorescence imaging data on top of white light images of the surgical scene. The white light images provide spatial context for the fluorescence data as, on its own, fluorescence imaging data can potentially be difficult to process. A number of imagers provide this feature such as the Quest Spectrum imaging device, amongst others[105]. The second feature desired in FGS imagers is the ability for the imager to provide fluorescence mode during theatre room light operation. Theatre lights are an unwanted source of broadband background signal, which reduces the signal to noise ratio. To overcome background signal, when it is not possible to turn of the operating theatre lights, high sensitivity to the fluorescent emission is required. This is perhaps one of the most important aspects of the imager design as fluorophore concentrations are likely to be low. This is due to several factors such as the distribution of molecular targets for the marker, the availability of the marker (due to the cost of manufacture) and, in the case of non-specific markers, retention of the fluorophore in the target tissues.

Another desirable feature is the ability of the imager to image multiple different fluorophores at once thus probing into multiple molecular processes at the same time.

Finally, the device footprint and ergonomics is an important consideration for a device that is to go into surgical theatre. FGS imagers can be unwieldy to use in the operating theatre due to their relatively large footprint. Space in an operating theatre is at a premium and for this reason, it is crucial that devices are as small and ergonomic as possible so as not to disrupt surgical workflow[101].

One aspect of commercial fluorescence imagers and FGS that needs to be addressed is the lack of quantified performance data available. Comparative imaging is highly desirable for FGS as a particular marker may require a particularly sensitive imager and, if the performance of FGS imagers can be quantified and compared, then the surgeon has an easier task of choosing the imager they need for their application. An effective calibration standard is currently lacking, which can measure fluorescent imager performance. Attempts have been made to provide such a standard for calibration. These typically consist of fluorescent phantoms or quantum dot solutions, which require preparation and do not provide a measurement of the number of photons being detected. Instead they provide a measurement of arbitrary counts above some pre-decided threshold[106, 107, 108]. Furthermore, measurements of sensitivity are also given in terms of the concentration of a specific marker, which gives no indication of the performance of the imager with other markers (the absolute performance of the imager). The work described in this dissertation aims to address this issue with the development of a novel FGS calibration device (discussed in chapter 2).

Another aspect of FGS imaging that is desirable for FGS, is the ability to assess resected tissue samples *ex-vivo*. The potential to analyse surgical margins immediately following resection could improve the outcomes of the procedure. Wide field and laparoscopic FGS devices are designed for *in-vivo* imaging and as such are not suitable for *ex-vivo* imaging following resection of diseased tissue. Resected tissue samples are usually sent for histological analysis, which involves staining the tissues with a dye and is then followed by microscopic evaluation to ascertain the boundary of healthy tissue surrounding the patient. Histology does not allow for multi-directional viewing[109]. Furthermore, histology can be a labour-intensive process that is carried out externally to the operating room.

By developing a novel *ex-vivo* imager, it is hoped that FGS could provide the means to assess tumour margins in the operating room thereby improving the outcomes of the surgical procedures.

2. FGS Calibrator

2.1 Introduction

In this chapter, the development of the FGS calibrator will be discussed starting from the initial design considerations, to the final testing and first use of the device on an in-house built clinical FGS imager[110].

The purpose of the FGS calibrator is to provide a means of measuring the performance characteristics of commercially developed clinical fluorescence imagers in SI units. The performance characteristics in question are:

- The detection sensitivity to near infrared (NIR) photons from a quasi-hemi-isotropic source at a specified working distance (defined here as the photon flux at the Rose criterion[(ref. 111, 112) †††]), measured in photons/s/cm^2.
- The amount of useful fluorescence excitation light delivered as a function of working distance, expressed as an intensity, in units of mW/cm^2.

These characteristics are not typically quoted by manufacturers and as such, it becomes difficult for decisions to be made on which imaging system is appropriate for a particular application. Furthermore, it is difficult for clinicians to compare marker performance across different systems, since there is a lack of quantification. This is something that would be highly desirable in FGS as it would allow for better understanding of the biological processes governing marker performance. References to the need for a calibration standard in FGS have been made in the literature[113, 101,

††† The Rose criterion is defined as the minimum SNR needed to discern image features from the background.

[114]. Published reports of calibration systems used for FGS have so far consisted of fluorescent phantoms or quantum dot solutions. In this chapter the design and development of a new type of calibration device is discussed.

2.2 FGS Calibrator Design

The calibrator is a small, portable electro-optical device that consists of three separate units, as well as a spectrometer. These were developed separately, to form the overall calibration system. Excluding the commercially developed spectrometer, the calibrator consists of a control module, an emitter module and a detector module. The detector module is a wide dynamic range, calibrated light measurement unit, the emitter module provides a known light intensity across a given angle and the control module includes additional electronics to allow interface of the other two modules to a host PC via a USB interface.

The aforementioned spectrometer is a Qmini spectrometer from RGB-photonics[115]. The device is a miniature spectrometer suitable for NIR applications with a spectral resolution of 0.3 nm. The original plan was to integrate the Qmini spectrometer into the rest of the calibration system. However, due to time constraints and issues with integrating the spectrometer software into the main calibrator software, the spectrometer was used as a standalone device.

2.2.1 Detector Module Design

The detector is designed with two important functions in mind. The primary function of the device is to allow quantification of the intensity of an FGS imager excitation light source. This measurement is conducted as a function of working distance (with an inverse square law relationship expected). This enables surgeons to know the amount of light available for excitation of the fluorescent probes being used in the surgical procedure. The second purpose of the device is to calibrate the emitter module in terms of the intensity produced from the emitter pinhole (discussed later).

The completed detector module is shown in Figure 5. The components of the detector are housed in a small hand-held enclosure (of outer dimensions 55 mm × 81.5 mm), for ease of measurement on large and sometimes unwieldy FGS imaging platforms.

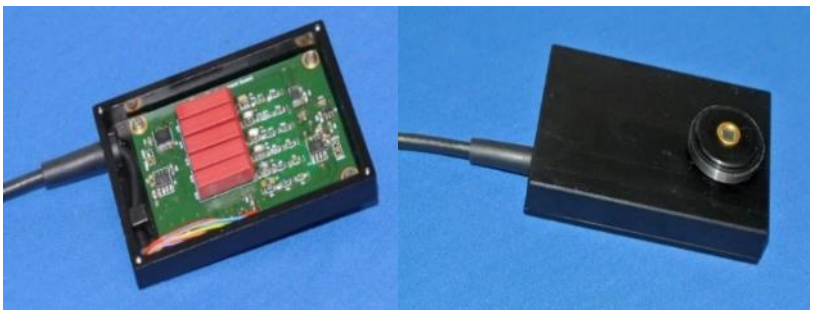


Figure 5: Completed photodiode detector module.

For this application a commercial off the shelf photodiode is used as the photodetector, specifically the Thorlabs® FDS100-CAL[116]. A photodiode is particularly useful for this application since most photodiodes are sensitive in the near infrared[117, 118, 119]and are able to provide the appropriate detection sensitivity. Furthermore, in the case of the photodiode used here, its output current is calibrated by the manufacturer, with the corresponding responsivity spectrum as shown in Figure 6.

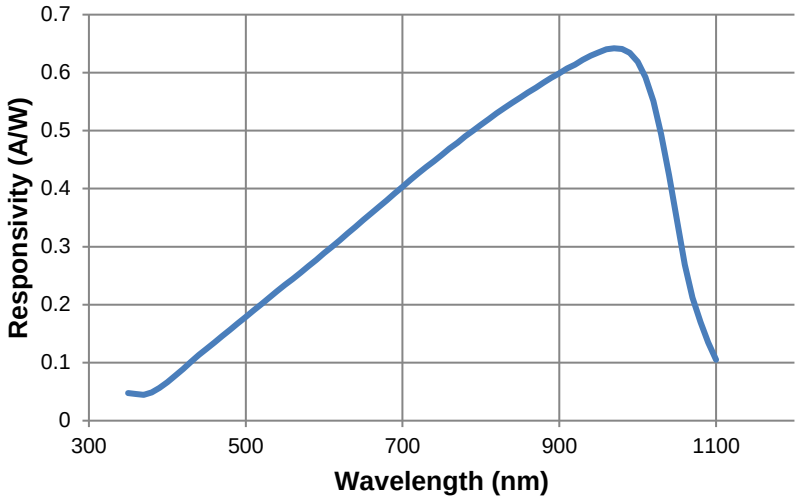


Figure 6: Calibrated responsivity spectrum of the FDS100-CAL, provided by Thorlabs® for the specific device used.

Due to the dual purpose of the detector module a large dynamic range is required. It should be noted that it is possible to obtain an off-the-shelf power meter possessing a large dynamic range but for this application it is was deemed to be more useful to develop a detector from scratch. This is because it is easy to adjust the design of a purpose-built detector (if required) and a purpose-built detector can be designed to integrate specifically with the emitter module for the purpose of calibrating the emitter (described later).

On its own the photodiode can provide the dynamic range required but its output current is low, requiring amplification. This was provided by a transimpedance amplifier circuit. This circuit allows the sensitivity to be varied using a programmable feedback resistance which, in conjunction with analogue to digital conversion can provide a total dynamic range of ~10^6:1. This dynamic range was deemed to be ample to cover the range of outputs from both the emitter module and the variety of FGS imager excitation light sources the device can be expected to encounter.

The sensitivity range switching in the detector module is carried out by a system of 5 relays, providing 6 separate sensitivity ranges. The relays are switched programmatically by a host PC through an interface device (the control module). The detector is designed to offer a range-range sensitivity ratio of 16, which equates to a 16 fold increase in sensitivity when switching from one sensitivity rating to the next more sensitive rating (which was experimentally tested as described later), this has been done deliberately to make digitisation of the signal at the output end more convenient for processing in the controller module's PIC (Programmable Intelligent Controller). A block diagram outlining the interrelation of the main electronic components housed within the device can be seen in Figure 7.

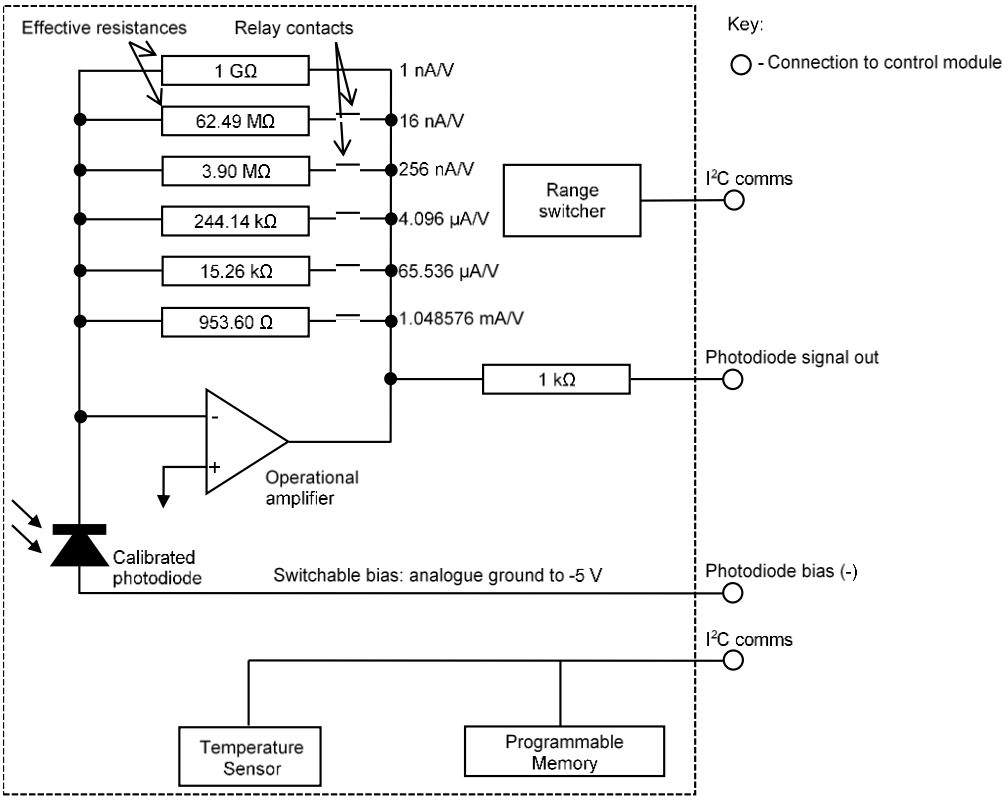


Figure 7: Block diagram demonstrating how the detector works as a current to voltage convertor to measure the light level incident on the photodiode. A 10^6:1 dynamic range is achieved through 16:1 feedback resistances in the transimpedance amplifier circuit. The output signal is digitised using a 16-bit analogue-to-digital convertor (ADC) in the control module (described later).

As shown in Figure 7, the device houses a temperature sensor[120] and a programmable memory known as an EEPROM (electrically erasable programmable read-only memory)[121]. The temperature sensor provides a measure of the temperature of the internal environment of the detector. It is important to monitor the temperature as it is reported that photodiode responsivity changes as temperature varies. Specifically, the responsivity of a photodiode can increase or decrease by as much as 1 % per degree temperature change depending on the wavelength[122]. However, since the device will be used in environments of stable room temperature, responsivity variations as a result of temperature fluctuations is unlikely to be an issue.

The programmable memory (EEPROM) serves to store the responsivity spectrum and other variables required to calculate the intensity incident on the photodiode. At this stage the intensity is calculated for the peak excitation wavelength of the excitation source but it could be possible to calculate the intensity from the spectrum of the excitation light in the future.

2.2.2 Emitter Module Design

The emitter module was the next module to be developed and is now described. The purpose of the emitter module is to provide a precisely adjustable, quasi-hemi-isotropic light source which can be varied in brightness programmatically.

The emitter is designed to enable characterisation of the detection limits of an FGS imaging system with different wavelengths. Since many different packages are available commercially at low cost, with a wide variety of useful wavelengths, LEDs were chosen as the desired light source. To enable the emission wavelengths to be easily modified, the driver for the LED is mounted on a printed circuit board that can be detached from the rest of the system, this is named the LED driver board. The LED driver houses a (feedback) photodiode[123], which is optically coupled to the LED and functions to monitor the brightness of the LED so that it may be compared to the LED setpoint. Any difference in the expected brightness (as set by the LED setpoint) and the actual LED brightness (as measured by the feedback photodiode) is used to adjust the brightness of the LED until the difference is effectively 0. This ensures that the LED brightness increases linearly with increasing LED setpoint voltage. To measure the LED current, a resistor (current sense resistor) has been placed in series with the LED. The LED current is measured by measuring the voltage across the resistor and dividing by the resistor (1 Ω) to determine the current. The emitter block diagram outlining the interrelation of the main electronic components housed within the device can be seen in Figure 8.

The feedback loop's setpoint is defined by an analogue-to-digital converter (ADC) housed on the LED source board (which is fixed in place as opposed to the

removable LED driver board). This setpoint is defined by a 16-bit digital number, generated in the host PC. This digital number is converted to an analogue voltage signal (LED setpoint voltage) which sets the LED brightness.

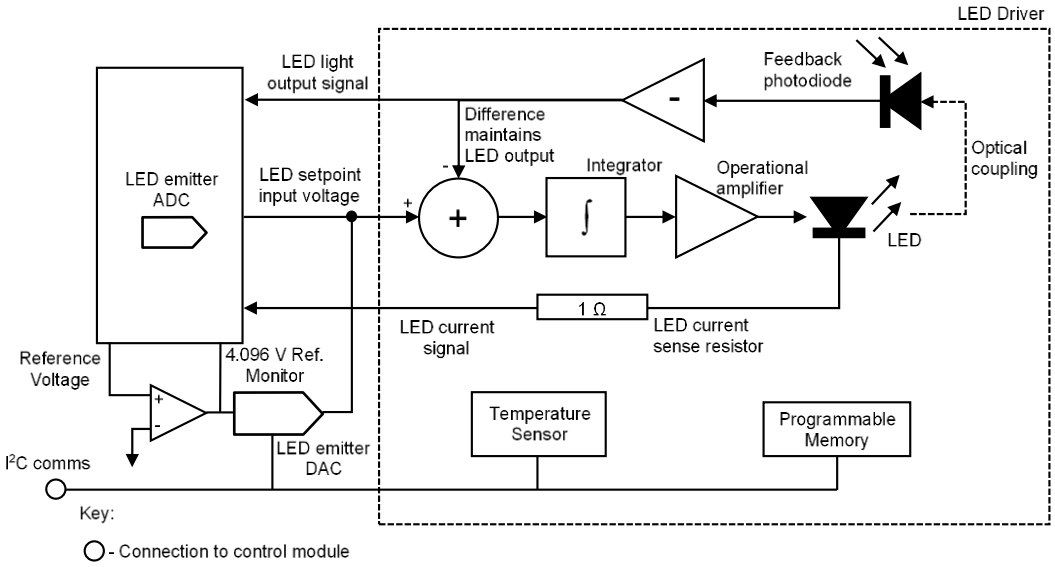


Figure 8: Simplified block diagram demonstrating the key internal components of the LED emitter module, designed to ensure linearity of the LED light output with increasing setpoint input.

As with the detector module, the LED emitter module houses a temperature sensor and a programmable memory (EEPROM). The temperature sensor monitors the temperature of the LED drive board, with each different LED drive board possessing its own dedicated temperature sensor. It is important to monitor the LED temperature as, if the LED temperature increases, the spectral characteristics change[124, 125], which must be avoided or compensated for. The programmable memory (EEPROM) stores information concerning the specific LED inserted into the emitter module. Such information includes the required LED supply voltage, the emitter module ADC reference voltage, the maximum LED current, the maximum LED temperature, the value of the resistor used to monitor the LED current (LED current signal in Figure

8) and finally the spectrum of the LED (used as a reference of the LED inserted into the module).

In addition to the LED, the emitter module is constructed in a way to allow additional optical components to be placed in front of the emitter. Such components include opal glass optical diffusers, neutral density filters and a 1000 μm diameter precision pinhole[126], as shown in Figure 9. The opal glass diffusers introduce even scattering to create a near-Lambertian source at the output of the diffuser[127] and the neutral density filters allow the emission of the LED to be reduced[128] to allow highly sensitive imagers to be calibrated by this device. Furthermore, the diffusers, neutral density filters and pinhole also serve to isolate the internal emitter module circuitry from the outside world to prevent stray light from coupling into the feedback system of the LED driver, causing a reduction in LED brightness. Altogether, the components contribute to reduce the amount of light that can enter the aperture and couple to the LED feedback diode by a factor of $\sim 10^6$.

The diffuse emission produced by the emitter is analogous to the diffuse emission from a fluorophore on or under the surface of a biological tissue sample. The completed device can be seen in Figure 10.

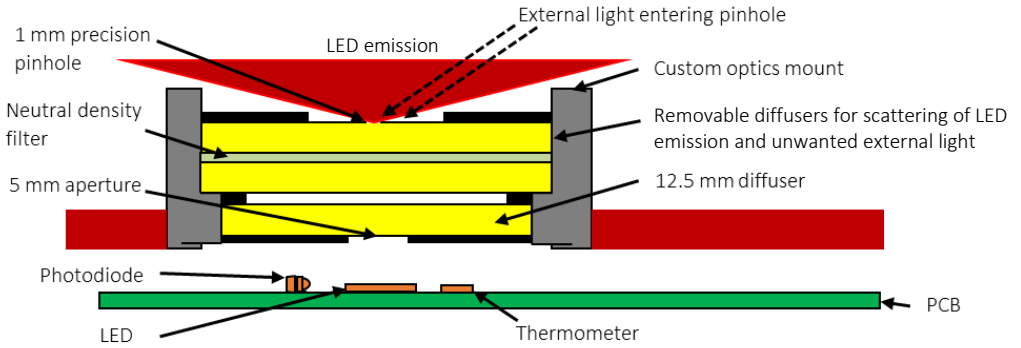


Figure 9: Schematic demonstrating how the case of the emitter allows for the insertion of diffusive optics into a mount situated above the LED. The above layout of optical components is merely an example of what may be used, although any number or combination of filters and diffusive optics may be placed in front of the LED depending on the needs of the system. By introducing these optics after the LED, the emission becomes quasi-hemi-isotropic ensuring that the emission intensity does not vary as a function of angle.

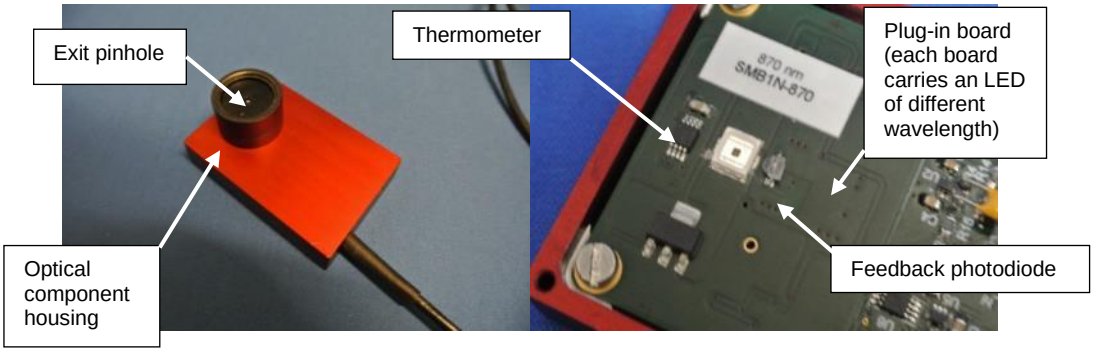


Figure 10: *Left*: The completed emitter module (of dimensions: 55 mm × 81.5 mm). *Right*: LED driver circuit board with feedback photodiode and thermometer. The feedback photodiode monitors the LED output and compares it to the user defined setpoint to ensure that the brightness can be varied in a linear manner.

2.2.3 Control Module and Software Design

The control module is the hardware interface between the emitter and detector modules and the host PC, also functioning as the power supply of the calibrator. A PIC, a Programmable Intelligent Controller based on a reduced instruction set microcontroller[129], housed in the module, contains the firmware used to carry out all device functions. A block diagram of the interface between the control module and the detector and emitter modules is shown in Figure 11. The completed module can be seen in Figure 12.

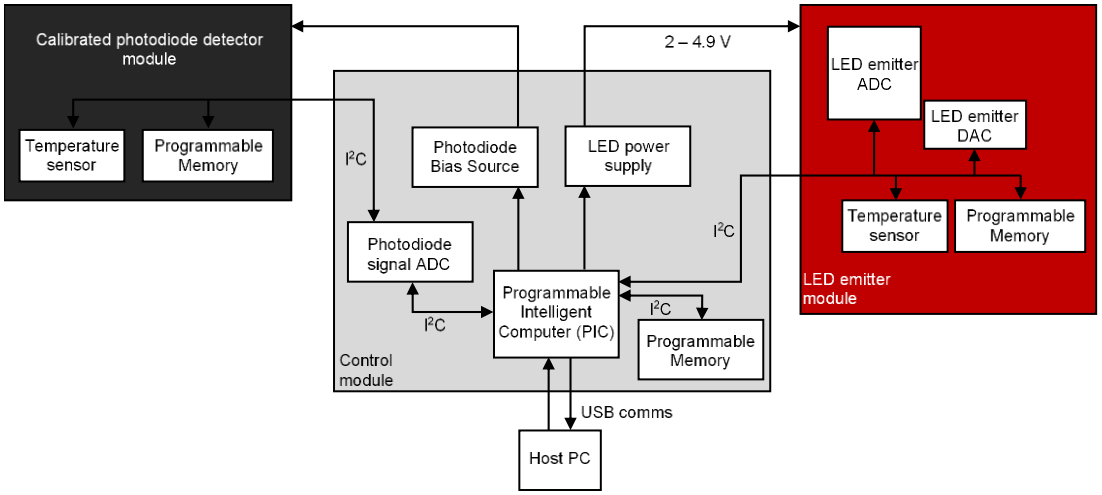


Figure 11: Block diagram demonstrating the interface between the host PC and the calibrated photodiode detector module and LED emitter module.

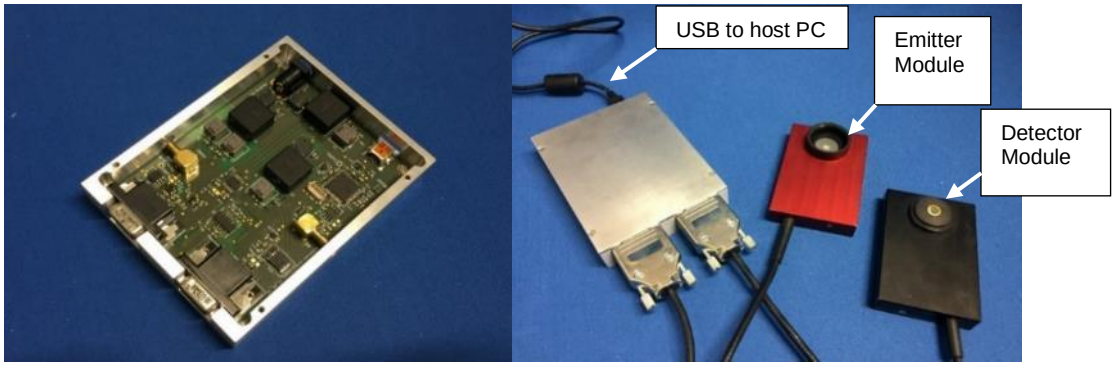


Figure 12: The completed control module connected to the measurement modules.

As shown in Figure 11, the control module houses an analogue to digital converter (ADC)[130] which converts the analogue photodiode output voltage (from the detector module) into digital form for processing in the PIC. As with the emitter and detector modules, the control module also houses a programmable memory (EEPROM) which is used to store variables such as the photodiode signal ADC offset which requires subtraction of the photodiode signal from the detector module and actual ADC sensitivity.

The primary component of the control module is the PIC that processes all data going into and out of the calibration device, acting as the hardware interface between the calibrator and the host PC. The primary task of the PIC is to process the data that are sampled from the detector and emitter modules. The PIC also serves to issue commands to the emitter and detector modules.

The total amount of time that the PIC allocates to handling data and processing incoming commands from the host PC is 300 ms. This ensures that the sampled data is updated at a frequency of approximately 3.33 Hz. This bandwidth was chosen for convenience, since it would allow users to easily detect changes/fluctuations occurring in the measurement whilst not being too slow to update.

The 300 ms PIC cycle is split into three blocks of equal time (100 ms) for convenience and to make the PIC firmware easier to implement. The first block of 100 ms is devoted to the sampling of the photodiode output voltage signal, which is sampled 1024 times at a sampling frequency of 10 kHz. The second 100 ms is devoted to the sampling of the detector and emitter module temperatures (sampled

only once in the 300 ms schedule) and then following this, sampling of the LED module data. The third and final 100 ms is devoted to the communications between the control module and the host PC via USB[‡‡‡]. When the communications are complete, the device is essentially idle for the remainder of the sampling schedule.

This schedule is briefly summarised in Table 2.

Block 1 (100 ms elapsed)	Block 2 (200 ms elapsed)	Block 3 (300 ms elapsed)
Sample the photodiode output voltage signal, averaged 1024 times	Sample module temperatures once and then sample LED emitter diagnostic data (each channel averaged 64 times)	Send the data as a formatted string through USB to host PC and remain idle for other tasks

Table 2: Firmware data sampling and communication schedule in the PIC of the control module.

The sampling of the detector photodiode output voltage signal is carried out using a 16-bit analogue-to-digital converter (ADC). The number of samples acquired is set to 1024 since it is more convenient for the PIC to handle divisions by 2^n required during averaging (in this case n = 10).

The process of sampling the photodiode output voltage signal is the main I^2C communications that occur between the PIC and the detector module. In addition to this, the relatively infrequent processes of writing and reading from the detector module memory (EEPROM), setting the photodiode sensitivity and reading the temperature from the device's thermometers take place.

‡‡‡ USB communications do not require this long, however 100 ms was devoted to the communications between the PIC and PC for symmetry (to ensure easier implementation of PIC firmware).

The sampling process for the LED module data is similar to the sampling process for the photodiode output signal. The process differs only in the respect that the LED module has 8 channels (LED supply voltage, LED light output, LED setpoint input voltage, LED ground, LED current, LED return, reference voltage and digital ground) that are sampled in 100 ms. This equates to 1024 samples in total, across 8 channels each individual channel is sampled 64 times.

The data that are sampled from the detector and emitter are sent via USB to the host PC where the data are then displayed on the host screen. The host software is written in CVI/LabWindows™ [131], used to display and process data from the device but also to issue commands to the device when required. The graphical user interface (GUI) of the host PC software can be seen in Figure 13.

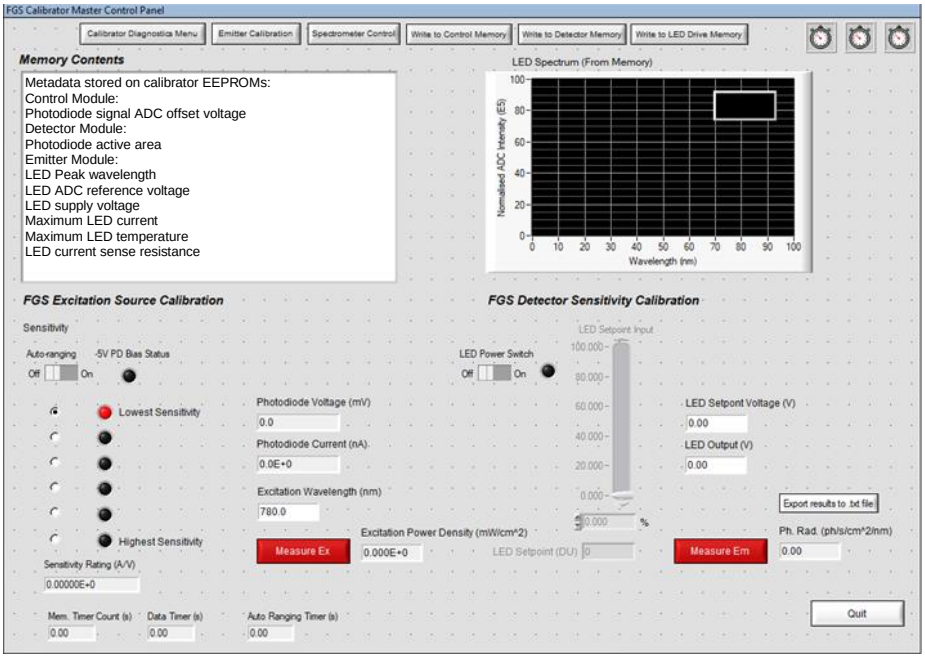


Figure 13: Front panel of the graphical user interface of the FGS calibrator software (operated from the host PC).

On start-up, the host CVI software issues a command to the PIC to initiate the process of reading the contents of the device EEPROMs (programmable memories) and to transfer the data to the host PC. These data are important as they contain pre-determined sensitivity range offsets for the detector module (for subtraction from the photodiode signal) as well as spectra for reference.

The white text box situated at the top left of the GUI displays metadata concerning the control, detector and emitter modules, stored in the EEPROMs (memories), to the user for reference. These metadata consist of the control module offset voltages; photodiode active area size, sensitivity values of each detector sensitivity range; LED peak wavelength; LED supply voltage; maximum LED current; maximum LED temperature and the LED current sense resistor value. The top right of the GUI displays the spectrum of the LED installed in the device for reference. This spectrum was experimentally measured by the Qmini spectrometer and then written to the memory (EEPROM) starting with the wavelengths and then the corresponding intensity values line by line until the entire spectrum is stored. In the future this spectral data could be used to more accurately determine the photon flux being emitted from the LED rather than serving simply as a reference but due to time constraints this has not been implemented here.

The sensitivity of the photodetector module is set using the controls in the bottom left of the GUI with an option to switch the detector to an auto-ranging mode. When in auto-ranging mode the output signal voltage from the photodiode is compared to an upper limit (15/16 of the total signal) and a lower limit (1/16 of the total signal). If the photodiode output voltage lies between the upper and lower limits, then the

device remains in the currently selected sensitivity range. If not, then the range is adjusted accordingly (either switching to the next most sensitive range or the next least sensitive range). Additionally, the CVI code contains a system for preventing the device from switching between ranges too quickly. This system requires that the signal exceed one of the limits for a set number of cycles, in this case the number is set to 5 but this can be changed in software. If auto-ranging is not required, this can be switched off by clicking the auto-ranging switch in the CVI software.

The LED is controlled using the lower right-hand side of the GUI with the slider which sets the brightness of the LED. The two buttons on the GUI labelled '*Measure Ex*' and '*Measure Em*' are used to produce the output measurements which form the calibration measurements. The '*Measure Ex*' button converts the photodiode output signal current into a measurement of the intensity incident on the surface of the photodiode at the working distance of the detector from the source. The photodiode current is calculated from the output voltage signal by multiplying the voltage by the sensitivity rating of the detector in A/V. Then the intensity is calculated from the current using the following equation:

$$I = \frac{i_{PD}}{\Re(\lambda) \cdot A} \tag{1}$$

Where I is the intensity in units of W/cm^2, $\Re(\lambda)$ is the responsivity of the photodiode in A/W as a function of the wavelength (λ) and A is the active surface area of the photodiode (in this case nominally specified by the manufacturer as 0.13 cm^2).

$i_{PD}/\Re(\lambda)$ represents the power measured by the photodiode in W and the area of the photodiode converts this measured power into an intensity.

The responsivity as a function of wavelength is stored as a spectrum in the memory of the detector module. When the user wishes to measure the intensity, the wavelength range must be correctly specified such that the response over that wavelength range (in units of A/W) can be determined from the aforementioned photodiode responsivity spectrum.

The '*Measure Em*' button converts the LED setpoint voltage set by the user into a photon flux produced by the LED emitter module (in units of photons/s/cm^2) at a specific wavelength. The LED setpoint is converted into a photon flux (φ) by substituting the LED setpoint voltage ($V_{setpoint}$) into the calibration equation:

$$\varphi = aV_{setpoint} \tag{2}$$

Where a is the calibration coefficient. The value of a (unique to every LED wavelength and thus LED) is stored in the memory (EEPROM) of the LED drive. The method for determining the calibration coefficient is described next.

2.3 Calibration of the LED Emitter

To allow conversion of the LED setpoint into a photon flux the conversion coefficient requires determining. This is achieved using the detector module.

The calibration process first involves attaching the detector module to the emitter as demonstrated in Figure 14.

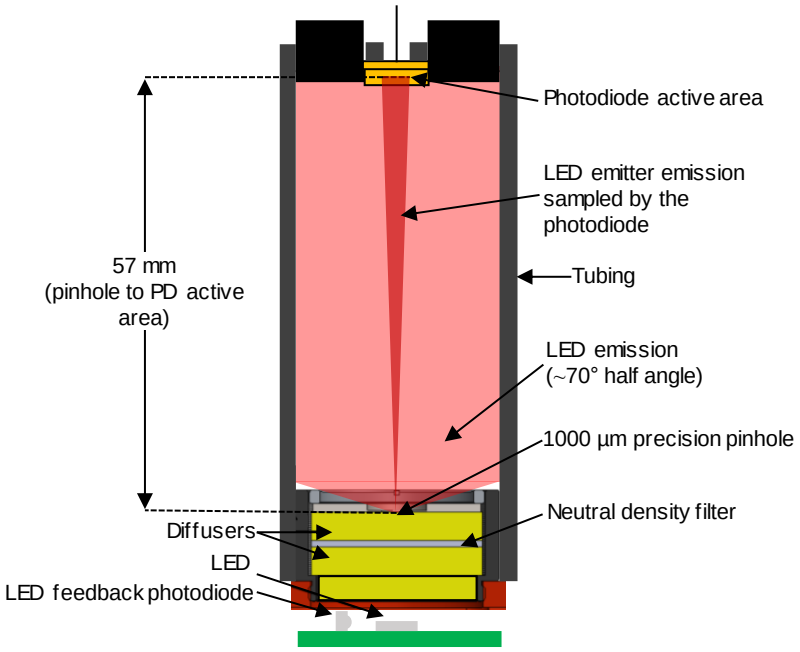


Figure 14: Emitter calibration setup (schematic). The detector module is attached to the emitter module with the diffusive optics in place and the detector calculates the intensity at various LED outputs to determine the photon flux produced by the LED module at a certain working distance (in this case 57 mm).

The setpoint voltage of the LED is increased incrementally and the intensity at each LED setpoint is determined from equation (1). The photon flux at a particular given working distance is then calculated using the following equation:

$$\varphi_{Emitter} = I_{Emitter} \cdot \frac{\lambda}{hc} \tag{3}$$

Where $\varphi_{Emitter}$ is the photon flux of the LED emitter, $I_{Emitter}$ is the intensity of the LED emitter and λ is the wavelength, h is Planck's constant and c is the speed of light in vacuum (essentially the same as in air as used in these experiments).

By knowing the photon flux at each corresponding LED setpoint voltage, the conversion coefficient a can then be determined from plotting the photon flux as a function of LED setpoint voltage.

2.4 FGS Calibrator Testing

2.4.1 Detector Module Sensitivity Calibration

To ensure accurate calculation of the photodiode current from the output voltage signal, the sensitivity values of each sensitivity range had to be calibrated. In practice this involved measuring the sensitivity of the most sensitive range in A/V and then measuring the ratio of the output voltages between the other ranges. From this, all sensitivity ratings values can be calculated. The range-to-range sensitivity ratio should be 16:1 by design, but these deviate due to the limited tolerance of the feedback resistors. The experiment involved increasing the brightness of the LED emitter module from zero until the detector module reached near full scale at a given range. For each brightness, the detector output signal voltage was measured for two adjacent sensitivity ranges and the ratio between the two output signal measurements was calculated. The outputs were plotted against each other, with the gradient of the linear plot being the ratio between the two sensitivity ranges. This process was repeated for all ranges, the aforementioned plots can be seen in Figure 15 and the final results can be seen in Table 3.

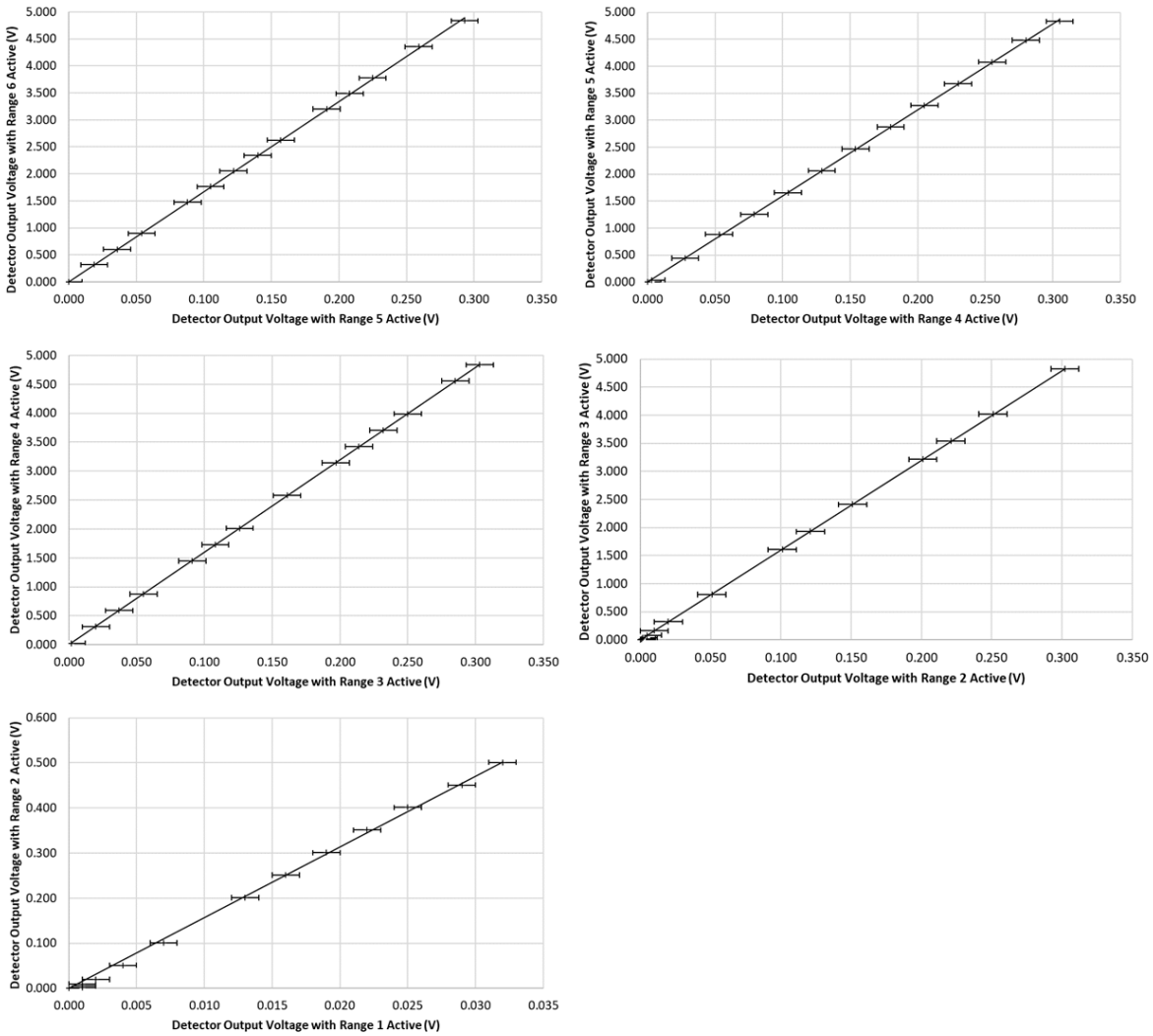


Figure 15: Plots used to determine the FGS calibrator detector module output voltage ratios between adjacent sensitivity ratings (see Table 3), the error bars denote the standard deviation in *x* and *y* (the error in *y* is not visible on this scale), with each reading being generated by the mean of 5 measurements. *Top left*: Plot used to determine the ratio between sensitivity range 6 and range 5. *Top right*: Plot used to determine the ratio between sensitivity range 5 and range 4. *Middle left*: Plot used to determine the ratio between sensitivity range 4 and range 3. *Middle right*: Plot used to determine the ratio between sensitivity range 3 and range 2. *Bottom left*: Plot used to determine the ratio between sensitivity range 2 and range 1. Note: The scale on the bottom left plot is different from the other plots since the emitter module could not produce enough light to use the full dynamic range at these sensitivities.

Range Ratio	Average Output Ratio (± 0.5)
Range 6 : Range 5	16.7
Range 5 : Range 4	16.0
Range 4 : Range 3	16.0
Range 3 : Range 2	16.0
Range 2 : Range 1	15.8

Table 3: Output ratios between each range, used to calculate the sensitivity in A/V for each sensitivity range.

From Table 3 it can be seen that the signal output ratio between each range is 16 with a tolerance of approximately 1%, which matches the tolerances of the resistors used. The exception is the ratio between sensitivity range 6 (the most sensitive range) and sensitivity range 5 (the second most sensitive range). This discrepancy is most likely due to the fact that 1% tolerance resistors were not available in sizes of 1 GΩ. However, this can be readily corrected in software when switching ranges using the above values stored in memory (EEPROM).

2.4.2 LED Emitter Module Testing and Calibration

Using the setup outlined in Figure 14, the LED module was calibrated for several wavelengths (690, 780 and 880 nm). The method involved increasing the intensity of each LED from 0% output to 100% output in incremental steps while the photodiode output voltage was recorded. The photodiode voltage was converted into a current using the sensitivity rating of each sensitivity range of the detector module. The signal current of the photodiode detector module is plotted against the setpoint input voltage of the LED, the results are plotted in linear space in Figure 16. Plots in log-log space are included in Figure 17.

During the course of the experimental testing of the LEDs, the LED currents and temperatures were recorded at each LED setpoint input. This was to check that the LED current was not approaching the quoted maximum current of each LED which would cause excess power consumption leading to a rise in the temperature of the LED. The maximum current ratings and the maximum currents that the LEDs were operated at are included in Table 4. For each LED, it was noted that no significant temperature rise occurred. If a significant temperature rise was to occur, then switching off the LED until the temperature returned to room temperature is the easiest solution.

LED Serial Number	LED Wavelength (nm)	Maximum LED Current Rating (mA)	Maximum LED Operating Current (mA)
SMB1N-690D-02	690	600	207
SMB1N-780D-02	780	800	121
SMB1N-880D-02	880	1000	204

Table 4: LEDs used in the emitter module of the FGS calibrator during calibration of the emitter and their maximum current ratings as well as the maximum currents the LEDs were operated at.

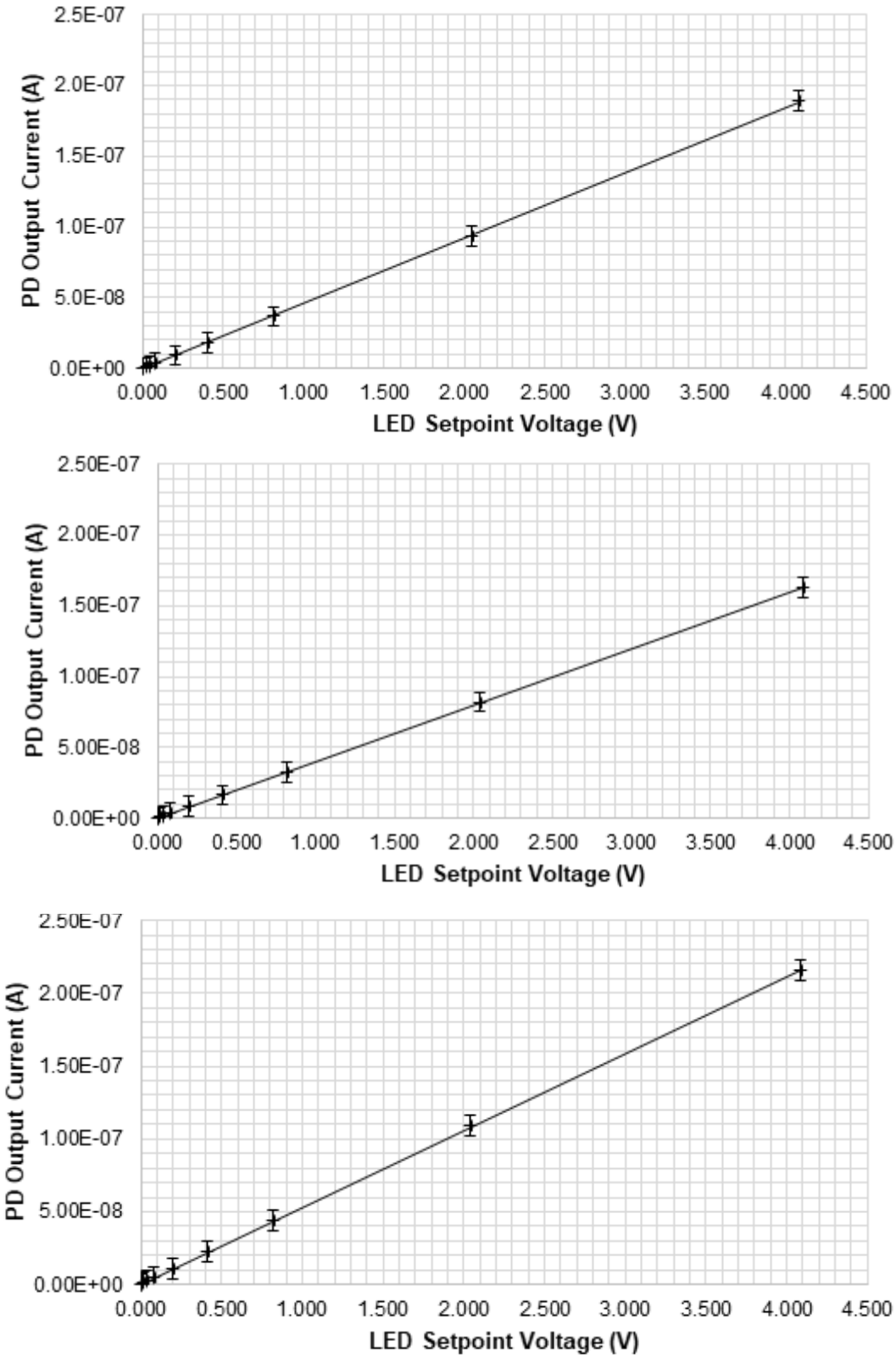


Figure 16: *Top*: Photodiode output signal voltage as a function of the LED setpoint voltage for 690 nm LED in linear space. *Middle*: Photodiode output signal voltage as a function of the LED setpoint voltage for 780 nm LED in linear space. *Bottom*: Photodiode output signal voltage as a function of the LED setpoint voltage for 880 nm LED in linear space. Note: The error bars are defined by the standard deviation, with each reading being generated by the mean of 5 measurements.

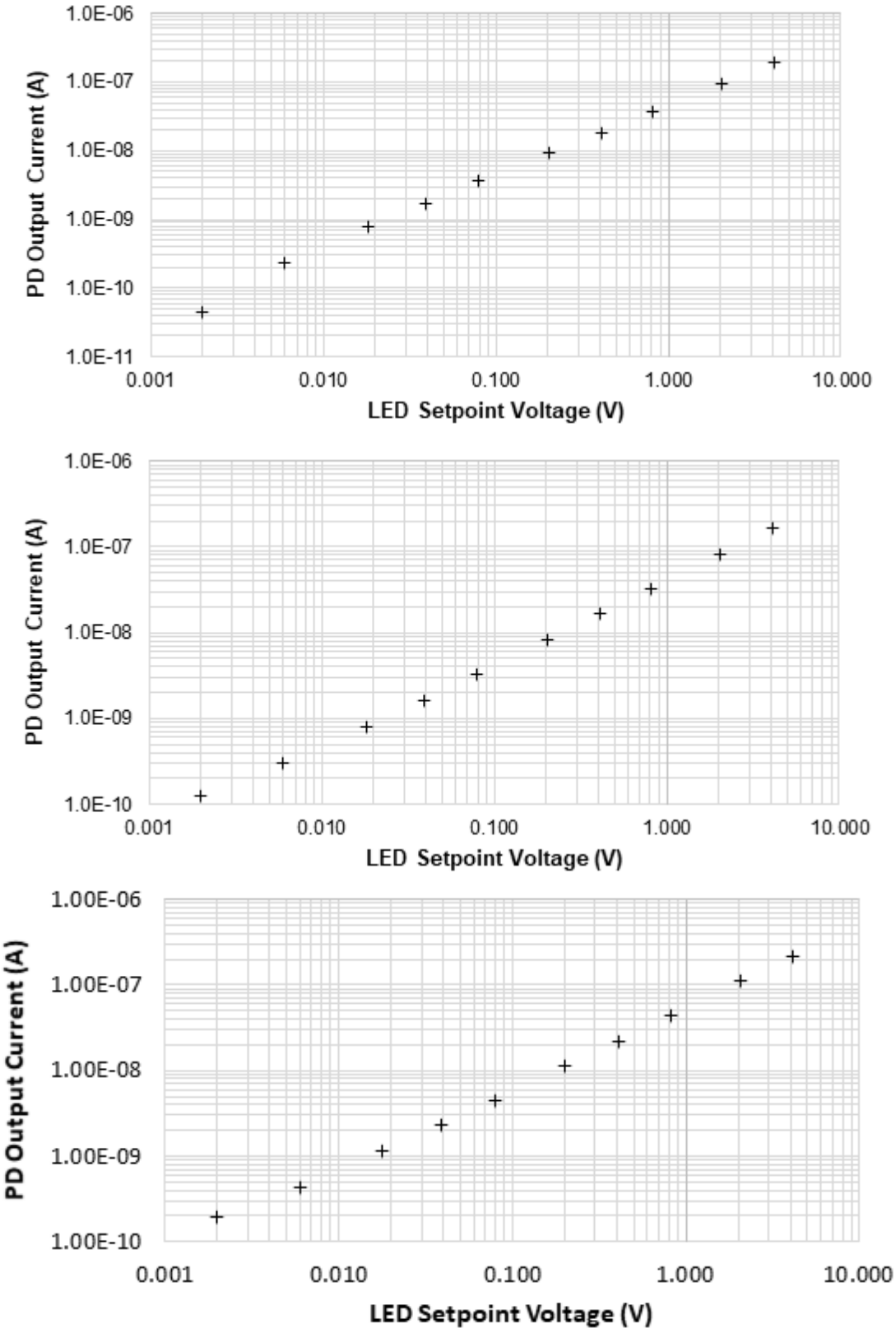


Figure 17: *Top*: Photodiode output signal voltage as a function of the LED setpoint voltage for 690 nm LED in log-log space. *Middle*: Photodiode output signal voltage as a function of the LED setpoint voltage for 780 nm LED in log-log space. *Bottom*: Photodiode output signal voltage as a function of the LED setpoint voltage for 880 nm LED in log-log space. Note: the error bars have been omitted from these plots to make it easier for the reader to see the data points.

From the linear fits to the data for each LED in Figure 17, the conversion coefficients were calculated from the gradients of each line. These are included in Table 5.

LED Wavelength (nm)	LED Setpoint Voltage to Current Conversion Coefficient (± 0.01) $\times 10^{-8}$ (A/V)
690	4.62
780	3.98
880	5.29

Table 5: LED setpoint voltage to current conversion coefficients for each LED, calculated from the graphical data in Figure 16.

As a check, the non-linearity of the LED emitter module was determined by calculating the percentage difference of the recorded photodiode output signal from the ideal linear fit to the data. In the case of the two LEDs used to generate the non-linearity plots shown in Figure 18.

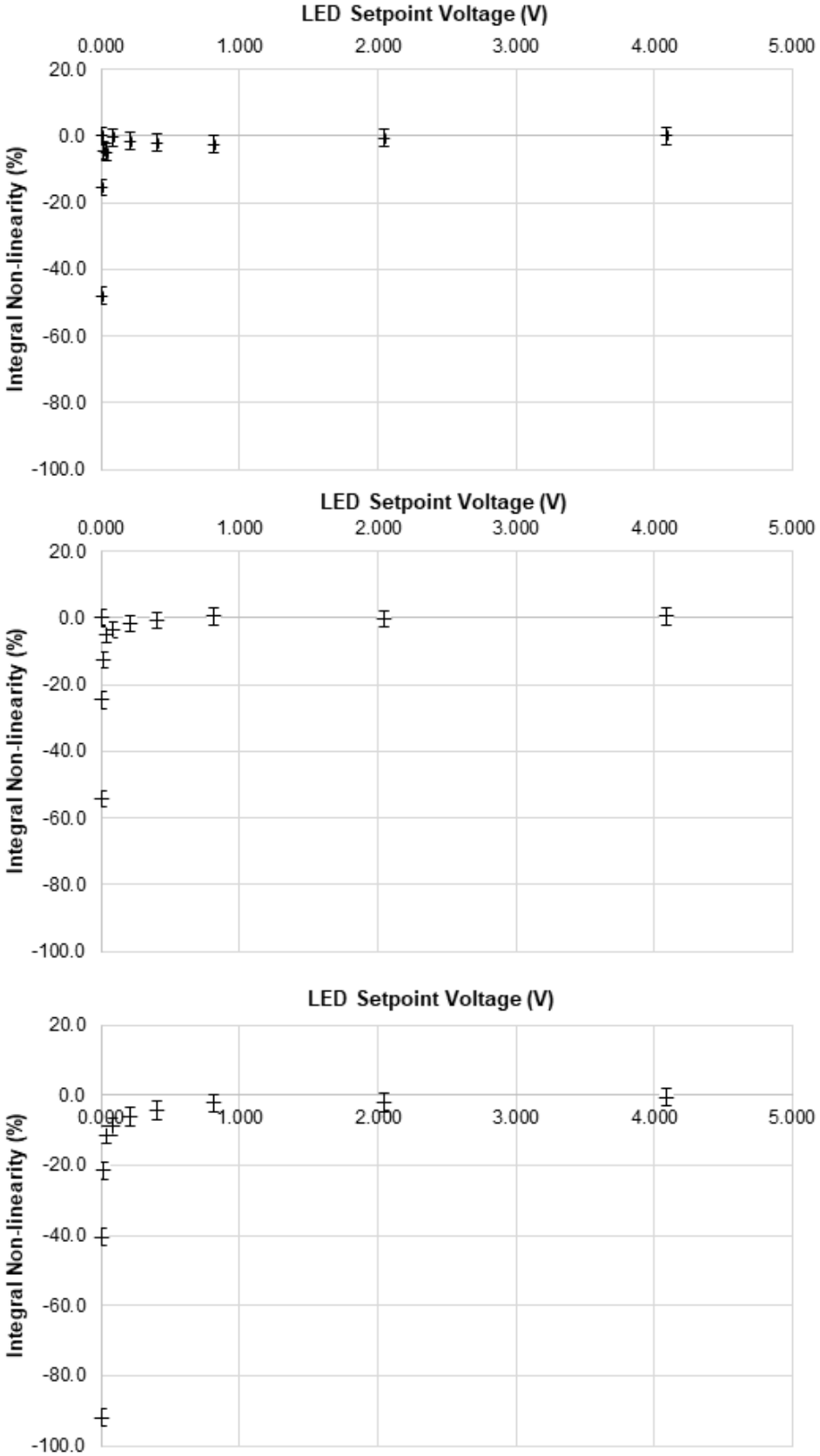


Figure 18: *Top*: 690 nm LED non-linearity calculated as the percentage difference from the ideal linear fit. *Middle*: 780 nm LED non-linearity calculated as the percentage difference from the ideal linear fit. *Bottom*: 880 nm LED non-linearity calculated as the percentage difference from the ideal linear fit. Note: The error bars are defined by the standard deviation, with each reading being generated by the mean of 5 measurements.

As can be seen from Figure 18, the LED source is non-linear at very small setpoint inputs, i.e. below 0.15% of full scale for 690 nm; below 0.44% of full scale for 780 nm and below 1.93% of full scale for 880 nm . This non-linearity may be attributable to the fact that the internal emitter feedback photodiode is not able to measure the light level of the LED at very low light levels, potentially due to poor optical coupling of the LED to the feedback photodiode. Poor coupling would reduce the opto-electrical open loop gain of the system. To improve on this the optical coupling could be improved using optical coupling gel or perhaps even better would be to fit a light guide for example. However, since the setpoints at which the LED operates in a non-linear manner are so low this can be largely ignored. If very low light levels are required from the LED emitter module, optical attenuators in the form of neutral density filters can be placed in front of the LED.

To complete the calibration process, the photodiode current is converted into an intensity before finally being converted into a photon flux using the responsivity spectrum of the calibrated photodiode in the detector module. This is again plotted as a function of the photodiode setpoint input voltage with the linear fit to the data forming the conversion equation used to convert the LED setpoint input voltage into a measurement of the emitter photon flux as shown in Figure 19.

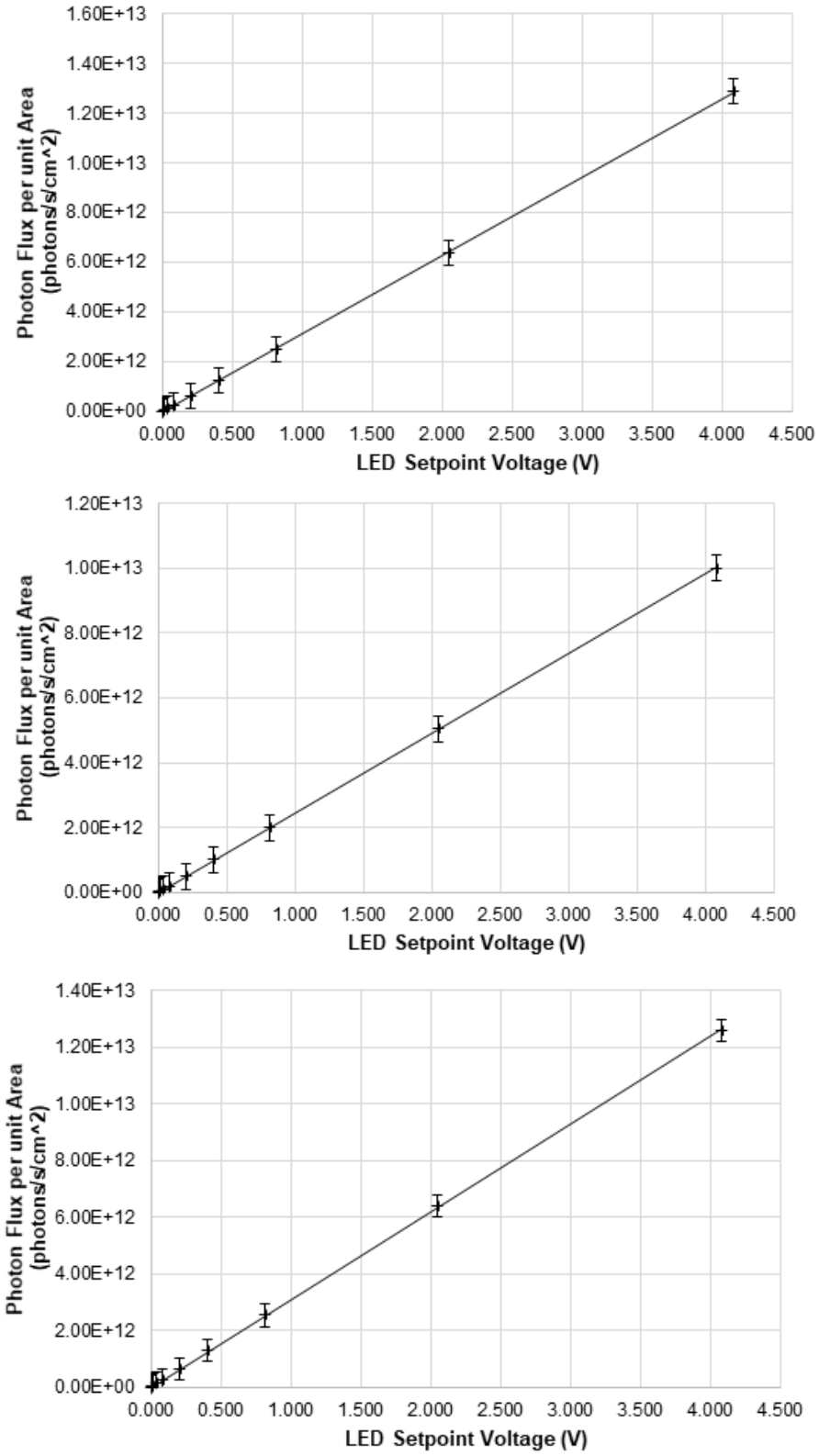


Figure 19: *Top*: Photon flux as a function of LED setpoint input voltage for 690 nm LED. *Middle*: Photon flux as a function of LED setpoint input voltage for 780 nm LED. *Bottom*: Photon flux as a function of LED setpoint input voltage for 880 nm LED. Note: The error bars are defined by the standard deviation, with each reading being generated by the mean of 5 measurements.

The coefficients of the linear fit to the data in Figure 19 are included in Table 6.

LED Wavelength (nm)	LED Setpoint Voltage to Photon Flux Conversion Coefficient (± 0.01) $\times 10^{12}$ (photons/s/cm^2)
690	3.15
780	2.45
880	3.09

Table 6: LED setpoint voltage to photon flux conversion coefficients for each LED, calculated from the graphical data in Figure 19.

The coefficients in Table 6 are stored on the memories (EEPROMs) of the respective LED drive boards so that the photon flux can be quickly calculated from the front panel of the GUI of the host PC software.

2.5 Calibration of an in-house Developed FGS Imager

2.5.1 Excitation Calibration

With the FGS calibrator tested and calibrated, initial calibration measurements could be carried out on an available FGS imager. The obvious choice for this was an in-house developed FGS imager that has been used in theatre[110].

The first stage of the calibration involved the characterisation of the imager excitation light source using the detector module. The setup involved placing the detector module in the centre of the illumination spot of the excitation light source, on a height-adjustable platform to vary the working distance, as shown in Figure 20.

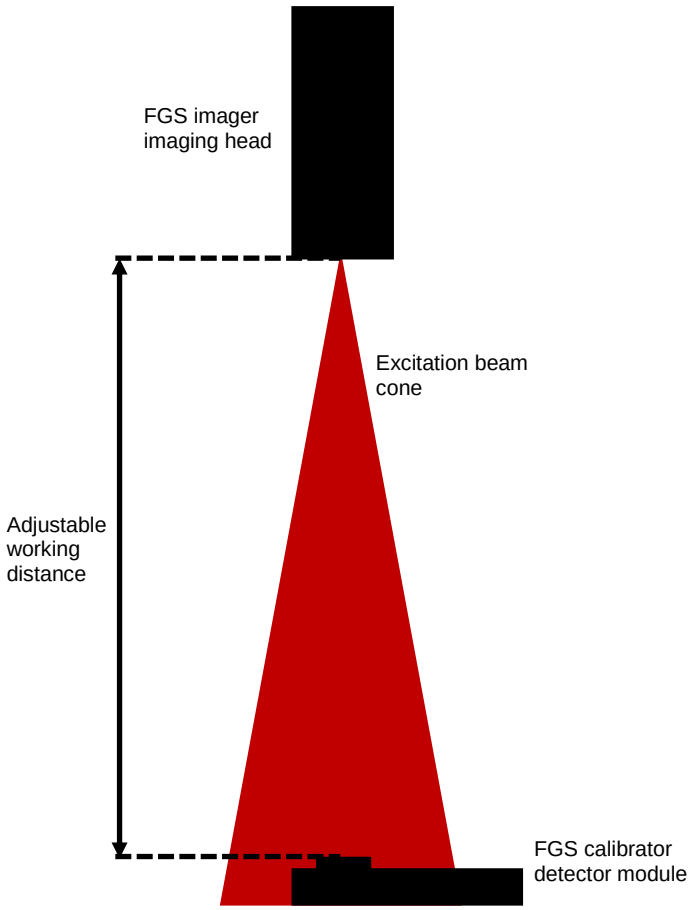


Figure 20: Measurement setup for characterisation of an FGS imager excitation beam (set to a wavelength of 660 nm).

The wavelength of the excitation light is 660 nm. At several working distances the intensity of the excitation beam was measured with the detector module. To eliminate light pollution all measurements were taken with the imager and the calibrator under a dark cover with the room lights off. The output intensity was plotted as a function of working distance and as a function of $1/d^2$ (where d is the working distance), as shown in Figure 21.

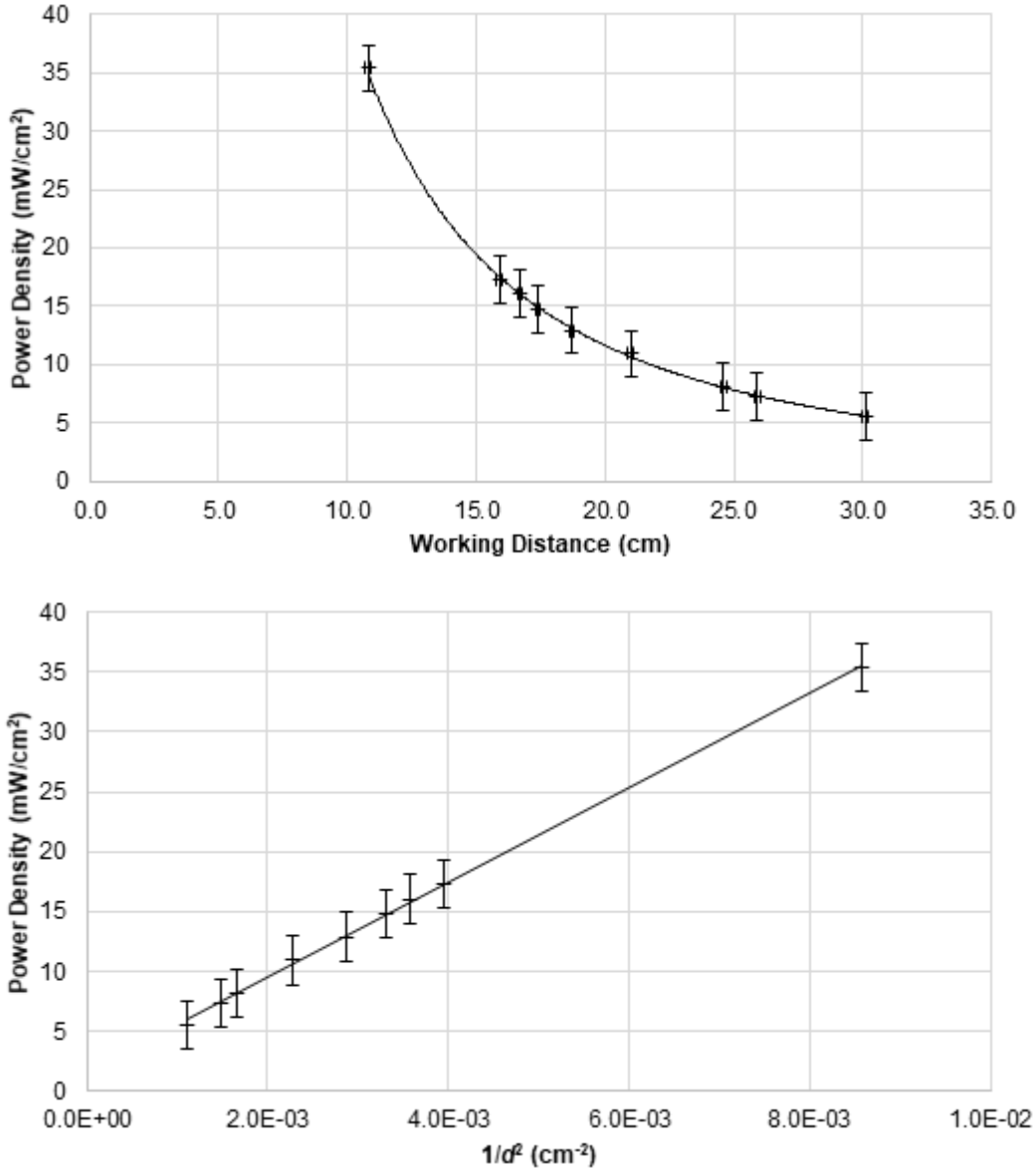


Figure 21: *Top*: Power density as a function of working distance for the excitation system of an in-house developed FGS imager. *Bottom*: Power density as a function of $1/d^2$ for the excitation system of an in-house developed FGS imager. Note: The error bars in *x are* determined from the error in the precision in the rule used to measure working distance, the errors in *y* are defined by the standard deviation with each reading being generated by the mean of 5 measurements. The noise floor has not been included as the detector module can detect power densities much lower than would be visible on the sale of the above plots.

As demonstrated, the excitation light source intensity follows the expected inverse square relationship with increasing working distance. This curve acts as a reference from which the intensity can be calculated from. The excitation light delivered to the sample can therefore be quantified.

2.5.2 Sensitivity Calibration

This section provides further information to the mitigating statement provided at the beginning of this dissertation in reference to disruption caused by the Covid-19 pandemic. This section provides details of the experimental method to be used to acquire data relevant to the sensitivity calibration process of the FGS imager.

Following on from the excitation calibration, the second stage of the calibration process is to determine the sensitivity of the imager to fluorescence photons. For this measurement, the emitter module is placed at a working distance of 57 mm from the head of the imager, which is the same as that of the working distance used to calibrate the emitter module using the detector module. This working distance ensures that the 1000 µm pinhole is visible over a larger number of pixels to avoid measurement error in the image analysis process. The working distance is to be kept constant during the measurement. The experimental setup is summarised in Figure 22.

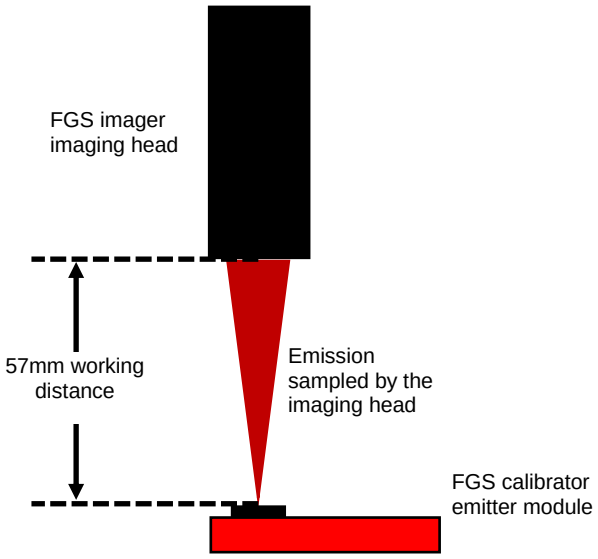


Figure 22: Measurement setup for the calibration of the FGS imager sensitivity to fluorescence emission (not to scale). The working distance is matched to that of the calibration of the LED emitter module using the detector described earlier.

Any number of relevant wavelengths can be used to test the sensitivity of the FGS imager. This depends on the availability of surface mount LEDs for mounting in the emitter module and also depends on the region of the optical spectrum that the imager probes. For this specific experiment, four wavelengths were planned for use to calibrate the sensitivity of the imager, these being 630, 780, 880 and 940 nm. For this particular experiment, it was planned that two reflective neutral density filters (of nominal OD = 2 and 3 respectively) would be inserted into the emitter module in front of the LED to adjust the output of the emitter and ensure the entire dynamic range of the emitter could be utilised. Also, to introduce scatter, an opal glass diffuser can be placed directly in front of the LED.

To effectively determine the sensitivity limit, the camera of the FGS imager requires operating at its most sensitive settings, which in the case of the in-house built imager

discussed here means operating the camera at 4 s integration time and ×10 camera gain.

Using the setup detailed in Figure 22, multiple images are then to be acquired at various brightness settings from 0% up to 100% emitter output. Once all images are acquired gamma corrections must be applied to each image, if required. In this specific case the Sony® XC-505 camera operates at a gamma of 0.45 but in a different FGS imager the gamma settings may be set to be 1 in which case gamma corrections are not required. The gamma process in a camera is the process of encoding the linear response of the CCD chip to increasing light intensity in a non-linear, power law expression which has the following general form[132]:

$$V = aI_{in}^{\gamma} + b \tag{4}$$

Where I_{in} is the intensity incident on the CCD chip (the original signal before gamma correction), V is the voltage or grey level after gamma correction, a and b are arbitrary conversion constants and γ is the gamma factor. A gamma factor of 1 means the intensity in the image captured by the camera is a linear representation of the scene intensity.

Following inverse gamma correction, the images must be analysed in the image processing software of choice, a good example is ImageJ. If the images are obtained using an RGB camera then they must first be converted to grayscale images, this can be done with the inbuilt functions in ImageJ, which enable conversion of RGB images into grayscale.

To obtain the average signal produced by the emitter module a region of interest can be drawn around the illumination spot in each image or thresholding can be used to separate the background from the emitter signal for easy identification of the signal from the background.

To calculate the SNR, the mean pixel value of the emitter signal spot in the image must be divided by the background signal. This can then be plotted as a function of the emission from the emitter, defined as a photon flux (in units of photons/s/cm^2). The sensitivity of the imager can then be defined as the point at which the emission from the emitter module results in a SNR of 5 in the image from the graphical data. The SNR of 5 was chosen as the lower detection limit since this is a conveniently pre-defined threshold, referred to as the Rose Criterion (named after Albert Rose), that is typically quoted as a lower detection limit of SNR. Alternatively, any signal to noise ratio could be specified as the detection limit as long as this is repeated across calibrations.

Following a successful calibration of an FGS imager, the amount of excitation light as a function of working distance is defined and the absolute sensitivity is determined at an SNR of 5. By understanding the amount of excitation light produced as a function of working distance, the surgeon can not only understand how much light is available for excitation of their chosen fluorescent marker but also how much power is being delivered to the patient when operating the device. At a particular working distance, the power density may exceed a predefined safety threshold (leading to higher risk of burning the patient's tissues). The surgeon can therefore reposition the device for improved safety to the patient.

Furthermore, by understanding what is the lower limit of light that is detectable, the surgeon can understand if the selected imager is suitable for the fluorophore chosen for their selected application (when also considering the amount of available excitation light) and can more easily compare results against those achieved with other imaging devices.

In the future, data obtained from calibration of FGS imagers could be used to inform a model which predicts the likely performance of the selected fluorophore and FGS imager. The model could not only be informed by the performance characteristics of FGS imagers but also by the assumed characteristics of the environmental conditions that the fluorophore will be subjected to. Such parameters could include pH, temperature and solvent (which could be varied in the model). As a consequence, the surgeon could understand the likely results of the imaging process even before carrying out any imaging.

2.6 Chapter 2 Summary

In this chapter, development of a novel electronic calibration device for Fluorescence Guided Surgery (FGS) has been described. This device enables characterisation of the excitation intensity provided by the excitation light source (as a function of working distance) and the sensitivity of the detection system. This device aims to provide a service to surgeons conducting FGS experiments through determination of absolute device sensitivity. By understanding the performance parameters of FGS imagers patient safety could be improved and surgeons can make more informed decisions on the suitability of their FSG imager and fluorophore combination (which could be predicted using a computational model informed by calibration data and other relevant biological parameters). Furthermore, comparative imaging could be more easily achieved between different imagers and fluorophore combinations.

This chapter has provided results from an initial test of the calibration device on an in-house developed clinical imager which has been used in theatre. In the case of the sensitivity calibration, the methodology required to obtain the data has been described instead of data, in light of the Covid-19 pandemic (as detailed at the start of the dissertation). Future plans for the use of this device will involve testing on other available in-house imaging systems. Furthermore, the calibration system will be used in commercial systems as they become available.

3. *Ex-vivo* Imager

3.1 Introduction

The success of a surgical procedure is determined by the presence of clear negative margins in a resected tissue sample, which means that no cancer cells are observed to be present at the edge of the tissue sample. On the other hand, positive or close margins suggest that residual tumour remains inside the patient and further resection may be needed.

For many cancer surgeries such as radical prostatectomy (prostate cancer), breast conserving surgery and oral cancer surgery (for example), post resection surgical margins are determined through histological analysis[133, 134, 135], which involves analysing stained sections of tissue microscopically. This process is carried out externally to the surgical procedure by a pathologist.

A desirable feature of FGS technology would be the ability to analyse resected tissue samples *ex-vivo* in theatre, to confirm the presence of clear negative margins on the go. This would increase the probability of successfully carrying out a complete resection of the diseased tissues of interest, thereby improving the outcome for the patient[7]. Histological analysis can then be used to confirm the results achieved with the *ex-vivo* imaging system.

In the past marker specificity has prevented *ex-vivo* imaging from being a possibility. As targeted markers become more widely available, *in-vivo* open surgery and laparoscopic imaging devices can be successfully used but are still limited in their use by theatre lighting interfering with open surgery imaging or by limited sensitivity

of laparoscopic devices (for example). Nevertheless, *ex-vivo* imaging in theatre becomes readily achievable, identifying specific marker accumulation in resected tissues, using optimised imaging.

The purpose of this section of the project is to develop a novel FGS imager to facilitate *ex-vivo* sample analysis in theatre to aid in clinical decision making. The imager will be used in conjunction with existing widefield or laparoscopic FGS imaging technology[110] in theatre. These existing *in-vivo* technologies will continue to be used to identify the tissues for resection and the *ex-vivo* imager used to carry out the post resection analysis. The particular fluorophores identified for use in tandem with the *ex-vivo* imager are included in Table 7.

Fluorophore	Fluorophore Quantum yield (%)	Wavelength Selected for Excitation (nm)
Cy5	26.1[ref 136]	645
Cy 5.5	28.4[ref 70]	645
IRDye 800	10[ref 137, 138]	750/780
ICG	4.3[ref 137,139]	780/808

Table 7: Fluorophores being investigated using the first iteration of the *ex-vivo* imager, including the wavelengths selected for excitation.

The markers in Table 7 are non-specific but the imager is designed with the purpose of imaging specific markers in mind. The concentration of any marker, specific or non-specific may be low in the tissues. In the case of non-specific markers, the reason is obvious, in the case of specific markers, it is more complicated. For any targeted marker, the specificity is never going to be perfect, with non-specific

binding inevitable. To eliminate non-specific binding, washout is allowed to take place to leave only the marker bound to the target tissues[60, 98]. Therefore, a requirement of the *ex-vivo* imager is to operate at high sensitivity to account for low marker concentrations on account of marker non-specificity. Currently existing *in-vivo* FGS imaging devices, both wide field imagers and laparoscopic imagers are unsuitable for *ex-vivo* imaging. In the case of wide field imagers, imaging low concentrations of fluorophore with long integration times would lead to the issue of motion blur in the acquired images as the sample is held up to the imaging head. Motion blur results in unclear images making subsequent analysis difficult/impossible. Furthermore, when using wide field imagers, theatre room lighting produces higher background signal, limiting the achievable SNR. In the case of laparoscopic FGS imagers, *ex-vivo* imaging is unsuitable due to the limited *f*-number (*f*/#) of the laparoscope (the small aperture for light collection). A small aperture for light collection limits the amount of emission that can be collected from the fluorescent markers present in the tissues, again limiting the achievable SNR.

To achieve high sensitivity by maximising the achievable SNR, the *ex-vivo* imager uses a low readout noise, chilled CCD camera. This camera was chosen as it was a readily available camera that is sensitive in the near infrared regions which require probing and also due to the fact that it can be operated at longer exposure times than the cameras present in existing FGS *in-vivo* imagers. Furthermore, the *ex-vivo* imager uses a specialised wavelength tuneable illumination system to deliver sufficient power efficiently and homogeneously across the sample. Wavelength tuneable filtering is also employed to reduce unwanted wavelengths from entering the camera

and increasing the background signal. Additionally, the *ex-vivo* imager will utilise spectral unmixing approaches to maximise imaging contrast by removing confounding autofluorescence signals. The current design of the *ex-vivo* imager is included in Figure 23.

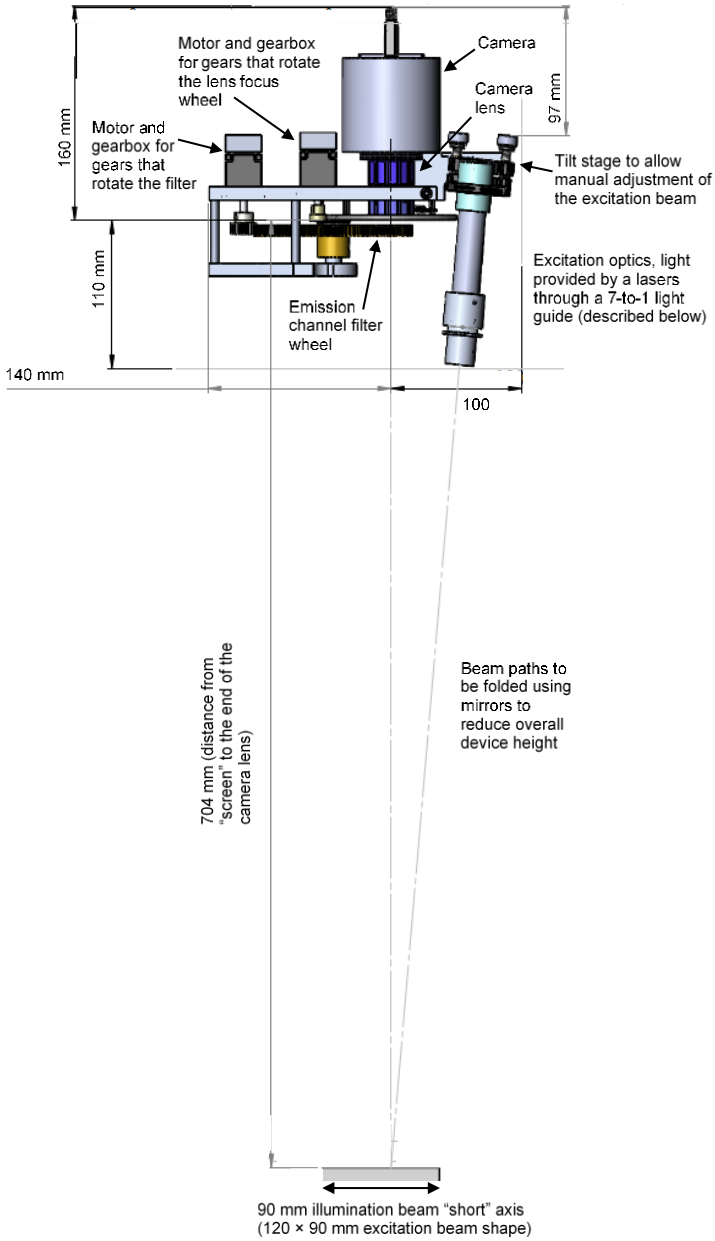


Figure 23: Main components that constitute the ex-vivo imager, shown from the side of the "short" axis of the excitation beam illumination.

Although this is not shown in Figure 23, the components will be housed inside a light proof case alongside all electronics. This eliminates theatre room light which will interfere with the imaging. Additionally, mirrors will be utilised to fold the beam paths, essentially splitting the height of the imager in half. Furthermore, in Figure 23 it can be seen that the illuminator is not mounted coaxially with the camera but is instead mounted at an angle of 5˚ relative to the detection camera. This is due to the fact that it would be too costly to implement the detection and illumination system coaxially as this would require the use of multiple large area dichromatic reflectors. Although some excitation light will be lost in this approach, the small angle used makes this negligible in practice and angled illumination is much easier to engineer. An additional slight benefit is that the likelihood of excitation light being reflected directly into the camera is reduced. The significance of the angle being 5˚ is discussed in a later section.

The purpose of this chapter is to discuss the work contributed to the development of the *ex-vivo* imager design included in Figure 23, including details of modelling and experimental results that contributed to the design.

3.2 Initial Illuminator Design

We begin with the excitation light source which was the first aspect of the *ex-vivo* imager to be designed. The illuminator provides the source of excitation light needed to produce the required fluorescence output from the sample. The two main requirements of the illuminator are: to maximise the delivered power density and to excite homogeneously across the sample area. Specifically, the light source is required to deliver intensities of the order of 1-10 mW/cm^2 to ensure that the number of photons reaching the fluorophores in the sample is appropriate, resulting in sufficient emission (since fluorophores have relatively low quantum efficiencies)[140]. A 1-10 mW/cm^2 range for the excitation intensity was chosen specifically for the reason that this has been used before in FGS(ref. 101). In theory, more power could be delivered to potentially increase fluorescence emission, thereby increasing the SNR. However, increasing power increases the potential for unwanted heating of the samples being imaged (depending on the duty cycle of the excitation light source). For this reason, the excitation power was matched with previous FGS imaging technology (although this could be altered in future designs). The imaged field was designed to be of the order of ~100 cm^2 to accommodate tissue samples from human patients whilst also accommodating mice for pre-clinical work. 120 × 90 mm^2 was deemed to be a good choice as this matches the 4:3 aspect ratio of common cameras, such as the CCD camera used in the imager (discussed later).

The first aspect of the excitation light source to be discussed is the selection of the light source itself as this was the first and most crucial step in the design of the illuminator system. The design originally started with LEDs since these have been

used in at least one commercial FGS system[101]. When considering the LED as the excitation light source, it was proposed that each LED wavelength could be mounted on a wheel, which would be rotated to select the desired wavelength. This would have been straightforward, since the electronics required to power LEDs are minimal (compared to lasers). However, as will be seen later, this approach had to be abandoned in favour of laser diodes sources.

What makes LEDs attractive as a light source, in many applications (not just this one), is the wide availability of many different packages and wavelengths at low cost. Before confirming LEDs as the right choice for the excitation light source, the optical modelling software Zemax/OpticStudio[141], was used to design the illumination system. Typically, many manufacturers provide a ready-made Zemax model of the optical components that they supply but in the case of the most suitable LED packages, no such models were available. A model of a commercially available LED package (shown in Figure 24(ref. 142)) was therefore developed in Zemax/OpticStudio from scratch.



Figure 24: LED package available from Roithner GmbH, initially chosen as the light source for the excitation system/illuminator. This LED package, part of the SMB1N Series (http://www.roithner-laser.com/led_highsingle_smd.html) was chosen for its narrow emission angle. This is compared to the other available LED packages not supplied with a lens, that exhibit much wider-angle emission profiles. Wider angle emission profiles are not desirable as they would require much more involved optics designs to maximise light collection for small area illumination.

The model based on the commercially available LED package shown in Figure 24 was designed to enable a variety of optical systems to be tested before purchasing the required optics. The development of the model proved difficult due to the fact that the material of the LED lens and the position of the LED chip in relation to the surface of the lens were not specified. However, since silicone resin is a widely used material for applications such as LED encapsulants and lenses[143], the optical properties of silicone resin were used to inform the model[144, 145]. An initial estimate for the position of the LED chip relative to the front surface of the lens was made by simply observing a single LED package, that was available to hand. An iterative approach was then used to determine the actual position of the LED chip to produce a reasonably accurate LED package model, which is shown in Figure 25.

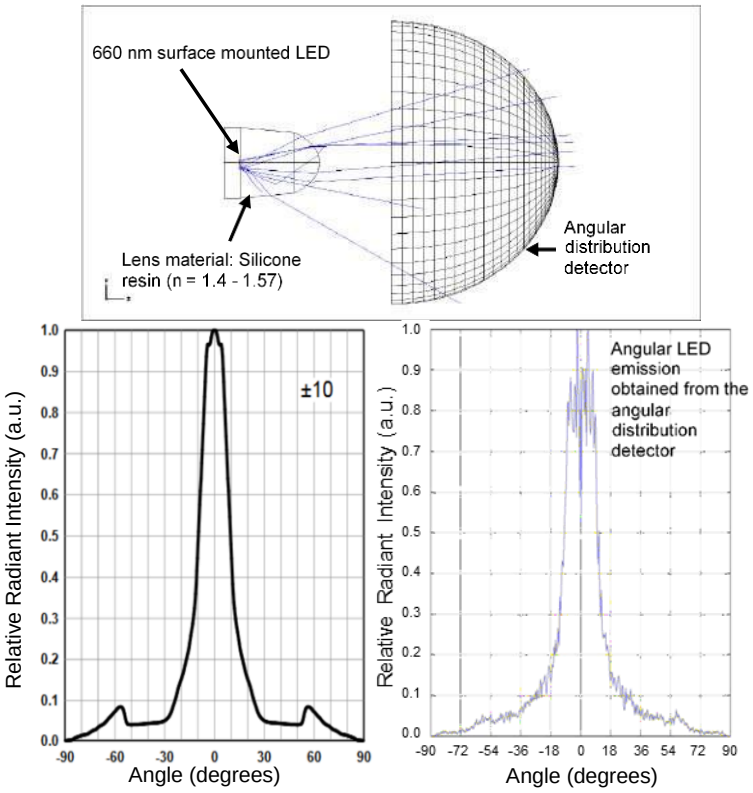


Figure 25: *Top*: LED model developed in Zemax from the manufacturer's data sheet (from Roithner Lasertechnik GmbH); *Bottom Left*: Relative radiant intensity as a function of angle for the LED as measured by the manufacturer; *Bottom Right*: Relative radiant intensity as a function of angle for the LED model as measured with an angular distribution detector in Zemax.

The model shown in Figure 25 was deemed to be reasonably accurate from a qualitative point of view as the plots line up closely when overlapped.. From a quantitative point of view, the full width half maximum (FWHM) of the manufacturers plot (located on the bottom left of Figure 25) is 20 degrees and 18 degrees for the Zemax model (located on the bottom right of Figure 25). This represents a 10% percentage difference between the Zemax model and the manufacturers plot in terms of the FWHM. Furthermore, the ratio of the peak to the side lobes is 12.5 for the manufacturers plot and 15.8 for the Zemax model. This represents a 27% percentage difference between the Zemax model and the manufacturers plot in terms of the ratio of the peaks to the side lobes. Whilst there is a discrepancy between the model and the manufacturers plot, the model was deemed to be a reasonable starting point for future simulations of the light source at this stage of the design, especially since a model was not available from the manufacturer. The reason for the differences between the plots could be the inaccuracy of the position of the chip relative to the surface of the encapsulant and/or the inaccuracy in terms of the correct value of the refractive index of the encapsulant material in the Zemax model. The measured LED radiation profile is provided by Roithner Lasertechnik GmbH for the SMB1N type LED[146].

Using this LED model, the aim was to find an arrangement of LEDs and/or optical elements (situated after the LEDs) to produce a 120×90 mm^2 emission profile at a working distance of ~600 mm, which is a reasonable distance to ensure that the imaging device is not excessively large. One of the first LED arrangements simulated

in Zemax for this project, that achieved close to the desired illumination pattern, was a 2 × 3 arrangement of LEDs as shown in Figure 26.

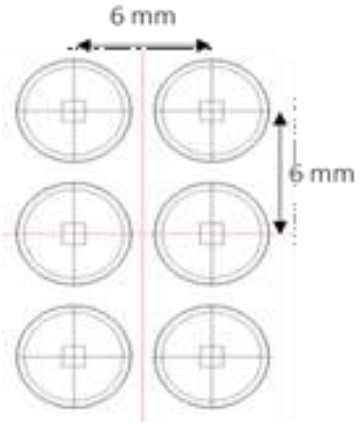


Figure 26: Rectangular arrangement of LEDs designed to achieve a rectangular emission profile. The 6 mm dimension is the minimum distance that this type of LED can be separated by when mounted.

With an arrangement of LEDs specified in the Zemax model, the next step was to place a single 40 mm diameter plano-convex lens (of focal length 160 mm) after the LED ‘array’ to collect all of the emission, as shown in Figure 27. The positions of each lens were varied in the Zemax model until the emission profile achieved an output that came close to achieving the required beam shape, as shown in Figure 28.

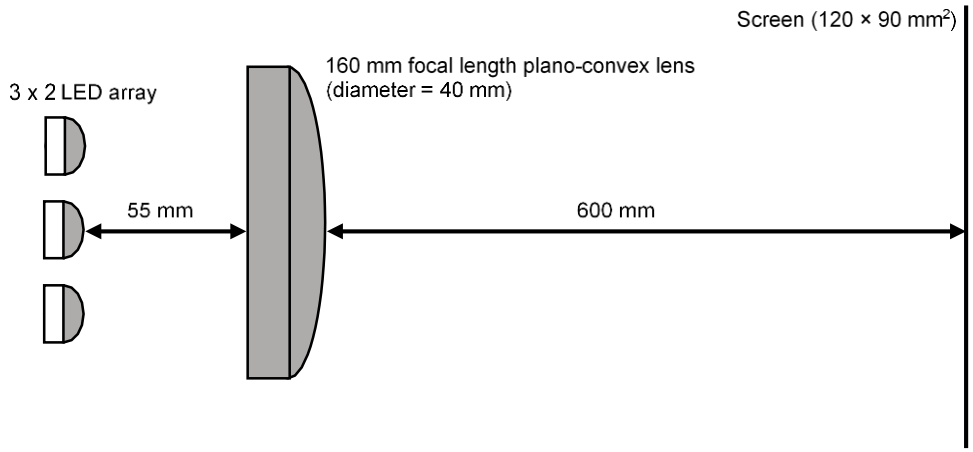


Figure 27: Zemax model consisting of a 2 × 3 array of LEDS based on the model in Figure 23 and a single common lens (of focal length 160 mm) placed 55 mm from the LED array (not to scale). The distance from the lens to the screen is 600 mm.

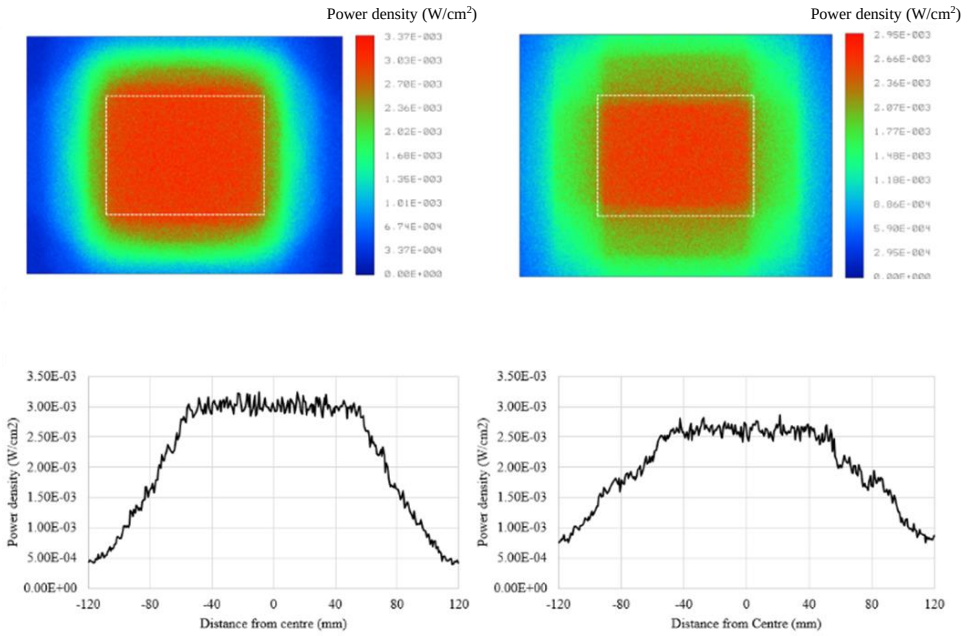


Figure 28: Results of simulations in Zemax. *Upper left*: Illumination profile produced by the 6 LED array with a 160 mm focal length lens (of diameter 40 mm) placed at a distance of 55 mm away from the LED array. *Upper right*: Illumination profile produced by the 6-LED array with an 80 mm focal length lens (of diameter 40 mm) placed at a distance of 20 mm away from the LED array. *Bottom left*: Power density at the screen as a function of the horizontal distance from the centre of screen for the profile produced in the upper left of the figure. *Bottom right*: Power density at the screen as a function of the horizontal distance from the centre of screen for the profile produced in the upper right of the figure.

Of the two lenses used in the above setup, the 160 mm focal length lens performed better in terms of the peak power density across the illuminated area. The peak is reasonably flat, although there is light lost at the edges of the 120 × 90 mm^2 area of interest.

Unfortunately, the spectral emission from LEDs is broad (>20-30 nm FWHM bandwidth) and their output must be filtered in order to allow fluorescence excitation of small Stokes shift fluorophores. It was therefore soon realised that this option is ultimately not particularly efficient due to the cost of large diameter filters required (40 mm in this instance). These filters are unduly expensive. Filters are most commonly available with clear apertures of 22 mm and correspondingly reduced diameter lenses are then required. A reduction in lens diameter demands that the distance between the LEDs and the lens is reduced, which in turn requires that the focal length be reduced. In attempt to find a solution to this issue, a lens of shorter focal length, placed at a closer distance of ~5 mm away from the LED array, to maximise light collection and reduce aberrations, was used to improve the system. However, this produced similar results to that of the 40 mm diameter lenses which is acceptable but it was felt that superior results could be achieved using a different setup.

Alongside the modelling described above, experiments were conducted at the optical bench to determine if combining LED beams was practical in reality. This was possible due to the fact that the LEDs are readily available at low cost for such experiments. This is discussed in the '*Experimental Testing*' section.

Ultimately, when taking account of all the information obtained in regard to the LEDs and upon further consultation of the radiation characteristics of the LED emission,

shown in Figure 29, it was decided that the use of LEDs as the excitation source in the *ex-vivo* imager would be abandoned.

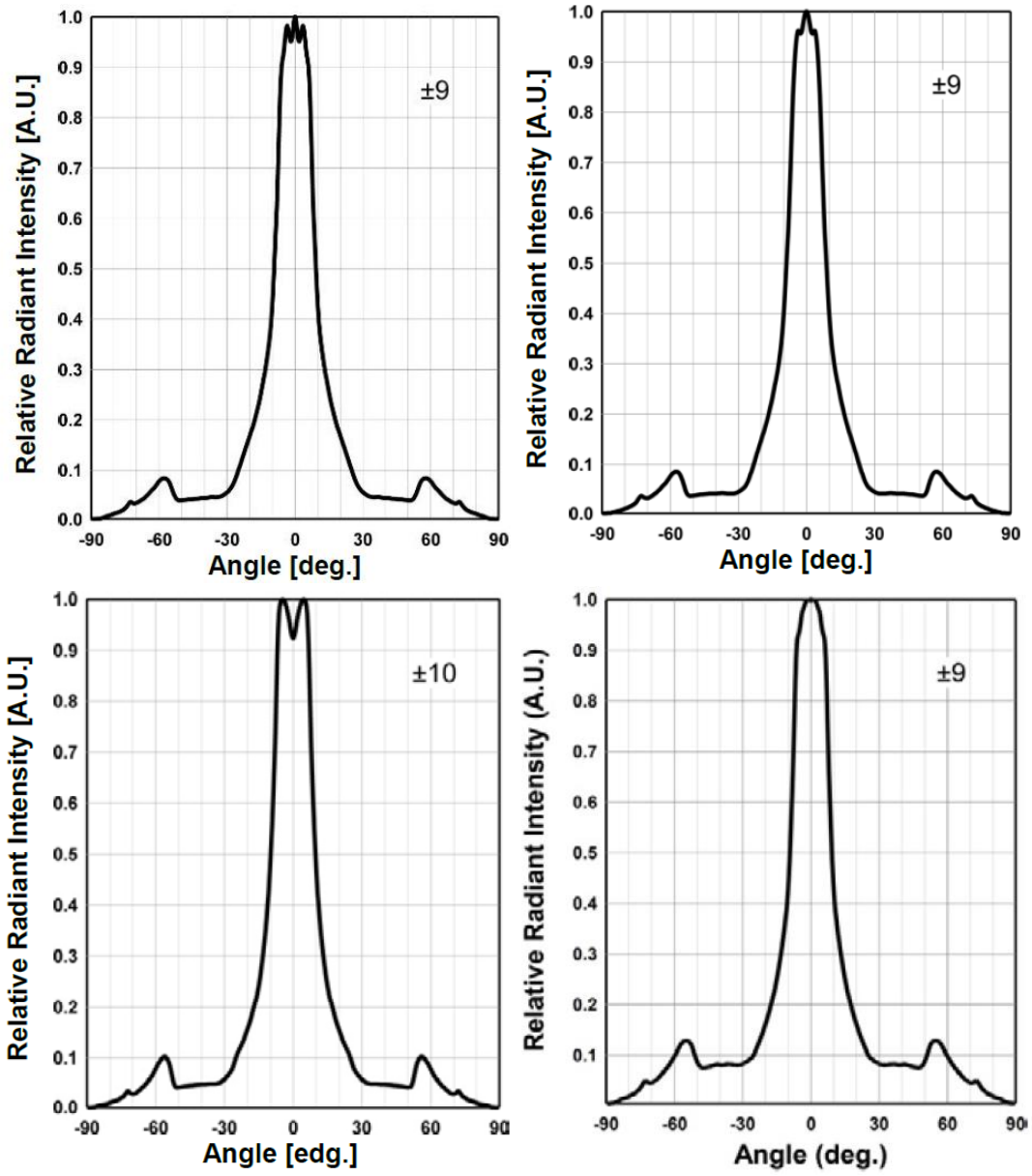


Figure 29: Radiation characteristics of several LEDs, of wavelengths: 690 nm (*top left*), 760 nm (*top right*), 810 nm (*bottom left*) and 830 nm (*bottom right*).

The relative intensity of the LED as a function of angle varies between each LED wavelength to the extent where design of a universal optical system for all wavelengths would be difficult, with each of the wavelength emitters requiring optimisation. The system would therefore be much more complicated than originally thought.

Furthermore, while such arrangements could be perhaps realised, they would require impracticably large filters.

Laser diodes were selected as the most viable replacement of LEDs. Although laser diodes are costly, they are significantly cheaper than large filters required by LEDs. Furthermore, laser diodes have the advantage of producing significantly higher power outputs over narrower bandwidths. They still require filters to remove unwanted output sidebands but it is much easier to deliver the required power density to the sample area since they behave as near-point sources (at least relative to other system dimensions).

3.3 Towards a Laser Diode Excitation Illumination System

Since the use of LEDs was abandoned it was decided that the most feasible light source to use in the illumination system would be the laser diode. As with the LEDs, multiple wavelengths would be utilised, to excite the fluorophores listed in Table 7. The laser diodes in the excitation illumination system are listed in Table 8[ref. 147].

Laser Part Number	Laser Wavelength (nm)	Optical Power (mW)	Input Power (mW)	Efficiency, η (%)	Beam Divergence (º)	
					Parallel, //	Perpendicular, ⊥
LDX-2410-645	645±3	400	2205	18	7	24
LDX-2410-690	690±3	750	2420	31	7	34
LDX-3110-750	750±5	1500	3040	49	6	26
LDX-3210-780	780±5	2000	3847.5	52	7	26
LDX-3210-808	808±5	2000	3800	52.5	7	36

Table 8: Laser diodes to be used in the *ex-vivo* imager excitation system. The data in this table is supplied by RPMC lasers Inc. and LDX Optronics Inc.

In this section, the design of the laser diode excitation illumination system will be discussed with particular emphasis on how the final design was reached by modelling the system in the optical modelling software Zemax.

All 5 laser diodes listed in Table 8 are to be mounted in a 10 mm thick laser cold plate and a 17 mm Delrin block for insulation. The system is designed with the aim of utilising 7 lasers but for now only 5 lasers have been selected. Laser temperature stabilisation and cooling is provided by a thermoelectric cooler (TEC) system. Each laser is collimated, filtered and refocused onto a 400 µm optical fibre. All of these fibre outputs are then bundled together in a 7-to-1 optical fibre combiner[148], as shown in Figure 30. The fibre bundle is shown in Figure 31.

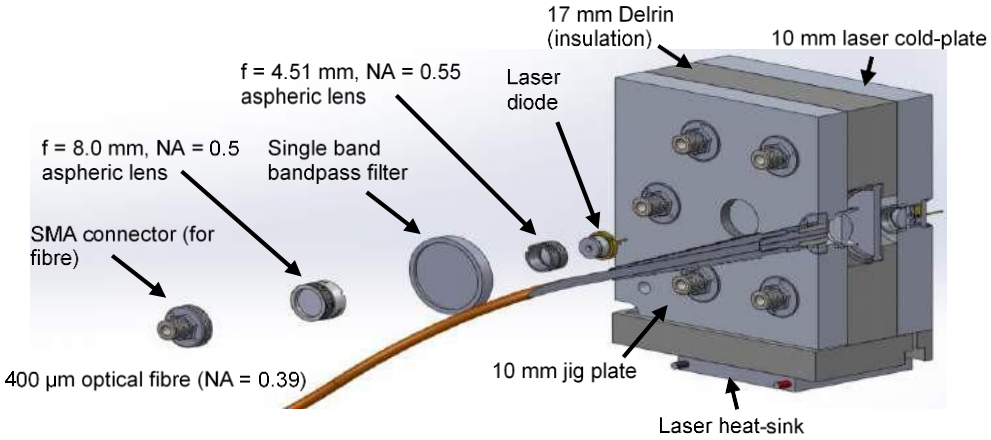


Figure 30: Exploded view of the *ex-vivo* imager light source, produced in Solid Works®. The output of each individual laser diode (LD) is brought together with the outputs of the other laser diodes in a 7-to-1 optical fibre.

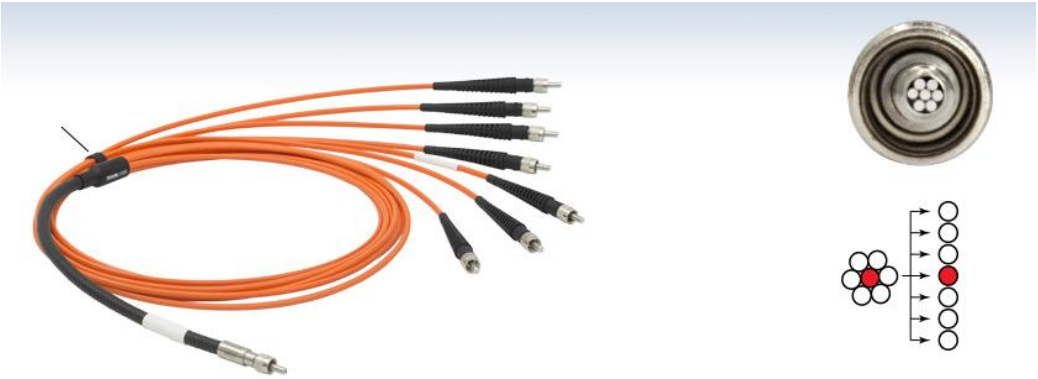


Figure 31: 400 µm 7-to-1 optical fibre from Thorlabs.

One laser at a time is energised and the output of each laser is guided to the final stage of the illuminator system. The final stage of the illuminator system uses a trapezoidal light pipe[149], as shown in Figure 32, to homogenise the output from the 7-to-1 fibre bundle by placing it close to the light pipe's 2.5 × 2.5 mm^2 input face. The chosen light pipe is 100 mm long and has a 5 × 5 mm^2 output face.

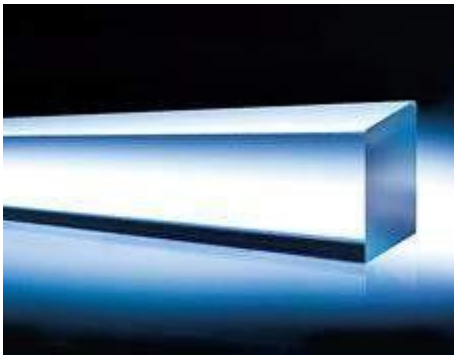


Figure 32: 2.5 × 2.5 mm^2 input face, 100 mm length, 5 × 5 mm^2 output face trapezoidal light guide.

The homogenised output is then shaped into a rectangular illumination field at the site of the sample undergoing excitation. This will be referred to as the screen from now on. The 120 × 90 mm^2 rectangular beam shape at the screen is produced using a single (30 mm focal length, 18 mm diameter) plano-convex lens[150] and a single (50 mm focal length, 22 × 20 mm^2) cylindrical lens[151]. The illuminator system is shown in Figure 33.

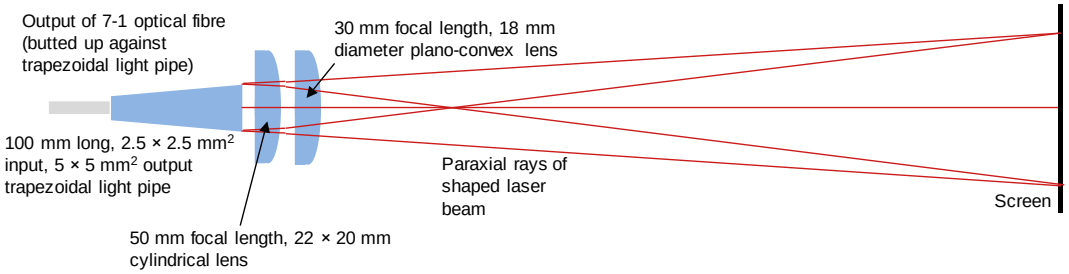


Figure 33: Optical setup of the excitation illuminator system.

What follows next are the various steps taken using Zemax to select the different optical components that comprise the excitation system and illuminator.

3.3.1 Laser Fibre Coupling

The laser diodes are to be mounted in one block and the outputs combined into a readily available 7-1 optical fibre combiner (Thorlabs® BF74LS01) as discussed previously. To couple the laser light from each wavelength into its respective input of the 7-to-1 fibre Zemax was utilised to determine the most suitable optical arrangement for this.

As with the LED, an available Zemax model of the laser diodes selected for the *ex-vivo* imager was not available. However, Zemax has an inbuilt '*Source Diode*' function built into the software which allows one to recreate the emission from a real laser diode. The main pieces of information required were the perpendicular and parallel laser dimension angles, which were provided by the manufacturer (and included in Table 8).

Before coupling to the input of the 7-to-1 optical fibre, the output of each laser requires filtering in order to remove unwanted LED-mode sidebands from the emission spectrum before being coupled to the input of the optical fibre. Multilayer filters are used here and they must be placed in an optical 'infinity' space. To collimate the laser diode output to allow for efficient filtering a single aspheric lens, of focal length 3.1 mm, was placed 1.85 mm from the laser diode[152]. An aspheric lens is used as aberrations are reduced and the collimation is superior as a result.

After the laser beam has passed through the filter, the collimated beam must be re-focussed into the optical fibre input aperture, for this a second lens is required.

Since the input aperture of the optical fibre has a numerical aperture (NA) of 0.39 the lens must focus the laser beam into a cone of no more than the corresponding acceptance angle of the fibre, i.e. ~46˚ (the half angle is ~23˚). Since the diameter of the collimated laser beam entering the lens is a known variable (2.8 mm), the approximate focal length required to achieve the ideal focusing can be estimated using the following equation:

$$f = \frac{2.8\ mm}{tan\ (22.95^{\circ})} = 6.6\ mm \quad (4)$$

Unfortunately, no commercially available lenses with a back focal length of 6.6 mm are available. However, this can be compensated for by adjusting the distance between the lens and the optical fibre to find the optimal position of the lens. Of the available lenses, the most suitable lens was found to be an aspheric lens of focal length 8 mm [ref. 153]. A schematic providing the details of the final design for the laser fibre coupling system is shown in Figure 34.

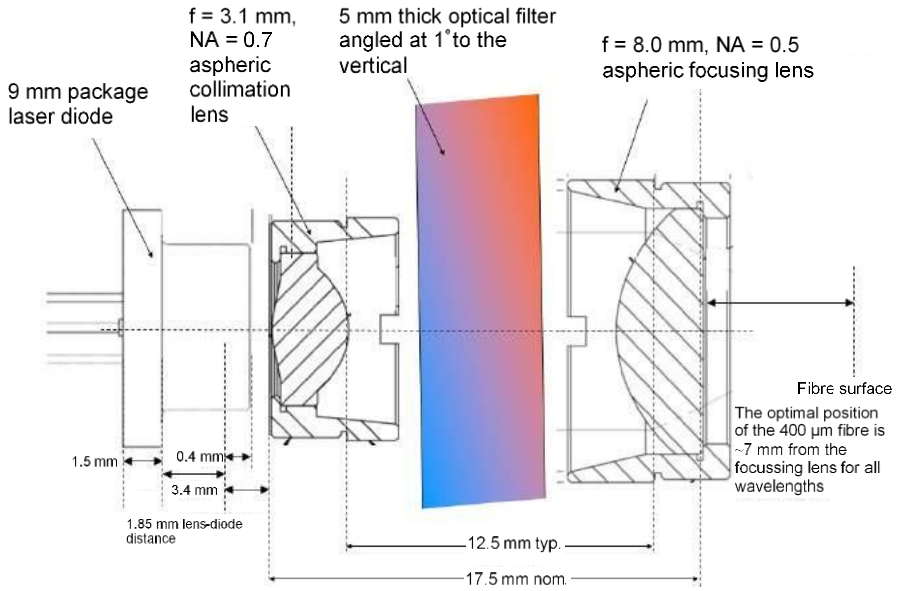


Figure 34: Laser diode-optical fibre coupling optical arrangement with lens spacings labelled. The design was developed in Zemax as with other optical designs include in this dissertation.

The optical filter situated in the middle of the two lenses is angled at 1˚ (minimum) to prevent light reflected from the front surface of the filter from coupling back into the laser diode. Laser light reflected back into the laser diode is undesirable as this can cause optical feedback that results in changing the laser output mode and potentially destroying the laser. The consequences of laser back-reflections have been reported previously in the literature[154].

3.3.2 Homogenisation and Beam Shaping

With the laser to optical fibre coupling design finalised, the optical system after the optical fibre was designed next. This part of the excitation light source forms the beam shaping illuminator, which was designed to provide a homogeneous illumination profile across an area of 120 × 90 mm^2. As before, all components were simulated in Zemax.

The main challenge when designing the illuminator, was to achieve a homogeneous, rectangular beam profile from a circular output produced from the 7-to-1 optical fibre (with an NA of 0.39 giving an emission cone half angle of 23˚). To achieve a homogeneous beam a light guide was used, specifically a trapezoidal light pipe of 2.5 × 2.5 mm^2 input face and 5 × 5 mm^2 output face (as shown previously in Figure 32).

When a particular laser wavelength is selected the trapezoidal light guide accepts laser light from one of 7 output apertures in the optical fibre bundle. The central fibre is aligned with the centre axis of the light guide with the other output fibres arranged in a hexagonal pattern around the central fibre.

When the trapezoidal light guide was simulated in Zemax, the central fibre output and two outputs at the edge of the bundle were simulated to determine if homogenisation is affected by the position of the fibre output, as shown in Figure 35. Although the light guide used in the final design of the illuminator is 100 mm in length, two light guides of different lengths (50 mm and 100 mm) were simulated to determine if the extent of homogenisation was affected significantly by the length of the light guide. Homogenisation is important in the light guide as this determines the homogeneity of the beam at the illuminated object.

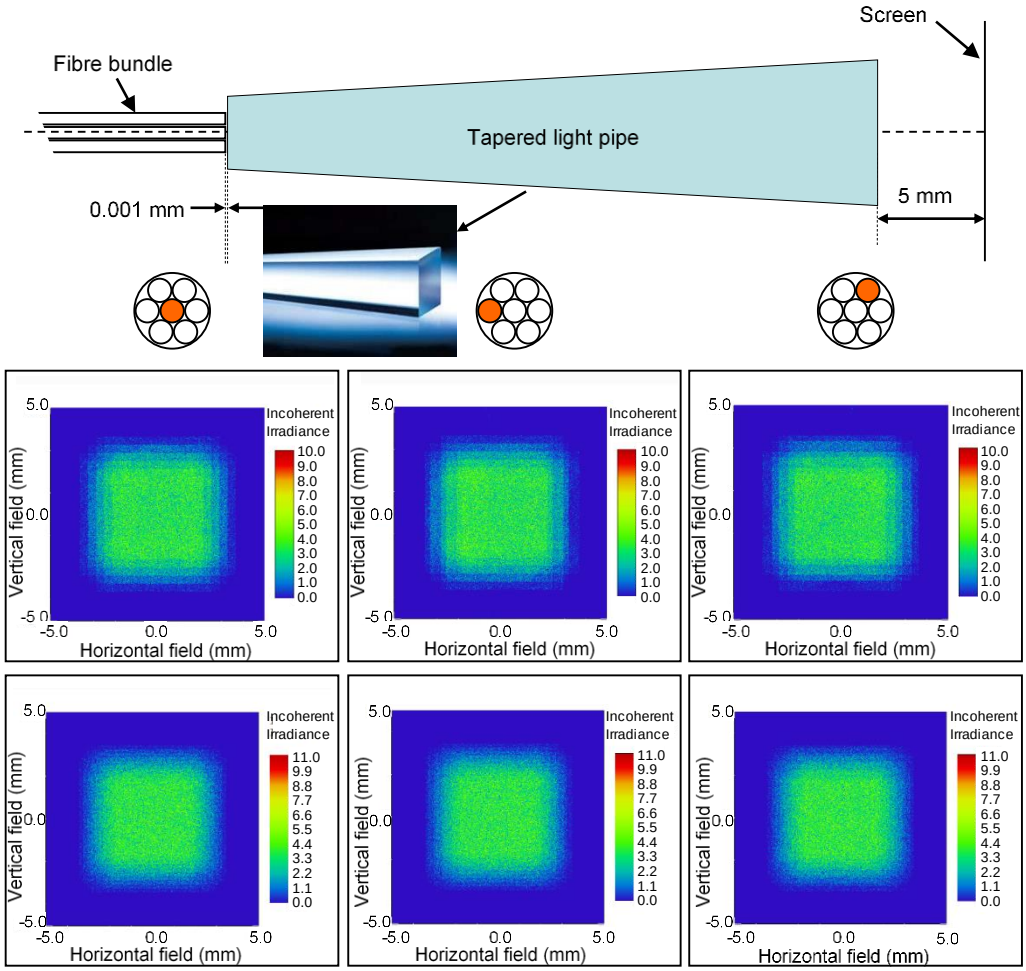


Figure 35: Results of Zemax simulations to qualitatively assess the homogenisation introduced by two different tapered light pipes. U*pper panels/plots*: Homogenisation induced by a 50 mm length tapered light guide. *Lower panels/plots*: Homogenisation induced by a100 mm length tapered light guide. Both tapered light guides possess 2.5 × 2.5 mm^2 input and 5 × 5 mm^2 output faces. T*op patterns*: The particular fibre output switched on for the simulation. The laser wavelength used in these particular simulations was 750 nm. Other wavelengths result in similar output patterns. The light pipe geometry is depicted at the top.

It can be seen that the beam homogenisation remains unaffected when the outer fibres are ‘switched on’ since the beam profiles at the output of the tapered light pipe are indistinguishable. However, altering the length of the light pipe from 50 mm to 100 mm does produce a slightly more homogeneous beam output. This was determined qualitatively by observing the plots by eye, with the plots generated by the 100 mm length tapered light guide appearing slightly more smooth at the edges with the 50 mm tapered light guide producing a beam with a slightly ‘stepped’ edge. Therefore the 100 mm light pipe was chosen in favour of the 50 mm light pipe.

Once the homogenisation of the beam had been verified in Zemax, the next challenge in the illuminator design was forming the rectangular beam at the screen.

To select the most appropriate optics to shape the output of the trapezoidal light pipe the étendue (see Appendix B) was considered at the input of the light pipe, to determine the emission angle at the output to best select the appropriate optics. In short, the étendue is a quantity that describes the spread of the beam as it traverses the light guide and it must be conserved. The étendue is proportional to the area and the solid angle of the beam entering the light guide, which is how this calculation was made. The input solid angle of the beam is ∼0.5 steradians and as previously defined the input area of the light pipe is 2.5 × 2.5 mm^2. This light enters the light pipe and emerges with a solid angle that is reduced by 4×, since the output face of the light pipe has an area of 5 × 5 mm^2 (4× more). The solid angle is reduced by a factor of 4 since to ensure conservation of the étendue. This equates to an output solid angle of ∼0.13 steradians, giving an output beam cone half angle of 11.5˚.

The task is now to reimage the 5 × 5 mm^2 output face of the trapezoidal light pipe with an emission half angle of <12˚ onto the screen to form a rectangular shape. Essentially this involves taking a square beam and transforming it into a rectangle, stretching the beam in one direction more than in the other direction. It was estimated that the best way to do this is with a plano-convex lens to stretch in both directions and then introduce additional stretching with a cylindrical lens.

To select the appropriate plano-convex lens, the problem was treated as a simple lens problem involving imaging a 5 mm tall ‘object’ onto a screen to form a 90 mm tall (and 90 mm wide image).

Using the thin lens equation, which relates the focal length (f), the object distance (u) and the image distance (v) as follows:

$$\frac{1}{f} = \frac{1}{u} + \frac{1}{v} \tag{5}$$

The ideal focal length lens can be determined if the distance from the lens to the screen is set to some value. This distance is largely determined from the limits on size of the imager itself, the specifications of commercially available lenses and the required angle of the beam for excitation rejection in the filters (as discussed later). Based on these considerations the value of v was initially set to be 590 mm. The distance from the object (i.e. the tapered light pipe output face) to the lens can be set using the following equation (used to determine the desired magnification, M):

$$M = \frac{i}{o} = \frac{v}{u} \tag{6}$$

Where i is the image height and o is the object height. The required M is equal to 90/5 = 18. This sets the initial value of the u to be equal to 590/18 = 32.8 mm.

Substituting this value of u into the thin lens equation, a focal length of 31.1 mm is obtained. The setup of this problem is summarised in Figure 36.

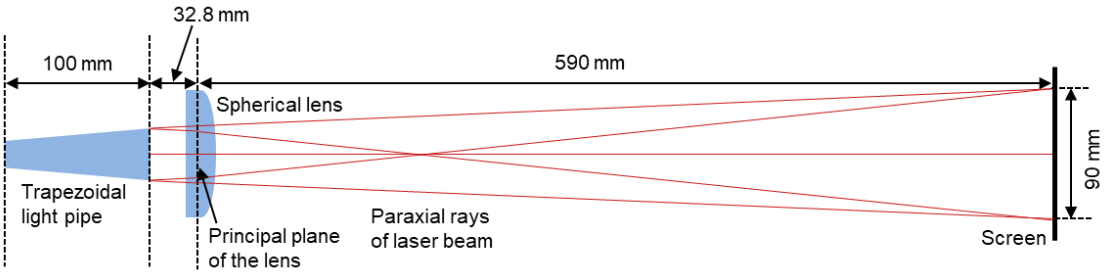


Figure 36: Zemax model setup to stretch 5 × 5 mm^2 beam into a 90 × 90 mm^2 illumination beam at the screen.

Unfortunately, lenses of 31.1 mm focal length are not readily available so instead, a lens of focal length of 30 mm (and diameter 18 mm) was selected to provide square illumination. It should be noted that by introducing a simple spherical lens, it was expected that some pincushion distortion would be present. This could be improved upon by using an achromatic lens but this increases cost somewhat for marginal gains in beam shape. The 30 mm spherical lens was added to the model shown previously in Figure 36 and the resulting beam profile was simulated in Zemax. The lens-to-screen working distance was varied in the model to test if any discernible difference in illumination homogeneity was observed. Both the 50 mm and 100 mm light pipes were simulated with the spherical lens to test if the 50 mm light pipe produced any difference in beam homogeneity at the screen, despite loss in homogeneity at the output of the light pipe. The illumination profiles can be seen in Figure 37, additionally the diagonal beam profiles are included in Figure 38.

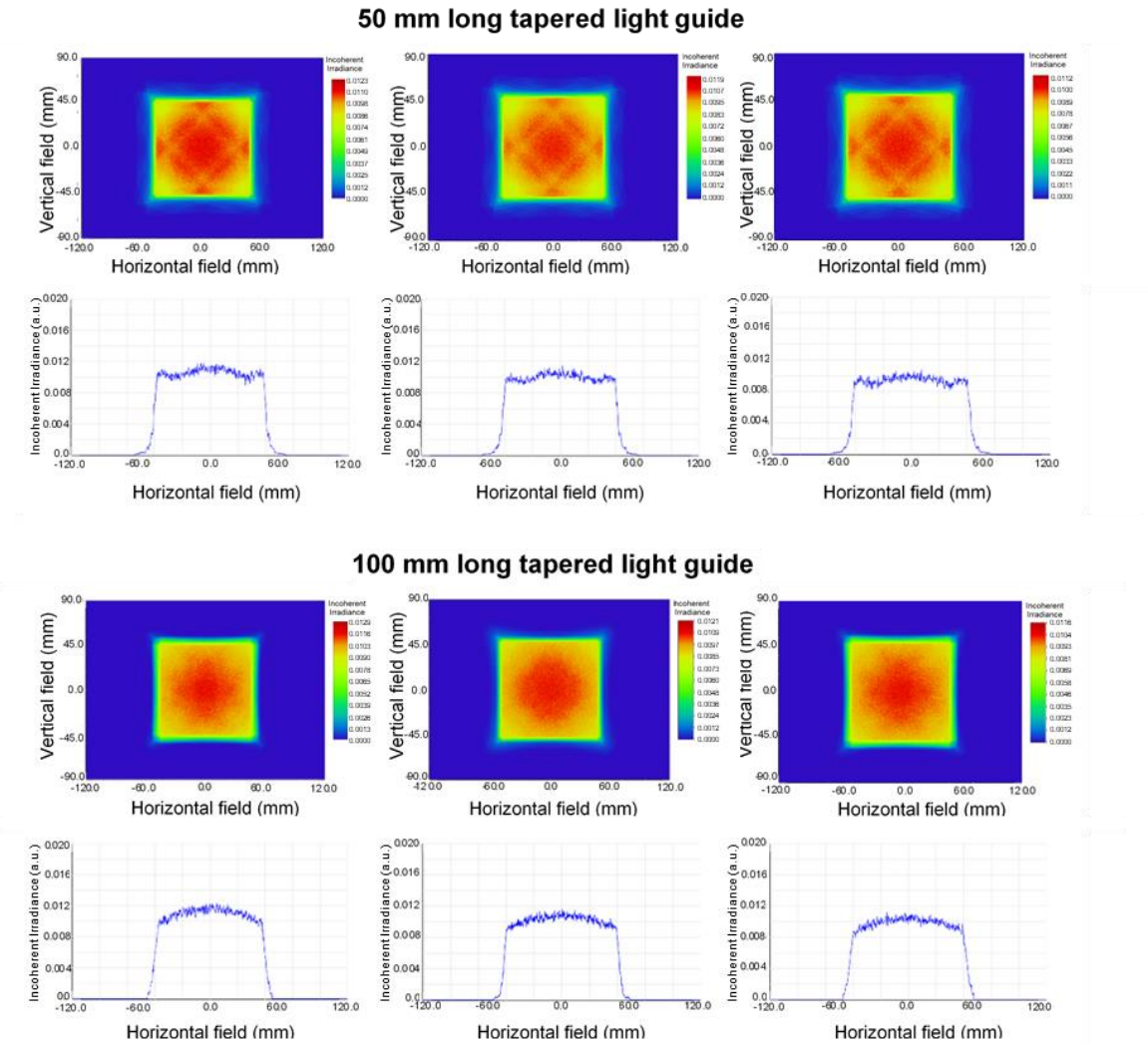


Figure 37: Performance of system with a single 30 mm focal length lens, resulting in a 90 × 90 mm^2 illumination field. Left: working distance = 575 mm; middle: working distance = 590 mm; right: working distance = 605 mm. Bottom plots show field flatness at the various working distances.

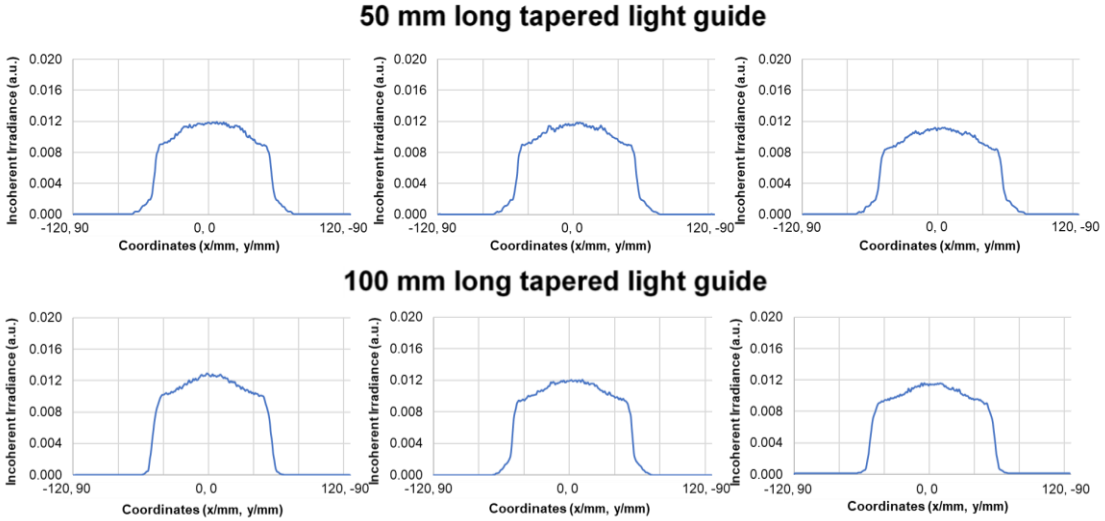


Figure 38: Diagonal beam profiles to accompany the horizontal beam profiles included at the bottom of Figure 37. By including the diagonal and horizontal beam profiles it provides a more complete picture of beam flatness.

As was the case before, the 100 mm light pipe generates the most homogeneous beam profile. Although it should be noted that the profiles on the bottom of Figure 37 are not completely homogeneous. This is more apparent in the beam profiles shown in Figure 38, with a 'hump' in intensity demonstrated in the beam profiles. Furthermore, in the RGB images in Figure 37 some pincushion distortion is present at the edges of the beam. However, this is minimal and can therefore be considered acceptable for this system.

To achieve the desired rectangular beam pattern, additional stretching is required in the horizontal direction. Specifically, to achieve the desired beam illumination pattern, a combined magnification (spherical lens + cylindrical lens) of 120/5 = 24 is required in the horizontal field. Due to the addition of the cylindrical lens the problem becomes a combined two-lens problem. For combined lenses, the formula for the total combined focal length of the system is as follows:

$$f_c = \frac{u_c v_c}{u_c + v_c} \tag{7}$$

For the combined lens it must be that $u_c + v_c = 622.8$ mm whilst ensuring that $v_c = 24u_c$ (where u_c is the object distance to the combined lens system and v_c is the image distance from the combined lens system). This is summarised in Figure 39.

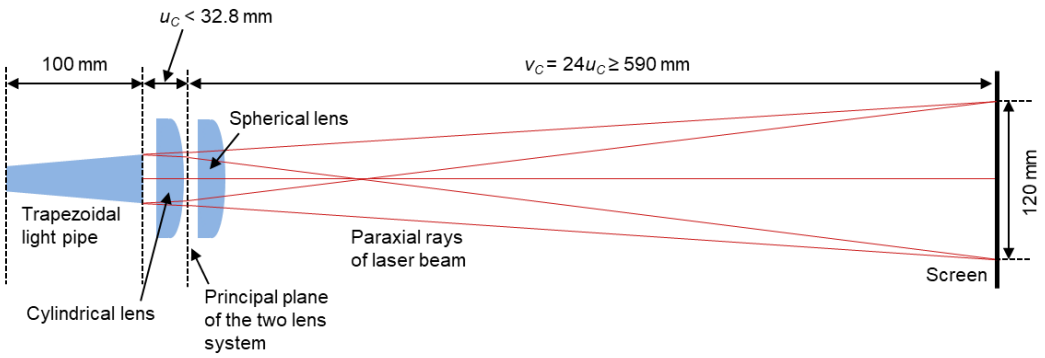


Figure 39: Zemax model setup to stretch 5 × 5 mm^2 beam into a 120 × 90 mm^2 illumination beam at the screen by adding a cylindrical lens. Both lens are treated as a combined lens of focal length f_C.

Based on what is known about the system, equation (7) becomes:

$$f_c = \frac{24{u_c}^2}{622.8} \tag{8}$$

Since u_c must be <32.8 mm a suitable value for u_c, such as 22.8 mm (10 mm less than the maximum allowed) can be chosen and the focal length of the combined lens calculated. Substituting the value of u_c into the above equation yields a value of f_c of 20.03 mm. Choosing a cylindrical lens of available focal length, for example a reasonable choice is 30 mm (matching the focal length of the spherical lens), the following formula[155] can then be used to determine the optimal distance (d) between them:

$$f_c = \frac{f_1 f_2}{(f_1 + f_2 - d)} \tag{9}$$

Where f_c is the combined focal length of the two lenses, f_1 is the focal length of the first lens, f_2 is the focal length of the second lens and d is the distance between them. Substituting in the relevant values and rearranging we find that the ideal distance is 15 mm for a combined focal length of 20.03 mm. This is of course the ideal approach but in reality, other factors come into play when dealing with real lenses, i.e. thick lenses and additional optical aberrations introduced by them. When lenses of long focal length are used, the issue is less apparent but, in this case, the lenses have relatively short focal lengths. To solve this issue, a 50 mm cylindrical lens, separated by 5 mm from a 30 mm spherical lens was implemented to reduce the total thickness of glass the beam was traversing. Zemax was used to simulate the beam achieved with this two-lens system as shown in Figure 40. As before, diagonal beam profiles are provided in Figure 41.

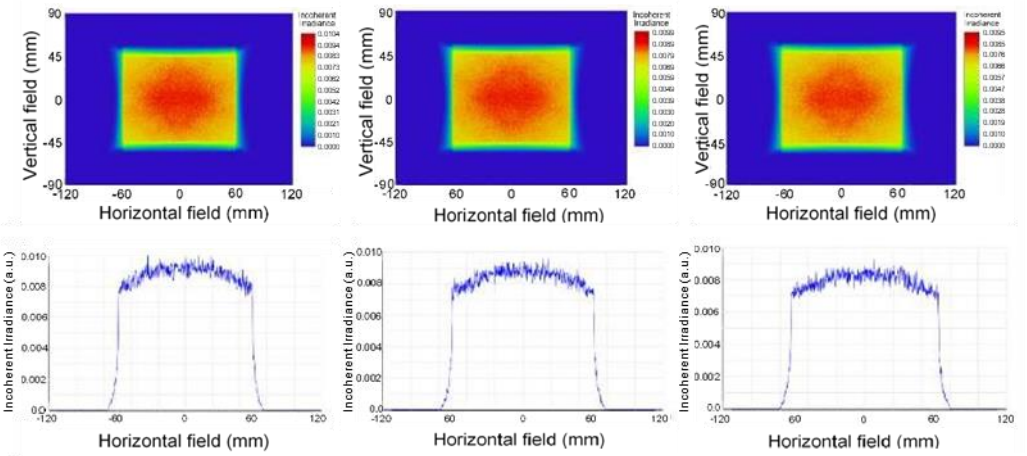


Figure 40: Performance of system with spherical and cylindrical lenses, resulting in a 120 × 90 mm^2 illumination field. *Left*: working distance = 575 mm; *middle*: working distance = 590 mm; *right*: working distance = 605 mm. *Bottom*: plots show field flatness at the various working distances.

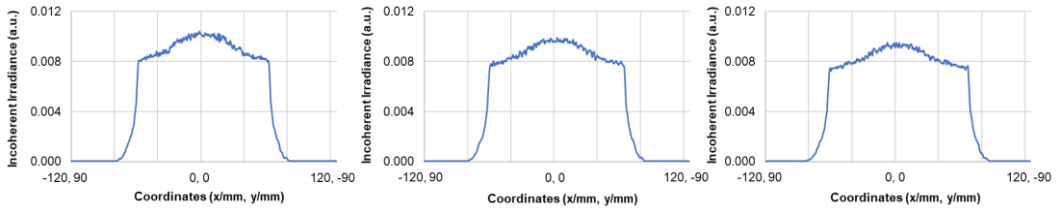


Figure 41: Diagonal beam profiles to accompany the horizontal beam profiles included at the bottom of Figure 40.

As can be seen in Figure 40, the cylindrical lens provides the required stretching of the beam to produce the desired 120 × 90 mm^2. It should be noted that, although every effort was made to achieve a completely flat illumination beam using the optics simulated in Zemax, this was not entirely possible, as shown at the bottom of Figure 40 and in the diagonal beam profiles included in Figure 41. There are methods to ensure beam flatness but these methods result in lost light and therefore reduced excitation intensity. Such methods include using higher magnification optics and then introducing an aperture stop to remove the light at the edges to ensure only the central flat portion of the beam was used. Other methods include using an apodising filter or a diffuser.

On the other hand, a 20% light loss at the corners is readily compensated for by image-processing after the camera output and will only reduce the edge signal to noise ratio by a few percent. The design arrived at was thus considered to be satisfactory. For reference, the complete design of the excitation illuminator system is shown Figure 42.

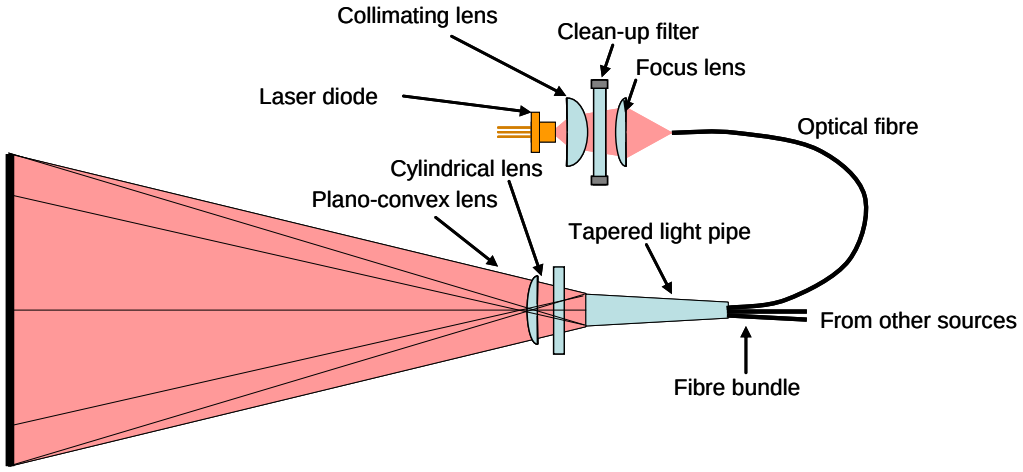


Figure 42: Outline of the design of the excitation illuminator system.

3.3.3 Additional Details

An additional bonus of the excitation illumination design is that it is inherently flexible and can be modified to achieve different aspect ratios. One such aspect ratio that the illuminator can be adapted for is 16:9, for example. To achieve a 16:9 aspect ratio, the focal length of the cylindrical lens was reduced from 50 mm to 12.5 mm and adjusting the distances between components slightly but other otherwise keeping everything else the same as demonstrated in Figure 43. The beam shape is shown in Figure 44, the horizontal and diagonal beam profiles are included in Figure 45.

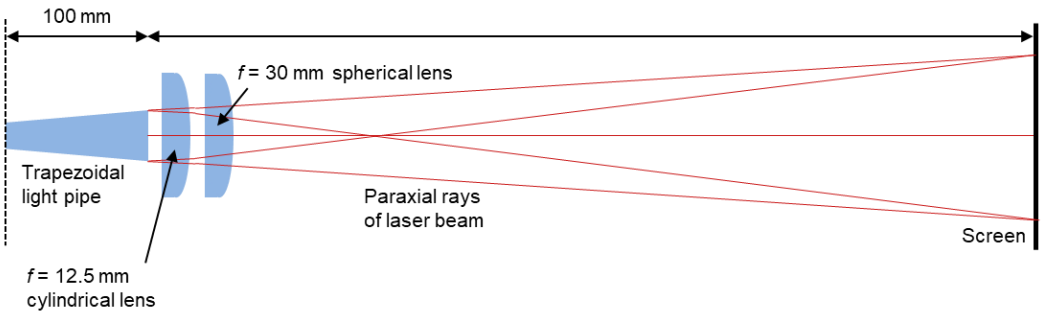


Figure 43: Optical layout designed to achieve a 16:9 aspect ratio.

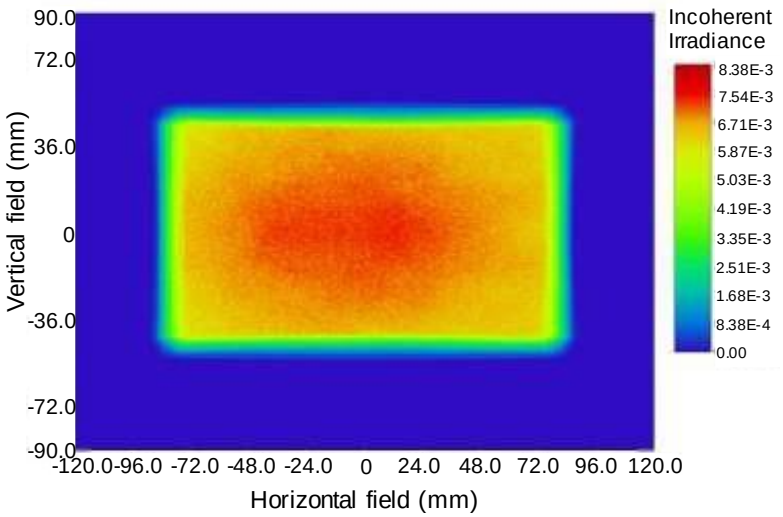


Figure 44: Beam shape at the screen.

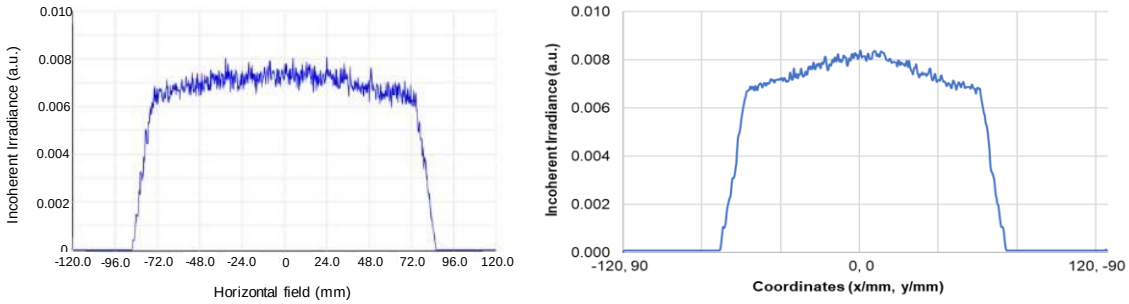


Figure 45: *Left*: Beam profile in the horizontal direction. *Right*: Beam profile in the diagonal direction.

It is noted that in both the 4:3 and 16:9 aspect ratio designs the field is not perfectly uniform and the excitation drops by <20% at the edges. Such differences in the centre and edge excitation can be readily corrected in software by imaging an object exhibiting uniform fluorescence (e.g. acrylic or other plastic sheets doped with fluorophores[156, 157]). Moreover, such corrections would also take care of any potential vignetting in the imaging system. Of course, the signal-to-noise ratio would decrease somewhat at the edges.

3.4 CCD Camera and NIR Lens

Fluorophore emissions are detected with a CCD camera, specifically the Trius SX-825 (Starlight Xpress Ltd.)[158] typically used for imaging in amateur astronomy. This camera was chosen for this application because it is a low readout noise camera that is sensitive in the near infrared. Low readout noise ensures that the achievable SNR can be maximised. Furthermore, the camera can be operated at exposure times that are longer than that utilised in real time *in-vivo* FGS imaging. Specifically, to maximise light collection and increase the achievable SNR, the camera will be operated at exposure times on the order of 500 ms to 1 s.

The camera is equipped with a VIS-NIR lens of fixed focal length 50 mm from Edmund Optics[159]. To allow adjustment of the focus of the lens during imaging, the lens focus ring is fitted with a gearing system, turned by a geared motor.

The lens is equipped with an *f*-number wheel which allows adjustment of the aperture size (*f*-number) of the lens. The *f*-number describes the ratio of the lens focal length (50 mm) to the diameter of the aperture, which determines the light collecting capability of the lens and sets the depth of field (the distance over which objects appear to be in focus). It is important to optimise both the light collection and depth of field achievable with the lens. It is important to optimise the light collection to maximise the signal to noise ratio achievable. Furthermore, optimisation of the depth of field ensures that the type of samples that are going to be imaged by the *ex-vivo* imager are completely in focus.

Since the manufacturer of the lens (Edmund Optics) provides a Zemax model, optimisation of the *f*/# could be easily carried out using the sequential mode of

Zemax[§§§]. By using this model of the lens, the ideal *f*/# for this application was found to be *f*/4, since this offers maximal light collection for a desirable depth of field of ~1 cm, which matches the range of sizes of samples requiring imaging.

Additionally, as discussed in the next section, concerning the selection of filters in the fluorescence emission channel, the *f*-number determines the maximum ray angle that can pass through the aperture of the lens. In the case of *f*/4, the maximum angle that can pass through the aperture at the specified working distance of ~704 mm, is ~5° which is important as it matches the maximum acceptance angle of the filters discussed in the next section.

[§§§] The sequential mode of Zemax is one of two modes that can be used in Zemax, the two modes being sequential and non-sequential mode. Sequential mode is more restrictive in how an optical system can be defined, involving individual ray tracing from a point source, rather than Monte Carlo ray tracing in non-sequential mode (which is used everywhere else in this dissertation).

3.5 Filtering

As with any FGS imaging device, filtering is a crucial aspect of the design. Filters are included in both the excitation system and the emission channel. In the excitation system, the purpose of the filters is to remove unwanted sideband emission. These 'clean-up' filters were selected using the specifications and tolerances of the laser emission provided by the laser manufacturer[160].

In the emission channel, the purpose of the filters is to block excitation light that may have been reflected from the surface of the imaged sample. Reflected excitation light would confound the incoming emission signal from the fluorophores present in the sample. To select the most appropriate filter for blocking the excitation signal in the emission channel the laser specifications (Table 8) and manufacturer defined tolerances were used.

The 'clean-up' filter transmission profile[161] and the corresponding emission channel filter transmission profile[162] for each laser are demonstrated in Figure 46.

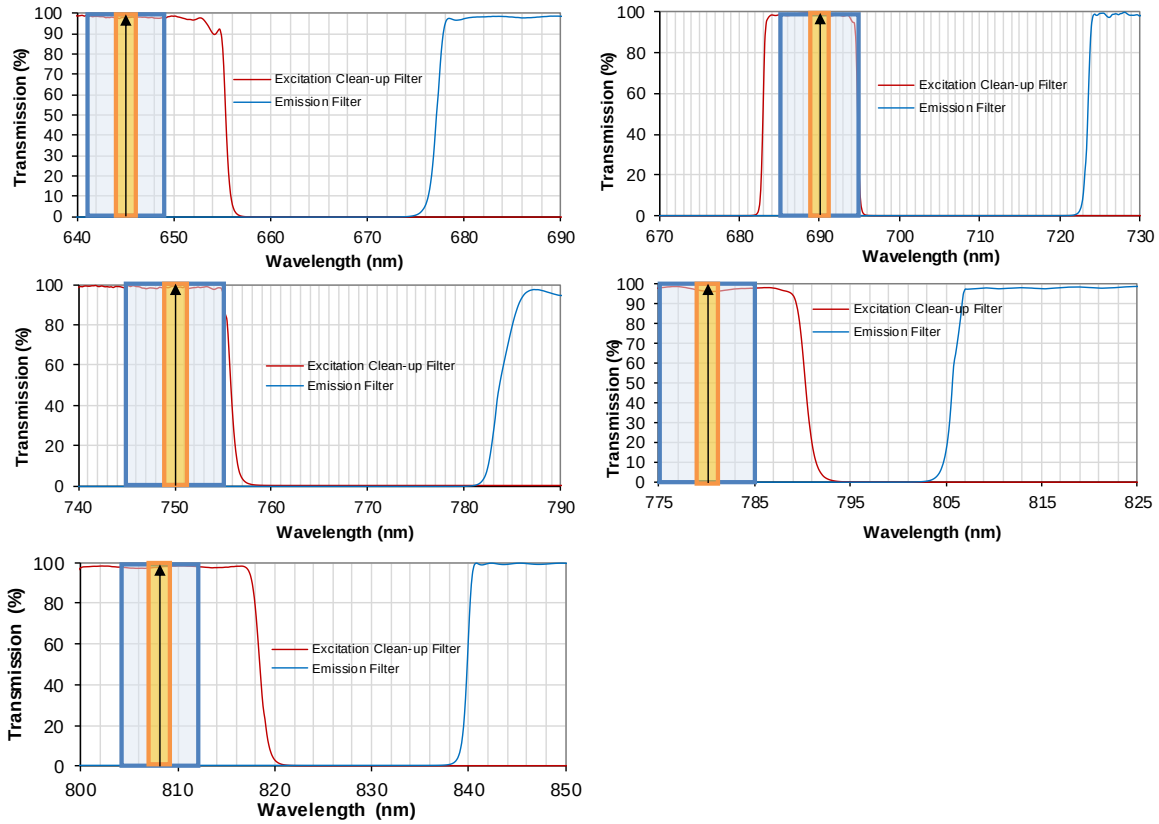


Figure 46: Data for the graphs are provided by Semrock (filters), RPMC Lasers Inc. and LDX Optronics Inc. (lasers). *Top Left*: 645 nm laser filtering; *Top Right*: 690 nm laser filtering; *Middle Left*: 750 nm laser filtering; *Middle Right*: 780 nm laser filtering; *Bottom Left*: 808 nm laser filtering. Indicated on each graph are the nominal laser emission wavelengths (black arrow), the laser bandwidths (orange box) and the laser tolerances (blue box).

Whilst the spectral data in Figure 46 demonstrate that the transmission is reduced massively in the regions where the filters act, this is not the whole story. To give a more complete picture of how well each filter performs, the optical density must be considered, this is demonstrated in the plots of Figure 47.

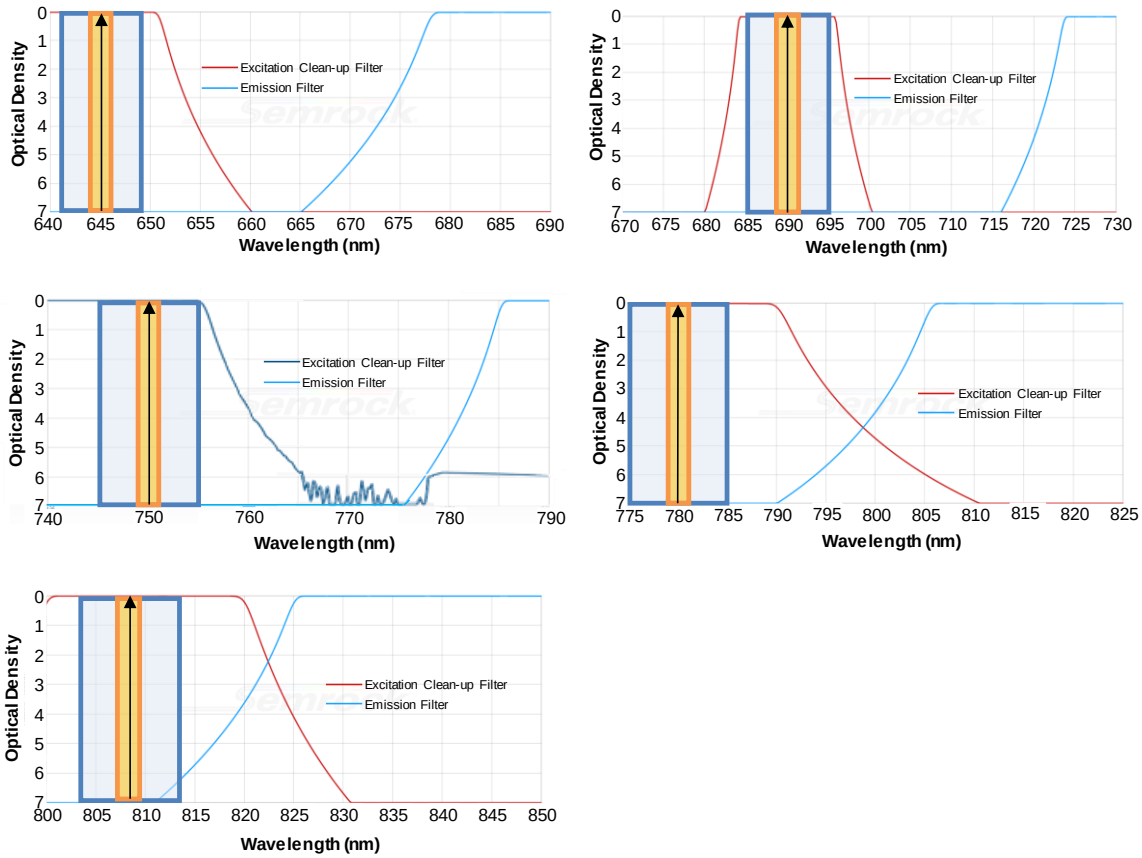


Figure 47: Data for the graphs are provided by Semrock (filters), RPMC Lasers Inc. and LDX Optronics Inc. (lasers). *Top Left*: 645 nm laser filtering in OD space; *Top Right*: 690 nm laser filtering; *Middle Left*: 750 nm laser filtering in OD space; *Middle Right*: 780 nm laser filtering in OD space; *Bottom Left*: 808 nm laser filtering in OD space. Indicated on each graph are the nominal laser emission wavelengths (black arrow), the laser bandwidths (orange box) and the laser tolerances (blue box).

From Figure 47 it can be seen that in some cases the optical density does not drop off as rapidly as the transmission suggesting that some leakage of light may occur in either channel. This is unfortunately unavoidable when using these filters. However, in the case of the emission filters, for example, the OD is at a value of 7 in the region of the laser emission (excitation light) meaning any excitation light incident on the filter is reduced to $1/10^7$ of its original intensity. This is a sizeable reduction and can be considered acceptable for this application.

In the excitation channel, the *ex-vivo* imager allows for selection of different excitation wavelengths during imaging. As with the focusing of the camera lens, switching of the emission filters is performed with a motorised filter wheel, as shown in Figure 48.

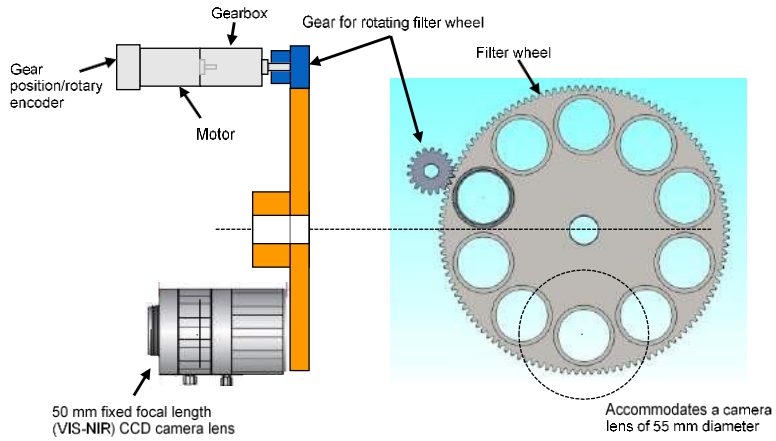


Figure 48: Filter wheel used to select different filters for the emission channel of the *ex-vivo* imager to accommodate for switching of excitation wavelength during imaging.

When the user requires the correct emission filter, when selecting one of the various excitation lasers, the stepper motor moves the filter wheel to align the centre of the desired filter with the centre of the camera lens. To enable alignment of the filters with the camera lens, the system driven by the stepper motor includes a magnet and Hall effect sensor, which senses the position and flags the zero position. The correct stepper motor setting is obtained by calibrating the number of steps the stepper motor must go through from the zero position to the first filter. This process is performed empirically at the calibration stage. One important aspect of the emission filters in the *ex-vivo* imager is the specified maximum cone half angle (CHA) of light incident on the surface of the filters. If the maximum cone half angle is exceeded by incident light, then the filters do not operate at their maximum effectiveness[163].

For all of the Semrock filters included in the design of the *ex-vivo* imager the smallest maximum cone half angle is quoted as being 5°. This means that the filter does not operate at its optimum for light incident on the filter at angles greater than 5°. To demonstrate the effect of increasing the incident light cone half angle (CHA) above 5°, transmission profiles of the filters are shown in Figure 49.

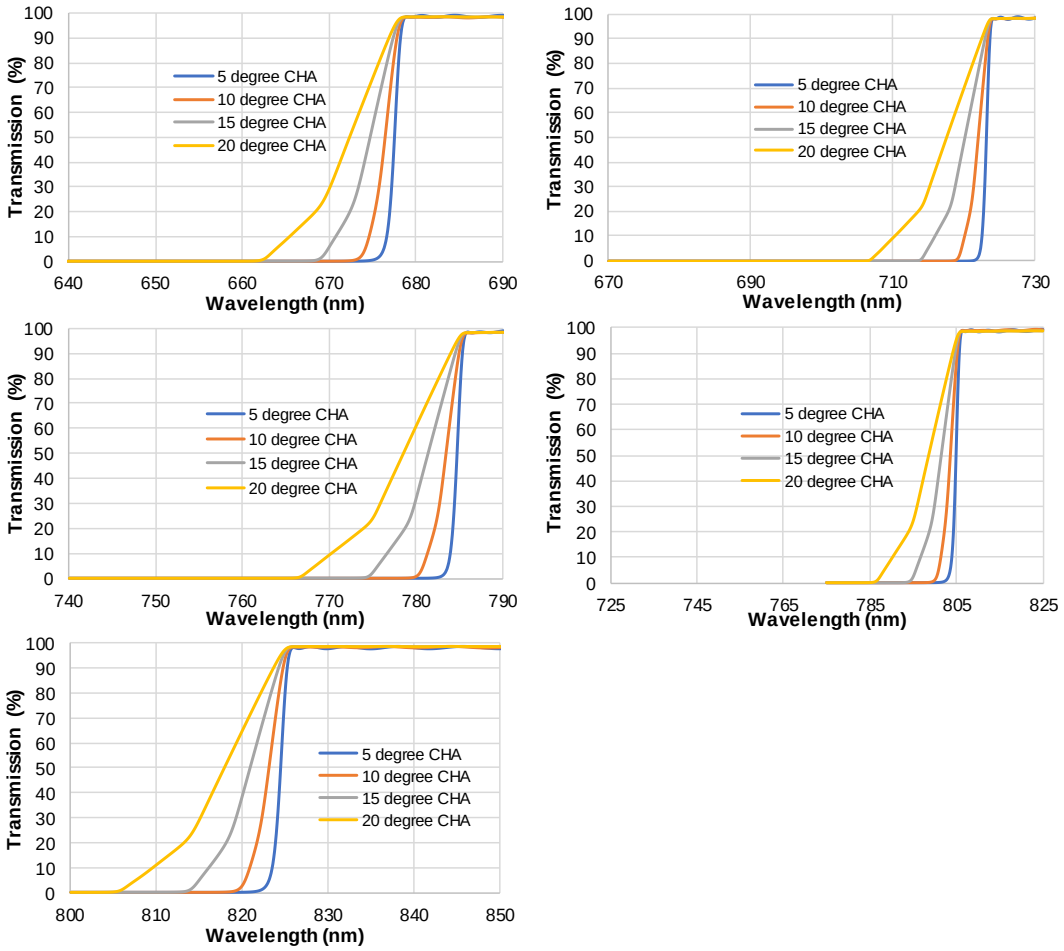


Figure 49: Data for the graphs are provided by Semrock. *Top Left*: 645 nm laser emission filtering; *Top Right*: 690 nm laser emission filtering; *Middle Left*: 750 nm laser emission filtering; *Middle Right*: 780 nm laser emission filtering; *Bottom Left*: 808 nm laser emission filtering.

As demonstrated in Figure 49, if light is incident on the filter at greater cone half angles then the hard edge of the transmission curve becomes distorted. This results in increased leakage of undesirable wavelengths through the filter into the emission channel. To keep this at a minimum, the maximum angle of acceptance into the emission channel is designed to be no more than 5°.

3.6 Spectral Unmixing

An interesting aspect of the *ex-vivo* imager design is the incorporation of spectral unmixing in the image processing chain. One of the difficulties in achieving high contrast in FGS imaging is the potential presence of autofluorescence that confounds the detected signal. Spectral unmixing can be used to remove the effects of autofluorescence signals thereby increasing the contrast. A spectral unmixing algorithm essentially sorts the spectral data present in each pixel into the individual spectral components.

Spectral unmixing relies on predetermined knowledge of the spectra likely to be present in an image. In the case of the *ex-vivo* imager the spectra likely to be present in an image are the signal of the fluorophore and the autofluorescence background. These data can be obtained by spectrometers during surgical procedures.

Unmixing models are either linear or non-linear, depending on the data set that requires unmixing. Linear unmixing algorithms are best used for unmixing spectral data that are acquired from a single specular reflection from a well-defined distribution of materials. Non-linear unmixing algorithms on the other hand are best used for unmixing spectral data that are acquired from multiple diffuse reflections from randomly distributed materials in a homogeneous medium[164].

Different unmixing algorithms exist but for the *ex-vivo* imager, the algorithm that was selected as the most appropriate for the data to be acquired is a non-negative least squares unmixing algorithm[165, 166].

Such methods have been previously been used by members of the Advanced Technology Development Group in the Department of Oncology at Oxford in which this work is conducted. Others have also used such methods for their applications[167].

The non-negative least squares unmixing algorithm treats the spectrum of the incoming image data as follows:

$$\varphi_{spectrum} = c_1\varphi_1 + c_2\varphi_2 + \cdots + c_N\varphi_N \quad (10)$$

Where $\varphi_{spectrum}$ denotes the spectrum detected by the imager; c_N denotes a constant which can take a value between 0 and 1 (but it may not be negative) and which describes the proportion of the total spectrum that the N^{th} spectral component (denoted by φ) corresponds to. Using spectral data as a reference for φ_1, φ_2, etc. values of the constants c are determined to reproduce the measured spectrum, φ. The algorithm eliminates non-negative values that cannot be physically true. As mentioned previously, the reference spectral data for the fluorophore and the autofluorescence spectrum are to be acquired during surgical procedures using spectrometers. As of the time of writing this dissertation the spectral unmixing algorithms have not been implemented in software. However, it felt necessary to provide a summary of what the spectral unmixing process will entail.

3.7 Experimental Testing Results

This section includes details of experimental data generated (and the methods used to generate it) when testing certain aspects of the *ex-vivo* imager.

3.7.1 Camera Performance Testing

The Starlight Xpress camera CCD incorporated in the *ex-vivo* imager is designed to operate in low light conditions and is therefore expected to perform reasonably well. As an experiment to measure the performance of the camera in terms of its conversion gain, photon transfer measurements were conducted on the camera. The conversion gain gives an indication of the number of photons each digital unit corresponds to in an image obtained by the camera (a digital unit corresponding to the intensity of a pixel in digital form). The method of photon transfer is a standard method for characterising noise and CCD camera performance in astronomy[168, 169].

The photon transfer technique described here is based on the method described in Janesick, 2007. The first step of the method involves illuminating the exposed CCD chip of the camera directly with a homogeneous light source (to ensure even illumination). This light source is then varied in brightness and images are acquired at each brightness using an appropriate camera exposure in order to utilise the entire dynamic range of the camera. These images are then used to determine the mean and variance of the signal which is used to determine the conversion gain.

Janesick, 2007 states that for an array of pixels, evenly illuminated by a homogeneous light source, the total *r.m.s.* (root mean square) noise (σ_{total}, in digital units) can be expressed as follows:

$$\sigma_{total}(r.m.s.) = \{\sigma_{read}(r.m.s.)^2 + \sigma_{shot}(r.m.s.)^2 + \sigma_{FPN}(r.m.s.)^2\}^{1/2} \qquad (11)$$

Where σ_{read} is the read noise of the camera, σ_{shot} is the photon shot noise and σ_{FPN} is fixed pattern noise. As quoted in Janesick, 2007 equation (11) can be expressed as follows:

$$\sigma_{total}(r.m.s.) = \left\{\sigma_{read}(r.m.s.)^2 + \frac{S}{K_{ADC}} + [P_N S]^2\right\}^{1/2} \quad (12)$$

Where S is the signal of the camera in digital units, K_{ADC} is the conversion gain of the camera and P_N is what is known as the fixed pattern noise quality factor (which is a constant which scales with the fixed pattern noise[170, ****] as a function of the input signal S).

Since fixed pattern noise can be neglected (since the camera is a CCD), equation (12) becomes:

$$\sigma_{read+shot}(r.m.s.)^2 = \frac{S}{K_{ADC}} + \sigma_{read}(r.m.s.)^2 \quad (13)$$

Where $\sigma_{read+shot}$ is the total *r.m.s.* noise present in the signal. Equation (13) is expressed in this way to take the form of a linear $y = mx + c$ expression with the conversion gain being represented as the inverse of the gradient, m, of the line (which is the measurement obtained from photon transfer).

$\sigma_{read+shot}(r.m.s.)$ is determined by calculating the variance of the signal in images captured by the camera and σ_{read} is the intercept of the straight line.

The experimental setup demonstrated in Figure 50 was established to capture the images used to calculate the conversion gain. A 690 nm LED powered by a variable current source provided the light source. The FGS calibrator emitter module (described

**** Fixed pattern noise (FPN) is noise which becomes noticeable during longer exposures, whereby the intensity measured by a particular pixel is different from an adjacent pixel, even for even illumination and constant intensity.

in Chapter 2) is an alternative for the light source but at the time of carrying out this particular experiment the FGS calibrator emitter module was not operational. A diffuser was introduced in front of the exposed CCD chip to produce even illumination of the CCD chip.

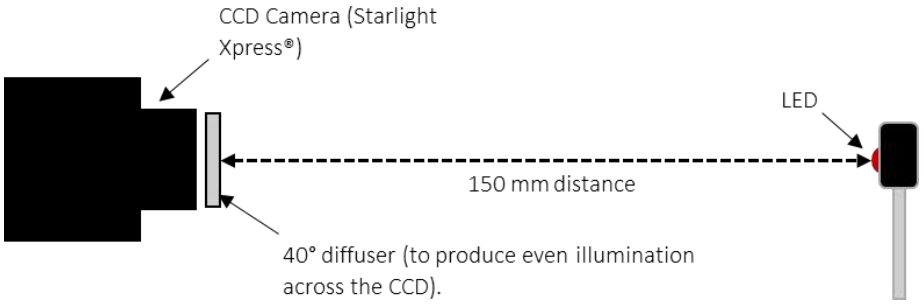


Figure 50: Experimental setup to measure the conversion gain of the camera. A 690 nm LED was used as the light source, a variable current supply enabled a range of outputs from the LED. A diffuser located in front of the CCD chip ensures that even illumination of the CCD chip can be achieved.

A series of images were acquired with the camera exposure set to 2 ms. Every image was analysed in ImageJ. The mean signal and variance was then measured across a region of interest, of area 30000 pixels^2 for each image. To determine the conversion gain of the camera the variance was plotted against the mean signal and is shown in Figure 51 where the gradient of the plot was measured. The conversion gain was then calculated as the reciprocal of the gradient.

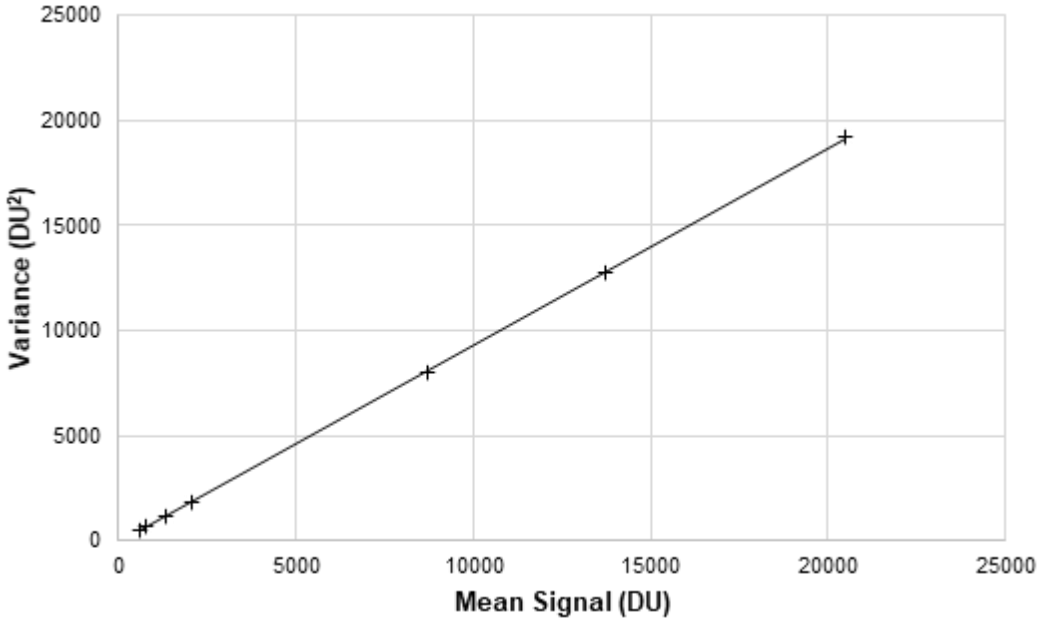


Figure 51: Variance as a function of the mean signal for an exposure of 2 ms calculated in ImageJ from images acquired with the Starlight Xpress CCD camera.

The gradient of the line in Figure 51 yields a conversion gain for the Starlight Xpress camera of 1/0.94 = 1.1 e^-/DU (DU is digital unit here). This value can then be converted into photons/DU by dividing by the nominal camera quantum efficiency, quoted by the manufacturer to be 55 % (or 0.55). Therefore, the conversion gain of the camera is 1.1/0.55 = 2 photons/DU which is reasonable for a chilled camera. The conversion gain could be better but this camera is a relatively low-cost CCD camera and is therefore unlikely to have optimal electronics in the read-out system.

3.7.2 LED Array Experiments

This experiment was conducted to determine if the LED array could be achieved in reality, since the results from modelling the system in Zemax achieved less than satisfactory results. The experiment was conducted before the LEDs were abandoned in favour of the laser diode due to their radiation profiles.

A combination of two linear translation stages were used to move a single LED in the *x* (side to side) and *y* (up and down) directions in order to experimentally simulate the LED array described previously in Figure 26. The Starlight Xpress CCD camera was then used to take multiple images which were then combined to form a composite image to demonstrate the composite beam that would be achieved with 6 LEDs. The camera was positioned approximately 900 mm from a screen. The setup is shown diagrammatically in Figure 52. The composite images can be seen in Figure 53.

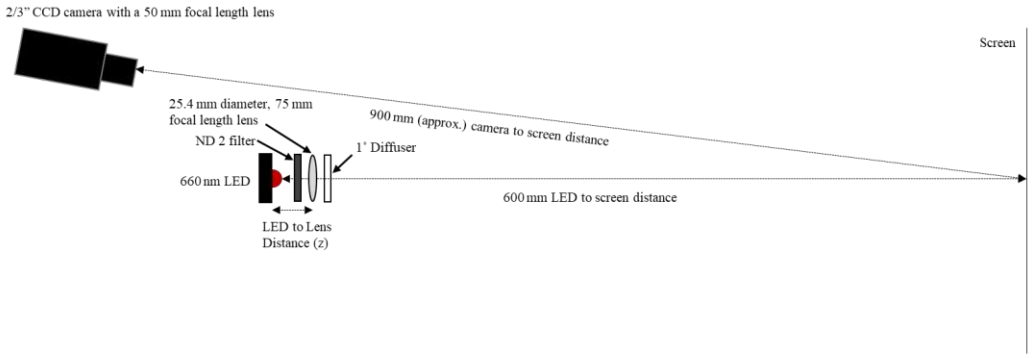


Figure 52: Experimental setup for LED experiments. The LED could be adjusted in the *x* (side to side) and *y* (up and down) directions. The screen was a paper sheet and was imaged by the camera. The camera is placed at a distance of 900 mm from the screen and positioned at a slight angle to the LED-screen optical axis to prevent the LED mount from appearing in the field of view. A 1° diffuser was introduced to the setup to scatter the LED output, as it was discovered that the LED chip bonding wires were being brought into focus at the screen, causing unwanted shadows adding to uneven illumination profiles. A neutral density filter (OD = 2, nominal) was also added to reduce the intensity of the LED beam to avoid camera saturation.

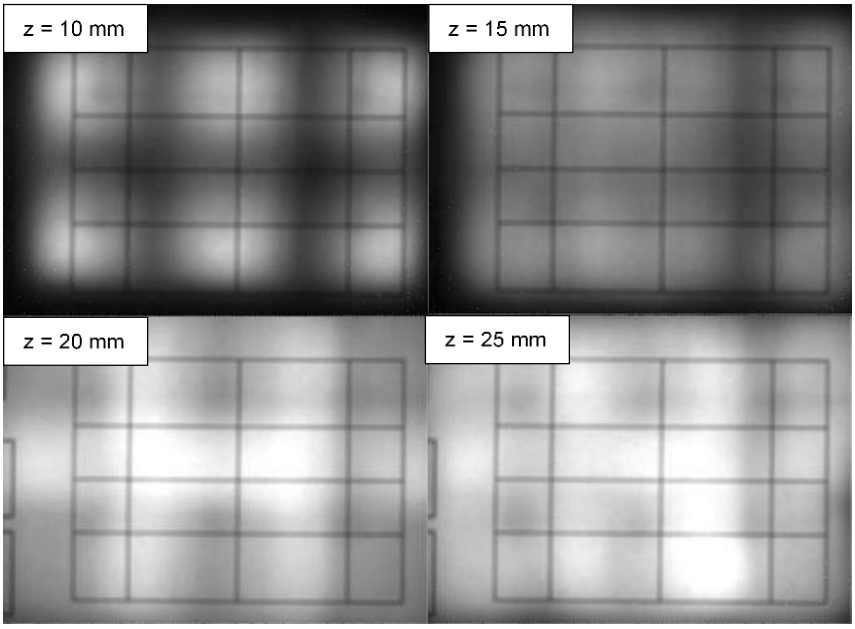


Figure 53: Composite images produced in the image processing software ImageJ demonstrating how LED outputs combine to produce a beam profile at the screen.

The distance between the LED and the lens was varied to maximise light collection but as can be seen in Figure 53, as the distance between the LED and the lens is varied, the illumination beam profile goes from underfilled to being overfilled. This was not observed in the Zemax modelling. When z = 10 mm, dark lines appear in the illumination pattern on the screen indicating that the desired beam profile is underfilled. In order to remedy this issue, the distance was increased up to 25 mm but now the beam profile had bright regions within it, indicating overfilling of the illumination beam profile. Such inhomogeneous illumination profiles are unacceptable. As previously described the use of LEDs was abandoned as the light source for the excitation delivery system for the *ex-vivo* imager, due to the radiation profiles included in Figure 29.

3.7.3 Illuminator Testing

This experiment was a simple test of the illuminator following completion of the design and construction of the system. The purpose of the experiment was to confirm that the illuminator functions as described in the model. The lasers incorporated in the final imager were not used in this test since the power supply and software for controlling the lasers was not available at the time. Instead the light source used was a simple 1 mm visible laser pointer. The laser pointer was mounted to an optical bench and aimed into one of the input channels of the 7-to-1 light fibre which was connected to the illuminator system. The illuminator system was mounted horizontally on the optical bench with a screen located approximately 600 mm away. The position of the lenses in the illuminator were adjusted until they matched that of the model described previously and the beam pattern at the screen was captured using a camera situated at approximately 600 mm away from the screen. The beam pattern is shown in Figure 54.

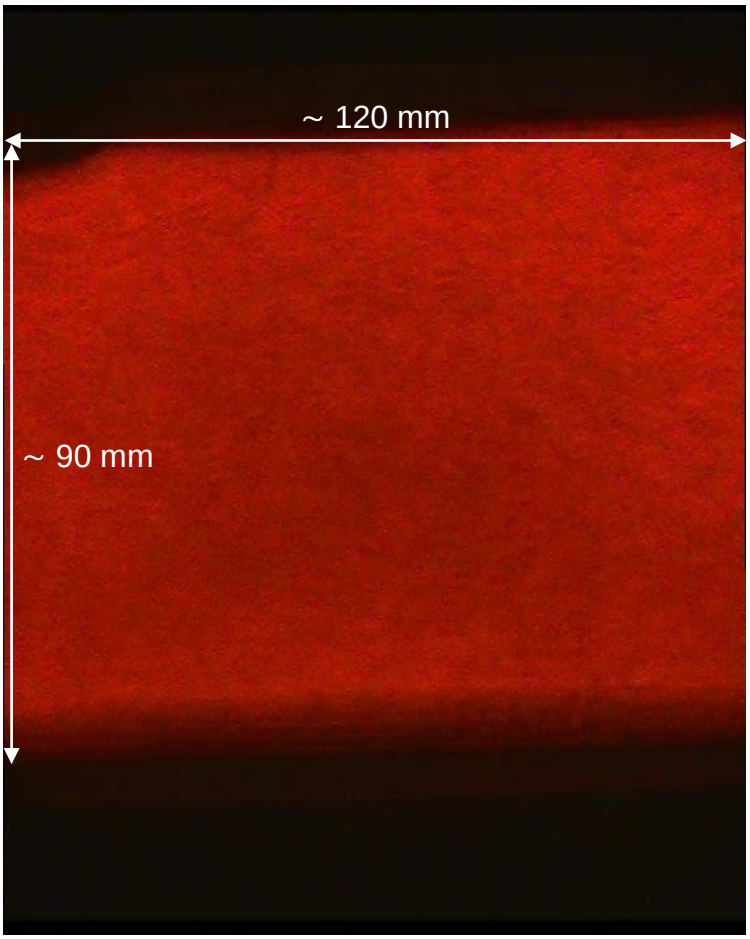


Figure 54: Beam pattern achieved for a working distance of 600 mm. *Note*: the dark patch in the top left hand corner is due to the trapezoidal light pipe becoming chipped during testing, the replacement part is to be tested with the rest of the device. The test here was conducted merely as proof of principle.

The size of the beam was measured by tracing the outline of the beam using a marker and measuring with a rule. As the model predicted, the beam illumination profile was 120×90 mm^2 in size.

3.8 Chapter 3 Summary

Presented in this chapter is the design of a novel *ex-vivo* imager to be used in tandem with other FGS imaging devices in surgery. This *ex-vivo* imager is designed to allow analysis of the surgical margins of resected tissue samples during the normal workflow of a surgical procedure. Based on the imaging results achieved with the *ex-vivo* imager, the surgeon can decide on whether further surgery is needed, i.e. if the margins are positive or close or whether the surgical resection has been successful and further surgery is not needed, i.e. if the surgical margins are negative. Therefore, this imager has the potential to directly impact the overall outcome of the surgical procedure.

Due to the fact that the *ex-vivo* imager is required to detect small concentrations of fluorophore, the device is designed to operate at high sensitivities. This is to be achieved by operating the device at longer exposure times, made possible by the fact that the imager is not required to image in real time. Furthermore, the imager will incorporate optics that allow for optimised light collection. Specifically, the low readout noise camera used in the *ex-vivo* imager is equipped with a VIS-NIR lens that can be operated at the optimum *f*-number to maximise light collection and the depth of field, in this case the camera lens will be operated at *f*/4 which results in a depth of field of ~1 cm. Besides the imager optics and camera, a novel aspect of this device is the planned incorporation of a non-negative least squares unmixing algorithm in the image processing chain. The purpose of this is to remove unwanted autofluorescence signals that reduce contrast.

In this chapter, the overall design of the imager has been outlined. Significant work has been contributed towards the development of a specialised excitation light source. The excitation light source is designed to homogeneously excite samples over a specified area using laser diodes, each wavelength selected for the set of particular fluorophores to be used in conjunction with the first iteration of the *ex-vivo* imager.

The initial design of the *ex-vivo* imager incorporated LEDs, which were modelled extensively (in the lens and optical modelling software Zemax) and used experimentally, to ascertain whether or not a homogeneous beam profile could be achieved with such a light source. Ultimately, LEDs were abandoned in favour of laser diodes due to the realisation that the desired homogeneity and beam shape required could not be achieved but also because the LED beam profiles differed between wavelengths, making a universal excitation light source difficult to realise. Following this realisation, laser diodes were decided upon as a suitable light source and a corresponding optical system was modelled in Zemax and consequently developed, this time successfully achieving the desired homogeneity and beam profile. The optical system relies on simple optical components, i.e. a trapezoidal light pipe, a single spherical lens and a single cylindrical lens to achieve a rectangular 4:3 aspect ratio beam profile with the desired homogeneity. The homogeneity could be improved further still but this would come at the cost of lost light which is undesirable for this system. The excitation light source system is flexible as it can be incorporated in other applications that use a different aspect ratio, all that is required is the swapping of the spherical and cylindrical lens for lenses of different focal lengths.

Following success with the modelling of the design of the excitation light source optical system, the components were experimentally tested at the optical bench as a quick demonstration to prove that the device functions as modelled.

Aside from the excitation system, the camera and emission channel/detection system, including the filtering system has been described. Filtering is crucial in FGS since excitation light reflecting back into the emission channel produces confounding signals. The filters selected for the *ex-vivo* imager have been matched with the excitation lasers to ensure filtering out of any laser light entering the emission channel. Since the filters are sensitive to incident angle, the *ex-vivo* imager system has been designed with this in mind, with the working distance of the camera lens (which is the aperture stop of the system), from the screen (sample area) selected to ensure that angles that may result in excess leakage of excitation light through the filter were eliminated.

Finally, to check the performance of the CCD camera in the *ex-vivo* imager, photon transfer was used to measure the conversion gain of the camera, which yielded a result which is reasonable for a camera of this type.

In the future, work conducted on the *ex-vivo* imager will involve testing of the device as a whole and measuring performance using fluorescence markers in the lab and using the FGS calibrator. The ultimate aim will be to take the device into preclinical trial settings and eventually to the operating theatre and to determine the practical aspects of the device and performance during surgical procedures. As a final note it should be said that, since the *ex-vivo* imager has been designed for use in surgical theatre, it is unlikely that resected tissue samples will be uniform across all resections in practice. Even though the *ex-vivo* imager is designed to accommodate samples within a range of thicknesses (up to 1 cm), there is likely to be uncertainty in the thickness with some

samples perhaps being thicker than the *ex-vivo* imager is designed for. If this is the case then parts of the sample being imaged may be out of focus which is undesirable for imaging. This could be accounted for by removing more tissue from the sample until it comes within the acceptable range of thicknesses. However, the device described here has been developed thus far to simply test the principle and in the future changes to the design may be required following feedback from use in theatre (when the device is fully operational).

4. Conclusion

Surgery is the one of the main methods used to treat cancer. Large tumours can be rapidly debulked or even removed entirely in a single procedure. Other treatments such as chemotherapy and radiation therapy can be used as an alternative to or in conjunction with surgery. However, surgery is perhaps the most effective way to treat a large tumour.

A variety of imaging techniques are available for surgeons to guide clinical decision-making but a lack of specificity and resolution can make their use limited. FGS is an emerging optical imaging technique adapted specifically to the operating room, which relies on the detection of fluorescence from fluorophores introduced to the patient prior to surgery. This fluorescence emission acts as a guide in real time for the surgeon to use during the resection of diseased tissues of interest. Non-specific fluorophores provide anatomical reference points for the surgeon to use. As specific markers become more readily available, specific molecular targeted FGS provides the required contrast to allow the surgeon to delineate between healthy and diseased tissues. FGS usually relies on the use of the near infrared region of the electromagnetic spectrum due to the reduced scattering and absorption afforded by the use of such wavelengths. In response to the growing interest in FGS many imaging devices have been developed to maximise excitation of the fluorophores of interest and to detect the emission with high sensitivity.

The overall aim of this work is to contribute new technology to the field of FGS to improve on the limitations within the field, namely the lack of a standard by which FGS imager performance can be quantified and also the ability to effectively image resected

tissue samples *ex-vivo*. The specific focus of this dissertation is therefore the development of a novel FGS calibrator and a clinical *ex-vivo* imager.

The FGS calibrator consists of a light detector of known performance and a stable light source (of switchable wavelength). The detector consists of a calibrated photodiode in a transimpedance amplifier circuit to convert the current of the photodiode to a voltage with a dynamic range of 10^6:1. The light source consists of an LED which is built into a negative feedback circuit to ensure a linear output over a range of set-point voltages used to set the LED brightness. The FGS calibrator is designed for calibrating clinical FGS imagers and excitation light sources for the purpose of providing information regarding the physical performance of the imager. An extension of this is that results obtained from FGS procedures can be more readily compared with the results from other groups since the limits of the devices performance are better defined. The FGS calibrator presents an alternative to calibration methods that are reported in the literature. Such calibration standards consist of fluorescent phantoms or quantum dot solutions which provide relative measures of the sensitivity limits of the device. Furthermore, these calibration standards require chemical preparation and have a finite shelf life.

To calibrate an FGS imager the calibrator detector module measures the power density of the excitation light source as a function of working distance (in units of mW/cm^2) and the light source allows the measurement of the signal-to-noise ratio as a function of photon flux (in units of $photons/s/cm^2$). By measuring the SNR as a function of the photon flux incident on the camera, the sensitivity limit to photons of a particular wavelength can be measured. In this dissertation, the sensitivity limit of the FGS imager was decided to be the photon flux detectable at an SNR of 5.

This limit is the Rose criterion, which is defined as the minimum SNR required to discern details in an image with 100% certainty. Of course, any SNR could be chosen to be the limit but this seems most appropriate as it is a defined limit.

In the previous chapters, the design and development of the FGS calibrator has been discussed highlighting the important aspects of the device design. The calibrator was used to calibrate an in-house developed imager, measuring the excitation light intensity as a function of working distance. The sensitivity limits of the in-house imager expressed in terms of a photon intensity at the Rose criterion can be measured as well but as discussed previously the data acquired could not be presented here. The future aim is to carry on this work, using the calibrator to calibrate another in-house developed clinical imager and beyond this, commercial imagers (as and when they become available). Data obtained from calibration of these imagers will serve as a reference for surgeons to make informed decisions on the best marker and imager combination for their FGS procedures. Although not discussed in this dissertation, the information obtained about the performance characteristics of an FGS imager could also be potentially used to inform a computational model. This model could be used to determine the performance of fluorophores under certain biological conditions. The biological conditions could include tissue pH, temperature and solvent (for example). The input parameters of the model would include the excitation power density of the FGS imager light source (at a specific working distance), as well as all of the characteristics of the fluorophore (such as quantum yield, concentration in the target tissue, etc.) and the characteristics of the tissue in which the fluorophore is located. The output would be the photon emission from the fluorophore which would determine

whether or not the FGS imager is suitable for that particular fluorophore considering its detection limit in terms of the photon flux.

The second part of this dissertation consists of work contributing to the devolvement of a novel *ex-vivo* imager. The *ex-vivo* imager is a device that is being developed to allow surgeons to analyse surgical margins following resection of diseased tissues.

This will enable the surgeon to decide whether further surgery is needed in the area of resection or not. When fully developed this imager has the potential of improving surgical outcomes. The imager will operate at high sensitivity by utilising a high sensitivity/low readout noise camera operating at longer exposure times to maximise light capture. A specialised excitation illuminator is included in the design to ensure effective excitation of fluorophores in the resected tissue sample. Additionally, spectral unmixing approaches will be applied to remove confounding autofluorescence signals to improve contrast.

The *ex-vivo* imager has been designed and progress has been made towards its construction. Considerable work was carried out in contribution to the design of the efficient excitation illumination system that maximises the outputs from several lasers onto a rectangular field as required by the rectangular imaging fields of camera; both 16:9 and the more usual 4:3 aspects ratios can be catered for. The system utilises multiple lasers, each of different wavelength, combined into a common light guide and delivery system. Zemax modelling software was used to develop this illumination system that was designed to excite over an area of 120×90 mm^2. Optical bench testing confirmed that the desired beam profile was achieved using the optical components confirming the Zemax model of the design. The camera is a chilled CCD-based camera that is designed to operate with low readout noise. The performance of the CCD camera

in terms of the conversion gain was determined by photon transfer measurements. The *ex-vivo* imager is currently in the process of being built and the aim will be to take the device into theatre to use in conjunction with FGS imagers. Before this however, the device will be tested using the FGS calibrator to confirm the sensitivity of the device and measure the power density of the excitation light source.

In the future, provided NIR imaging is successful with this imager, the aim is to potentially move into imaging in the short-wave infrared (SWIR) region of the optical spectrum (900 – 1700 nm). By increasing the wavelength, further reduced scattering and absorption can be exploited. Furthermore, autofluorescence is reduced even further in this region of the optical spectrum.

Additional Information

As a final note to the reader, the mechanical designs and construction of the FGS calibrator modules were carried out by the Advanced Technology Group of the Department of Oncology. I have contributed to the build of the FGS calibrator emitter and all performance tests of the emitter and detector modules were carried out by me. I have contributed to the design and writing of the control module software. Testing of the FGS calibrator device on the in-house built FGS imager was carried out by me.

I have contributed to the design of the *ex-vivo* imager by carrying out extensive modelling and experimental testing of the *ex-vivo* imager excitation light source, including early attempts to use LEDs. I carried out all other practical tests and measurements in the work contributing to the *ex-vivo* imager.

Appendices

Appendix A: FGS Calibrator Noise Calculations

To give an idea of the likely performance of the FGS calibrator detector module, the theoretical noise contributions to the output measurement signal were estimated to give an approximate idea of the number of photons that the module could effectively 'see'.

The detector module of the FGS calibrator utilises a transimpedance amplifier circuit to allow range switching with 6 possible sensitivity settings. Each range uses a different feedback resistance to set the sensitivity. The overall dynamic range is 10^6:1. It is well known that the components in a transimpedance amplifier interact and introduce noise in the signal. The sources of each noise component are described in the literature, a method of how to estimate the noise spectrum and the individual contributions is described in a Burr-Brown technical note supplied by Texas Instruments[171] as well as elsewhere[172].

The key sources of noise in the transimpedance amplifier circuit are shot (current) noise, thermal (voltage) noise and flicker (1/*f*) noise. The total noise N_{total} (expressed in V) is defined as the square root of the sum of the squares of each individual noise source as follows:

$$N_{total} = \sqrt{{N_i}^2 + {N_R}^2 + {N_{1/f}}^2} \qquad \text{(A-1)}$$

Where N_i is the current noise contribution (*rms*), N_R is the thermal noise contribution (*rms*) and $N_{1/f}$ is the flicker noise (1/*f*) noise contribution (*rms*).

The voltage contribution of the current noise is calculated using the following equation:

$$N_i = \frac{\pi}{2} \cdot R_{feedback} \cdot 10\ \text{fA}/\sqrt{\text{Hz}} \cdot \sqrt{f_O} \qquad \text{(A-2)}$$

Where $R_{feedback}$ is the resistance of the selected sensitivity range (which takes values of 1 GΩ, 6.25 MΩ, 3.91 MΩ, 244 kΩ, 15.3 kΩ or 951 Ω), 10 fA/√Hz is the current noise density of the transimpedance circuit in the detector module and f_O is the open loop gain roll off frequency (which is the frequency at which the open loop gain drops off rapidly).

The voltage contribution of the thermal noise is expressed as follows:

$$N_R = \sqrt{\left(\sqrt{4k_B TBR_{feedback}}\right)^2 + \left(\sqrt{4k_B TBR_{shunt}}\right)^2} \quad \text{(A-3)}$$

Where k_B is Boltzmann's constant, T is the temperature in K (this is the room temperature, defined here to be 300 K), B is the effective noise bandwidth (defined here as $(\pi/2) \times f_O$) and R_{shunt} is the shunt resistance of the photodiode (1 GΩ).

Finally, the contribution of the flicker noise (or $1/f$ noise) is expressed as follows:

$$N_{1/f} = \left(1 + \frac{R_{feedback}}{R_{shunt}}\right) \cdot A_N \cdot \sqrt{\ln\left(\frac{f_C}{f_A}\right)} \cdot \frac{\pi}{2} \quad \text{(A-4)}$$

Where A_N is a constant defined as the transimpedance amplifier input noise density at a frequency of 1 Hz (which is 120 nV/√Hz in this case), f_C is the upper frequency limit (the upper cut-off frequency) and f_A is the lower frequency of the system (0.01 Hz).

For the FGS calibrator the measurement bandwidth is 10 Hz for the photodiode signal. This sets the frequency for the calculations to be 5 Hz due to the Nyquist theorem for sampling. This is of course well beyond the upper input cut off frequency so there is not risk of undersampling the photodiode putout signal.

Using the previously defined equations, the noise contributions for each source were calculated at a frequency of 5 Hz.

Using the equations above the contributions of each noise source and the total noise was calculated for each feedback resistance. The results are shown in Table 9, including the total noise for each sensitivity range.

Feedback resistance (Ω)	Total 1/f noise voltage (μV)	Total current noise voltage (nV)	Total resistance noise voltage (mV)	Total (r.m.s.) noise (mV)	Total (p-p) noise (mV)
1.00×10^{9}	0.94	3.51×10^{4}	1.88	1.88	12.4
62.5×10^{6}	0.50	2.20×10^{3}	1.69	1.69	11.2
3.90×10^{6}	0.47	137	6.27	6.27	41.4
244×10^{3}	0.47	8.57	16.6	16.6	110
5.2×10^{3}	0.47	0.54	20.6	20.6	136
954	0.47	0.03	21.0	21.0	139

Table 9: Total noise calculated for the FGS calibrator detector module according to the Burr-Brown note describing the process of analysing the noise produced in a transimpedance amplifier circuit.

The results in Table 9 demonstrate the root mean square (*r.m.s.*) and peak-peak (*p-p*) noise voltages that are generated in the output signal as a result of noise generated in the transimpedance amplification system of the detector module.

This calculation can be converted into an equivalent intensity or photon flux, thereby demonstrating the required intensity/photon flux required to generate a signal to noise ratio (SNR) of 1. This can be done by first converting the total noise voltage into a current value by using Ohm's law, $V = IR$. This current value is then converted into a measurement of the power measured by the photodiode using the responsivity of the photodiode (in units of A/W). The power is converted into an intensity by dividing the power by the nominal active area of the photodiode (0.13 cm^2) and this is then finally

converted into a photon flux by dividing the intensity by the energy of a single photon (of wavelength 780 nm in this case). The results of these calculations are shown in Table 10.

Feedback Resistance (Ω)	Total (r.m.s.) noise (mV)	Equivalent input noise current (pA)	Equivalent input optical power (pW)	Equivalent input optical intensity (W/cm^2)	Equivalent input photon flux ($\times 10^6$ photons/s/cm^2)
1.00×10^9	1.88	1.88	3.84	2.96×10^{-11}	116
62.5×10^6	1.69	27.1	55.3	4.25×10^{-10}	1.67×10^3
3.9×10^6	6.27	1.60×10^3	3.27×10^3	2.52×10^{-8}	9.88×10^4
244.1×10^3	16.6	6.81×10^4	1.39×10^5	1.07×10^{-6}	4.19×10^6
5.2×10^3	20.6	1.35×10^6	2.75×10^6	2.12×10^{-5}	8.30×10^7
953.6	21.0	2.20×10^7	4.49×10^7	3.46×10^{-4}	1.36×10^9

Table 10: Equivalent input flux of photons needed to achieve a signal to noise ratio of 1 for a wavelength of 780 nm.

The results shown in Table 10 demonstrate a theoretical limit of detection that must be overcome by the input light source to produce a signal to noise ratio (SNR) of 1. Overall, this limit is acceptable given that the detector can potentially detect an optical power as low as 3.84 pW in the most sensitive range.

The intensity (or photon flux) quoted in Table 10 is dependent on the wavelength since the photodiode responsivity varies with wavelength. To completely characterise the theoretical limits of the detector performance, the above calculations must be carried out at all wavelengths but for the purposes of demonstration, the calculations shown here were conducted at a single wavelength: 780 nm. This was deemed appropriate since it is in the NIR region of the optical spectrum that the detector module will be probing.

Appendix B: Numerical Aperture and Étendue

One important aspect of optics that is referred to in this dissertation is numerical aperture and étendue. This appendix therefore serves to provide a more detailed definition of the two concepts as they are of direct relevance to this project and some of the design considerations used in the development of the FGS calibrator and *ex-vivo* imager.

B.1 Numerical Aperture

Numerical aperture (NA) is a simple parameter which succinctly describes the capability of the optical component to accept (or emit light). The parameter is defined as:

$$\mathrm{NA} = n \sin \theta \tag{B.1}$$

Where n is the refractive index of the medium in which the light is traversing and θ is the acceptance angle of the optical component. The acceptance angle is defined as the maximum angle of incidence that a light ray can have relative to the optical component to be captured by the optical component[173, 174]. The acceptance angle used to determine the NA is geometrically related to an arbitrary (plano-convex) lens as shown in Figure 55.

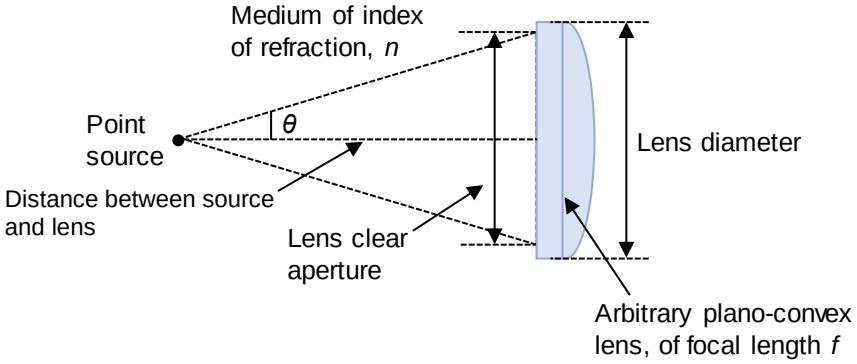


Figure 55: NA of an arbitrary plano-convex lens.

When manufacturers quote the numerical aperture of an optical component, it is related to the clear aperture of the lens and not the lens diameter, as indicated in Figure 55. The clear aperture of an optical component is the diameter of the aperture that defines the portion of the lens that offers the specified functionality[175].

The numerical aperture of optical components is important to consider when seeking high transmission of light through the system, with the smallest numerical aperture of any particular optical component defining the effectiveness of the system as a whole. Furthermore, the numerical aperture is one of the factors that defines the limit of resolution of the system which is a crucial parameter in any imaging application[176, 177]. Specifically, the resolution goes as the inverse of the numerical aperture, in terms of the Rayleigh criterion (r), which defines the diffraction limit of resolution and is expressed using the following expression:

$$r = \frac{0.6\lambda}{NA} \tag{B.2}$$

Where λ is the wavelength of light[178].

B.2 Étendue

Étendue describes the spread of a beam as it traverses an optical system. Like the numerical aperture it is an important quantity to consider when choosing the right optics to ensure efficient transmission of light. As with NA, matching the étendue ensures efficient transmission of light. The infinitesimal element of étendue ($\delta\varepsilon$) is described using the following relation[179, 180]:

$$\delta\varepsilon = n^2 \cos\theta \, \delta\omega\delta A \tag{B.3}$$

Where n is the index of refraction of the medium the incident ray is traversing before

being captured by the lens, θ is the angle of the light ray relative to the normal of the element δA (which is the element of area the ray is traversing) and $\delta\omega$ is the element of solid angle of the light ray. For a $\theta = 0$ then the infinitesimal element of étendue becomes:

$$\delta\varepsilon = n^2 \delta\omega \delta A \tag{B.4}$$

These quantities are related geometrically as demonstrated in Figure 56.

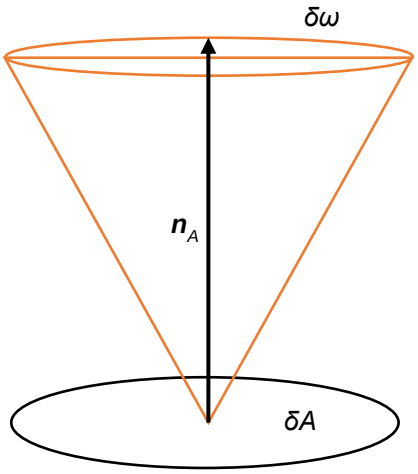


Figure 56: Geometry of the used to define the étendue of a ray traversing a medium of refractive index, *n*. The vector $\boldsymbol{n}_A$ defines the normal to the element of area denoted by δA.

Appendix C: LEDs, Laser Diodes and CCD Cameras

This appendix serves to provide a more detailed description of some of the electro-optical components mentioned in this dissertation, specifically LEDs, laser diodes and CCD cameras.

C.1 LEDs

LEDs are continuum semiconductor light sources that have been widely adopted in many different applications such as medical imaging devices, housing lights, advertising and automobile headlights amongst many others[181, 182, 183].

In a typical LED, light is generated through the process of electron hole recombination in the depletion zone of a p-n junction, the wavelength of light produced corresponding directly to the bandgap energy of the diode. The p-n junction of an LED consists of a p-doped (material with fewer electrons/more holes) fused to an n-doped material (material with a greater number of electrons), this is demonstrated in Figure 57. When a power source is connected to the LED, in the forward biased setup, current flows in the LED supplying electrons to the semiconductor which recombine with holes to produce light[184]. The wide adoption and reliance on LEDs for lighting can be attributed to the low cost of LEDs and the fact that they possess favourable properties, such as higher efficiency than other widely used light sources (such as tungsten filament bulbs), long lifetime and small light emitting area. Furthermore, many different options are available with regard to emission wavelength and package type. However, due to the production process, the packaging of LEDs are poor in terms of the optical quality of the beam[185].

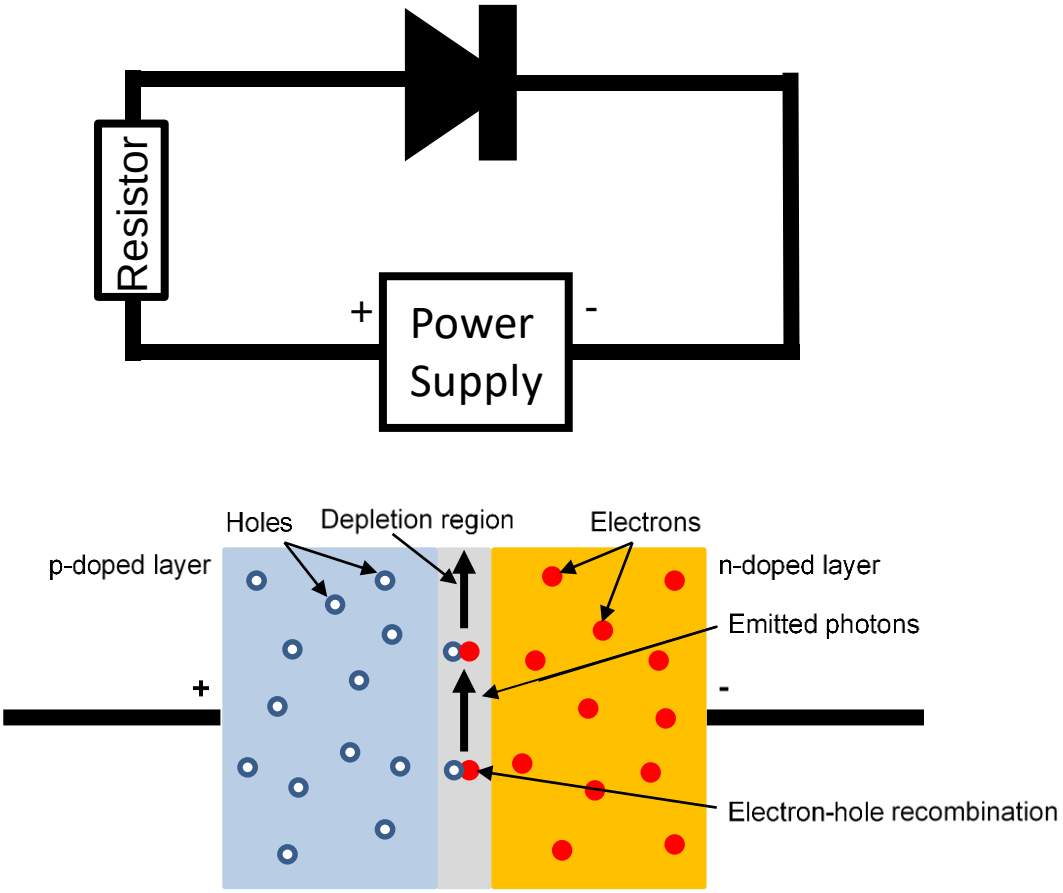


Figure 57: *Top*: Circuit diagram of a forward biased LED. *Bottom*: LED p-n junction.

C.2 Laser Diodes

Laser diodes, as with LEDs are solid state semiconductor light sources. Laser diodes are highly efficient and, despite being more expensive than LEDs, are cheaper than other types of lasers. Many different options are available in terms of the peak emission wavelength with laser diodes producing in the visible and the near infrared at a variety of wavelengths from 380 nm up to 1550 nm[185].

A typical laser diode is constructed from a heavily doped p-n junction. When a heavily doped p-n junction is formed, electrons (from the n-doped side) diffuse towards the p-doped side of the semiconductor and holes (from the p-doped side) diffuse toward the n-doped side forming an excess of electrons and holes in the depletion zone.

This presence of electrons and holes causes the build-up of an electric field called the depletion field which slows the diffusion process. Application of a voltage (forward bias) across the p-n junction causes a narrow region to form where both electrons and holes are present (this is the active region of the laser diode), which cannot occur in a normal p-n junction. The application of a forward bias voltage causes population inversion to take place in which electrons and holes recombine to produce incoherent light. If the current (injection of carriers, i.e. electrons) is high enough, above the lasing current, the laser diode starts lasing as the gain increases. As the laser diode starts lasing stimulated emission dominates over the spontaneous emission process which occurs in an LED. In the laser diode the active region of the semiconductor crystal or p-n junction acts as the gain medium[186].

C.3 CCD Cameras

The primary component of the CCD camera is the CCD chip which is typically constructed from silicon. The chip is essentially an array of photodetectors (pixels) which store charge in a potential well. The charge is generated by incoming photons, with the magnitude of the charge stored on each pixel being approximately proportional to the intensity of the incoming photons[187]. Indeed, a notable advantage of CCDs is the high linearity afforded by the device[188]. Once the integration time has elapsed, the charge stored on each pixel of the CCD is transferred by an analogue shift register and is subsequently read out.

Three types of CCD exist, these being full frame CCDs, interline transfer (ILT) CCDs (akin to the Starlight XPress used in this project for the *ex-vivo* imager) and frame transfer (FT) CCDs. Full frame CCDs are the simplest form of CCD sensor. Full frame CCDs shift the charge stored on the pixels vertically, row by row to the readout register.

When a row of charge has been shifted into the readout register the charge is shifted horizontally from one pixel to the next to read out. The disadvantage of this method is the potential for light to fall on the pixels during transfer of charge into the readout register (this is called charge smearing). Mechanical shutters are sometimes used to avoid this issue, although shutters have the potential to suffer from mechanical issues since they are a moving part. Full frame CCDs are typically the most sensitive of the three families of CCDs[189].

In ILT CCDs, once the integration time has elapsed, each line of pixels is transferred into readout columns where the charge is then read out, column by column. In FT CCDs, the charge is transferred column by column into a shielded array and subsequently read out. The benefit of ILT CCDs over FT CCDs is the higher shutter performance achievable with ILT CCDs due to the massively reduced time taken to read out the charge stored on the pixels in an ILT CCD[185, 190].

Advancements in CCD technology have also led to the development of the electron multiplying CCD (emCCD). In a typical CCD the main contributor to noise is the output amplifier. This noise can be reduced through slowing of the readout clock and averaging the output. The cost of this is that real time imaging with the CCD is prevented, although noise is heavily reduced. The emCCD prevents the need for this trade-off by increasing the gain in the readout electronics of the CCD[185, 191].

References

[1] World Health Organisation (WHO). (2018). All cancers. Available at: https://doi.org/L11\n10.1051/0004-6361/201016331

[2] World Health Organisation (WHO) (2018) *Cancer: Key Facts*. Available at: https://www.who.int/news-room/fact-sheets/detail/cancer.

[3] Cancer Research UK (2018) 'Cancer in the UK | 2018'.

[4] Cancer Research UK (2014) *Cancer survival statistics | Cancer Research UK*. Available at: https://www.cancerresearchuk.org/health-professional/cancer-statistics/survival (Accessed: 25 November 2018).

[5] Cancer Research UK (2017) *Treatment for cancer | Cancer in general | Cancer Research UK*. Available at: https://www.cancerresearchuk.org/about-cancer/cancer-in-general/treatment (Accessed: 17 November 2017).

[6] NHS (2017) *Radiotherapy - NHS*. Available at: https://www.nhs.uk/conditions/radiotherapy/ (Accessed: 5 December 2018).

[7] Tringale, K. R., Pang, J., & Nguyen, Q. T. (2018). Image-guided surgery in cancer: A strategy to reduce incidence of positive surgical margins. *Wiley Interdisciplinary Reviews: Systems Biology and Medicine*, *10*(3), e1412. https://doi.org/10.1002/wsbm.1412

[8] Wright, J. L., Dalkin, B. L., True, L. D., Ellis, W. J., Stanford, J. L., Lange, P. H. and Lin, D. W. (2010). Positive Surgical Margins at Radical Prostatectomy Predict Prostate Cancer Specific Mortality. *Journal of Urology*, *183*(6), 2213–2218. https://doi.org/10.1016/j.juro.2010.02.017

[9] Keereweer, S., Kerrebijn, J. D. F., Van Driel, P. B. A. A., Xie, B., Kaijzel, E. L., Snoeks, T. J. A., Que, I., Hutteman, M., van der Vorst, J. R., Mieog, J. S. D., Vahrmeijer, A. L., van de Velde, C. J. H., Baatenburg de Jong, R. J. and Löwik, C. W. G. M. (2011). Optical image-guided surgery - Where do we stand? *Molecular Imaging and Biology*. https://doi.org/10.1007/s11307-010-0373-2

[10] Fei, B., Lu, G., Wang, X., Zhang, H., Little, J. V., Magliocca, K. R. and Chen, A. Y. (2017). Tumor margin assessment of surgical tissue specimen of cancer patients using label-free hyperspectral imaging. *Advanced Biomedical and Clinical Diagnostic and Surgical Guidance Systems XV*, *10054*, 100540E. https://doi.org/10.1117/12.2249803

[11] Low, P. S., Singhal, S. and Srinivasarao, M. (2018). Fluorescence-guided surgery of cancer: applications, tools and perspectives, 64–72.

[12] Zheng, Y., Yang, H., Wang, H., Kang, K., Zhang, W., Ma, G. and Du, S. (2019). Fluorescence-guided surgery in cancer treatment: Current status and future perspectives. *Journal of Threatened Taxa*, *7*(Suppl 1), 4–7. https://doi.org/10.21037/atm.2019.01.26

[13] Chest x-ray | Diagnosing lung cancer | Cancer Research UK. (no date). Retrieved January 16, 2018, from https://www.cancerresearchuk.org/about-cancer/lung-cancer/getting-diagnosed/tests/chest-x-ray

[14] Bone Cancer: Diagnosis | Cancer.Net. (no date). Retrieved January 16, 2018, from https://www.cancer.net/cancer-types/bone-cancer/diagnosis

[15] X-Ray Generators. (no date). Retrieved February 22, 2018, from https://www.nde-ed.org/EducationResources/CommunityCollege/Radiography/EquipmentMaterials/xrayGenerators.htm

[16] Bansal, G. J. (2006). Digital radiography. A comparison with modern conventional imaging. *Postgraduate Medical Journal*, *82*(969), 425–428. https://doi.org/10.1136/pgmj.2005.038448

[17] Goldman, L. W. (2007). Principles of CT and CT Technology. *Journal of Nuclear Medicine Technology*, *35*(3), 115–128. https://doi.org/10.2967/jnmt.107.042978

[18] Institute of Physics (no date) *X-ray imaging*. Available at: https://www.iop.org/education/teacher/resources/teaching-medical-physics/xray/page_56315.html#gref (Accessed: 1 June 2019).

[19] Mahesh, M. (2012). *MDCT Physics: The Basics: Technology, Image Quality and Radiation Dose*.

[20] Lubell, D. L. (2005) 'Drawbacks and limitations of computed tomography', *Texas Heart Institute Journal*, 32(2), p. 250.

[21] James, M. L. and Gambhir, S. S. (2012). A Molecular Imaging Primer: Modalities, Imaging Agents, and Applications. *Physiological Reviews*, *92*(2), 897–965. https://doi.org/10.1152/physrev.00049.2010

[22] Grover, V. P. B., Tognarelli, J. M., Crossey, M. M. E., Cox, I. J., Taylor-Robinson, S. D. and McPhail, M. J. W. (2015). Magnetic Resonance Imaging: Principles and Techniques: Lessons for Clinicians. *Journal of Clinical and Experimental Hepatology*, *5*(3), 246–255. https://doi.org/10.1016/j.jceh.2015.08.001

[23] Van Reeth, E., Tham, I. W. K., Tan, C. H. and Poh, C. L. (2012). Super-resolution in magnetic resonance imaging: A review. *Concepts in Magnetic Resonance Part A*, *40A*(6), 306–325. https://doi.org/10.1002/cmr.a.21249

[24] Tempany, C. M. C., Carroll, P. R. and Leapman, M. S. (no date). The role of magnetic resonance imaging in prostate cancer. Retrieved January 10, 2018, from https://www.uptodate.com/contents/the-role-of-magnetic-resonance-imaging-in-prostate-cancer

[25] Radhakrishna, S., Agarwal, S., Parikh, P. M., Kaur, K., Panwar, S., Sharma, S., Dey, A., Saxena, K. K., Chandra, M. and Sud, S. (2018). Role of magnetic resonance imaging in breast cancer management. *South Asian journal of cancer*, *7*(2), 69–71. https://doi.org/10.4103/sajc.sajc_104_18

[26] Martin, D. J., Wells, I. T. P. and Goodwin, C. R. (2015). Physics of ultrasound. *Anaesthesia & Intensive Care Medicine*, *16*(3), 132–135. https://doi.org/10.1016/j.mpaic.2015.01.003

[27] RadiologyInfo.org (no date) *Ultrasound (Sonography)*. Available at: https://www.radiologyinfo.org/en/info.cfm?pg=genus (Accessed: 8 January 2018).

[28] Pysz, M. A., Gambhir, S. S. and Willmann, J. K. (2010) 'Molecular Imaging: Current Status and Emerging Strategies', *Clinical Radiology*, 23(1), pp. 1–7. https://doi.org/10.1016/j.crad.2010.03.011

[29] Gambhir, S. S. (2002). Molecular imaging of cancer with positron emission tomography. *Nature Reviews Cancer*, *2*(9), 683–693. https://doi.org/10.1038/nrc882

[30] Stephen, Z. R., Kievit, F. M. and Zhang, M. (2011). Magnetite Nanoparticles for Medical MR Imaging. *Materials today*, *14*(7-8), 330–338. https://doi.org/10.1016/S1369-7021(11)70163-8

[31] GeneCards The Human Gene Database. (no date). VCAM1 Gene (Protein Coding) Vascular Cell Adhesion Molecule 1. Retrieved July 1, 2018, from https://www.genecards.org/cgi-bin/carddisp.pl?gene=VCAM1

[32] Zarghami, N., Khrapitchev, A. A., Perez-Balderas, F., Soto, M. S., Larkin, J. R., Bau, L. and Sibson, N. R. (2018). Optimization of molecularly targeted MRI in the brain: Empirical comparison of sequences and particles. *International Journal of Nanomedicine*, *13*, 4345–4359. https://doi.org/10.2147/IJN.S158071

[33] Reuveni, T., Motiei, M., Romman, Z., Popovtzer, A., and Popovtzer, R. (2011). Targeted gold nanoparticles enable molecular CT imaging of cancer: an in vivo study. *International Journal of Nanomedicine*, (2859–2864). https://pubmed.ncbi.nlm.nih.gov/22131831/

[34] Harvey, C. (2015). Ultrasound with microbubbles. *Cancer Imaging*, *15*(Suppl 1), O19. https://doi.org/10.1186/1470-7330-15-S1-O19

[35] Deshpande, N., Needles, A. and Willmann, J. K. (2010). Molecular ultrasound imaging: current status and future directions. *Clinical radiology*, *65*(7), 567–581. https://doi.org/10.1016/j.crad.2010.02.013

[36] Nabi, H. A. and Zubeldia, J. M. (2002). Clinical applications of 18F-FDG in oncology. *Journal of nuclear medicine technology*, *30*(1), 3-9.

[37] Vandenberghe, S., Mikhaylova, E., D'Hoe, E., Mollet, P. and Karp, J. S. (2016). Recent developments in time-of-flight PET. *EJNMMI Physics*, *3*(1). https://doi.org/10.1186/s40658-016-0138-3

[38] Gritters, L. S. and Wahl, R. L. (1993) 'Single photon emission computed tomography in cancer imaging.', *Oncology*, 7(7), pp. 59–63, 66 discussion 66, 69.

[39] Khalil, M. M., Tremoleda, J. L., Bayomy, T. B. and Gsell, W. (2011). Molecular SPECT Imaging: An Overview. *International Journal of Molecular Imaging*, *2011*, 1–15. https://doi.org/10.1155/2011/796025

[40] Weissleder, R. and Pittet, M. J. (2008). Imaging in the era of molecular oncology. *Nature*, *452*(7187), 580–589. https://doi.org/10.1038/nature06917

[41] Nishida, N., Yano, H., Nishida, T., Kamura, T. and Kojiro, M. (2006). Angiogenesis in cancer. *Vascular health and risk management*, *2*(3), 213–219.

[42] Hillen, F. and Griffioen, A. W. (2007). Tumour vascularization: sprouting angiogenesis and beyond. *Cancer and Metastasis Reviews*, *26*(3–4), 489–502. https://doi.org/10.1007/s10555-007-9094-7

[43] Sheth, R. A. and Mahmood, U. (2010). Optical molecular imaging and its emerging role in colorectal cancer. *American Journal of Physiology-Gastrointestinal and Liver Physiology*, *299*(4), G807–G820. https://doi.org/10.1152/ajpgi.00195.2010

[44] National Institute of Biomedical Imaging and Engineering. (no date). Optical Imaging. Retrieved August 3, 2018, from https://www.nibib.nih.gov/science-education/science-topics/optical-imaging

[45] Hemmer, E., Benayas, A., Légaré, F. and Vetrone, F. (2016). Exploiting the biological windows: current perspectives on fluorescent bioprobes emitting above 1000 nm. *Nanoscale Horizons*, *1*(3), 168–184. https://doi.org/10.1039/C5NH00073D

[46] Wang, T. D. and Van Dam, J. (2004). Optical biopsy: a new frontier in endoscopic detection and diagnosis. *Clinical gastroenterology and hepatology : the official clinical practice journal of the American Gastroenterological Association*, *2*(9), 744–753.

[47] Huang, D., Swanson, E. A, Lin, C. P., Schuman, J. S., Stinson, W. G., Chang, W., Hee, M. R., Flotte, T., Gregory, K., Puliafito, C. A. and Fujimoto, J. G. (1991). Optical Coherence Tomography, 1–4.

[48] Ibne Mokbul, M. (2017). Optical Coherence Tomography: Basic Concepts and Applications in Neuroscience Research. *Journal of Medical Engineering*, 1–20. https://doi.org/10.1155/2017/3409327

[49] Izatt, J. A., Hee, M. R., Swanson, E. A., Lin, C. P., Huang, D., Schuman, J. S., Puliafito, C. A. and Fujimoto, J. G. (1994). Micrometer-Scale Resolution Imaging of the Anterior Eye In Vivo With Optical Coherence Tomography. *Clinical Sciences*, *112*(12), 1584–1589.

[50] Schmitt, J., Kolstad, D. and Petersen, C. (2005). Intravascular Optical Coherence Tomography – Opening a Window into Coronary Artery Disease. *European Cardiology Review*, *1*(1), 1. https://doi.org/10.1364/OPN.15.2.000020

[51] Xu, M. and Wang, L. V. (2006). Photoacoustic imaging in biomedicine. *Review of Scientific Instruments*, *77*(4). https://doi.org/10.1063/1.2195024

[52] Beard, P. (2011). Biomedical photoacoustic imaging. *Interface Focus*, *1*(4), 602–631. https://doi.org/10.1098/rsfs.2011.0028

[53] Hoshi, Y. and Yamada, Y. (2016). Overview of diffuse optical tomography and its clinical applications. *Journal of Biomedical Optics*, *21*(9), 091312. https://doi.org/10.1117/1.JBO.21.9.091312

[54] Corlu, A., Choe, R., Durduran, T., Rosen, M. A., Schweiger, M., Arridge, S. R., Schnall, M. D. and Yodh, A. G. (2007). Three-dimensional in vivo fluorescence diffuse optical tomography of breast cancer in humans. *Optics Express*, *15*(11), 6696. https://doi.org/10.1364/oe.15.006696

[55] Hasnain, A., Mehta, K., Zhou, X., Li, H. and Chen, N. (2018). Laplace-domain diffuse optical measurement. *Scientific Reports*, *8*(1), 1–8. https://doi.org/10.1038/s41598-018-30353-5

[56] Durduran, T., Choe, R., Baker, W. B. and Yodh, A. G. (2010). Diffuse Optics for Tissue Monitoring and Tomography. *Reports on Progress in Physics*, *73*(7). https://doi.org/10.1088/0034-4885/73/7/076701

[57] Fenn, M. B., Xanthopoulos, P., Pyrgiotakis, G., Grobmyer, S. R., Pardalos, P. M. and Hench, L. L. (2011). Raman spectroscopy for clinical oncology. *Advances in Optical Technologies*, *2011*. https://doi.org/10.1155/2011/213783

[58] Orosco, R. K., Tsien, R. Y. and Nguyen, Q. T. (2013). Fluorescence Imaging in Surgery. *IEEE Reviews in Biomedical Engineering*, *6*, 178–187. https://doi.org/10.1109/RBME.2013.2240294

[59] Vahrmeijer, A., Hutteman, M., van der Vorst, J. R., van de Velde, C. J. H. and Frangioni, J. V. (2013). Image-Guided Cancer Surgery Using Near-Infrared Fluorescence. *Nature Reviews Clinical Oncology*, *10*(9), 507–518. https://doi.org/10.1038/nrclinonc.2013.123

[60] Nagaya, T., Nakamura, Y. A., Choyke, P. L. and Kobayashi, H. (2017). Fluorescence-Guided Surgery. *Frontiers in Oncology*, *7*. https://doi.org/10.3389/fonc.2017.00314

[61] Jeschke, S., Lusuardi, L., Myatt, A., Hruby, S., Pirich, C. and Janetschek, G. (2012). Visualisation of the lymph node pathway in real time by laparoscopic radioisotope- and fluorescence-guided sentinel lymph node dissection in prostate cancer staging. *Urology*, *80*(5), 1080–1087. https://doi.org/10.1016/j.urology.2012.05.050

[62] Van Der Poel, H. G., Buckle, T., Brouwer, O. R., Valdés Olmos, R. A. and Van Leeuwen, F. W. B. (2011). Intraoperative laparoscopic fluorescence guidance to the sentinel lymph node in prostate cancer patients: Clinical proof of concept of an integrated functional imaging approach using a multimodal tracer. *European Urology*. https://doi.org/10.1016/j.eururo.2011.03.024

[63] Yeung, T. M., Volpi, D., Tullis, I. D. C., Nicholson, G. A., Buchs, N., Cunningham, C., Guy, R., Lindsay, I., George, B., Jones, O., Wang, L. M., Hompes, R., Vojnovic, B., Hamdy, F. and Mortensen, N. J. (2016). Identifying Ureters In Situ Under Fluorescence During Laparoscopic and Open Colorectal Surgery. *Annals of Surgery*, *263*(1), e1–e2. https://doi.org/10.1097/SLA.0000000000001513

[64] Verbeek, F. P. R., van der Vorst, J. R., Tummers, Q. R. J. G., Boonstra, M. C., de Rooij, K. E., Löwik, C. W. G. M., Valentijn, A. R. P. M., van de Velde, C. J. H., Choi, H. S., Frangioni, J. V. and Vahrmeijer, A. L. (2014). Near-infrared Fluorescent Imaging of Both Colorectal Cancer and Ureters Using a Low-Dose

Integrin Targeted Probe, *21*(0 4), 528–537. https://doi.org/10.1245/s10434-014-3524-x

[65] Mangano, M. S., De Gobbi, A., Beniamin, F., Lamon, C., Ciaccia, M. and Maccatrozzo, L. (2018). Robot-assisted nerve-sparing radical prostatectomy using near-infrared fluorescence technology and indocyanine green: initial experience. *Urologia Journal*, *85*(1), 29–31. https://doi.org/10.5301/uj.5000244

[66] Long Island Surgery, P. C. (2015). Laparoscopic Surgery. Retrieved February 2, 2018, from http://www.longislandsurgery.org/laparoscopic.html

[67] Mondal, P. P. and Diaspro, A. (2003). *Fundamentals of Fluorescence Microscopy: Exploring Life with Light*.

[68] Lleres, D., Swift, S. and Lamond, A. I. (2007). Detecting Protein-Protein Interactions In Vivo with FRET using Multiphoton Fluorescence Lifetime Imaging Microscopy (FLIM). *Current Protocols in Cytometry*, (October). https://doi.org/10.1002/0471142956.cy1210s42

[69] Topaloglu, N., Gulsoy, M. and Yuksel, S. (2013). Antimicrobial photodynamic therapy of resistant bacterial strains by indocyanine green and 809-nm diode laser. *Photomedicine and Laser Surgery*, *31*(4), 155–162. https://doi.org/10.1089/pho.2012.3430

[70] Hong, G., Antaris, A. L. and Dai, H. (2017). Near-infrared fluorophores for biomedical imaging. *Nature Biomedical Engineering*, *1*(1), 10. https://doi.org/10.1038/s41551-016-0010

[71] Landsman, M. L. J., Kwant, G., Mook, G. A. and Zijlstra, W. G. (1976). Light absorbing properties, stability, and spectral stabilization of indocyanine green. *Journal of Applied Physiology*, *40*(4), 575–583. https://doi.org/10.1152/jappl.1976.40.4.575

[72] Choyke, P. L., Alford, R., Simpson, H. M., Duberman, J., Craig Hill, G., Ogawa, M., Regino, C. and Kobayashi, H. (2009). Toxicity of organic fluorophores used in molecular imaging: Literature review. *Molecular Imaging*, *8*(6), 341–354. https://doi.org/10.2310/7290.2009.00031

[73] Schaafsma, B. E., Mieog, J. S. D., Hutteman, M., Van Der Vorst, J. R., Kuppen, P. J. K., Löwik, C. W. G. M., Frangioni, J. V., van de Velde, C. J, H. and Vahrmeijer, A. L. (2011). The clinical use of indocyanine green as a near-infrared fluorescent contrast agent for image-guided oncologic surgery. *Journal of Surgical Oncology*. https://doi.org/10.1002/jso.21943

[74] Alander, J. T., Kaartinen, I., Laakso, A., Pätilä, T., Spillmann, T., Tuchin, V. V., Venermo, M. and Välisuo, P. (2012). A Review of Indocyanine Green Fluorescent Imaging in Surgery. *International Journal of Biomedical Imaging*, 1–26. https://doi.org/10.1155/2012/940585

[75] Jiang, J. X., Keating, J. J., De Jesus, E. M., Judy, R. P., Madajewski, B., Venegas, O., Okusanya, O. T. and Singhal, S. (2015) 'Optimization of the enhanced permeability and retention effect for near-infrared imaging of solid tumors with indocyanine green.', *American journal of nuclear medicine and molecular imaging*, 5(4), pp. 390–400. https://pubmed.ncbi.nlm.nih.gov/26269776/

[76] Matsumura, Y. and Maeda, H. (1986) 'A New Concept for Macromolecular Therapeutics in Cancer Chemotherapy: Mechanism of Tumoritropic Accumulation of Proteins and the Antitumor Agent Smancs', *Cancer Research*, 46(8), pp. 6387–6392.

[77] Porcu, E. P., Salis, A., Gavini, E., Rassu, G., Maestri, M. and Giunchedi, P. (2016). Indocyanine green delivery systems for tumour detection and treatments. *Biotechnology Advances*, *34*(5), 768–789. https://doi.org/10.1016/j.biotechadv.2016.04.001

[78] Tummers, Q. R. J. G., Verbeek, F. P. R., Schaafsma, B. E., Boonstra, M. C., van der Vorst, J. R., Liefers, G. J., van de Velde, C. J., Frangioni, J. V. and Vahrmeijer, A. L. (2014). Real-Time Intraoperative Detection of Breast Cancer using Near-infrared Fluorescence Imaging and Methylene Blue. *European Journal of Surgical Oncology*, *40*(7), 850-858. https://doi.org/10.1016/j.ejso.2014.02.225

[79] Zakaria, S., Hoskin, T. L. and Degnim, A. C. (2008) 'Safety and technical success of methylene blue dye for lymphatic mapping in breast cancer', *American Journal of Surgery*, 196(2), pp. 228–233. https://doi.org/10.1016/j.amjsurg.2007.08.060

[80] Verbeek, F. P., van der Vorst, J. R., Schaafsma, B. E., Swijnenburg, R. J., Gaarenstroom, K. N., Elzevier, H. W., van de Velde, C. J., Frangioni, J. V. and Vahrmeijer, A. L. (2013). Intraoperative near infrared fluorescence guided identification of the ureters using low dose methylene blue: a first in human experience. *The Journal of urology*, *190*(2), 574–579. https://doi.org/10.1016/j.juro.2013.02.3187

[81] Ginimuge, P. R. and Jyothi, S. D. (2010) 'Methylene blue: Revisited', *Journal of Anaesthesiology Clinical Pharmacology*, 26(4), pp. 517–520.

[82] Klinik, N., Stummer, W., Pichlmeier, U., Meinel, T., Wiestler, D., Zanella, F. and Reulen, H. J. (2006). Fluorescence-guided surgery with 5-aminolevulinic acid for resection of malignant glioma: a randomised controlled multicentre phase III trial. *The Lancet Oncology*, *7*, 392–401. https://doi.org/10.1016/S1470-2045(06)

[83] Colditz, M. J. and Jeffree, R. L. (2012) 'Aminolevulinic acid (ALA)-protoporphyrin IX fluorescence guided tumour resection. Part 1: Clinical, radiological and pathological studies', *Journal of Clinical Neuroscience*, 19(11), pp. 1471–1474. https://doi.org/10.1016/j.jocn.2012.03.009

[84] Jichlinski, P., Forrer, M., Mizeret, J., Glanzmann, T., Braichotte, D., Wagnieres, G., Zimmer, G., Guillou, L., Schmidlin, F., Graber, P., van den Bergh, H. and Leisinger, H. J. (1997) Clinical evaluation of a method for detecting superficial surgical transitional cell carcinoma of the bladder by light-induced fluorescence of protoporphyrin IX following the topical application of 5-aminolevulinic acid: preliminary results, *Lasers in Surgical Medicine*, 20(4), pp. 402–408. https://doi.org/10.1002/(SICI)1096-9101(1997)20:4<402::AID-LSM5>3.0.CO;2-U

[85] Jichlinski, P., Guillou, L., Karlsen, S. J., Malmstrom, P. U., Jocham, D., Brennhovd, B., Johansson, E., Gärtner, T., Lange, N., van den Bergh, H. and Leisinger, H-J. (2003) Hexyl aminolevulinate fluorescence cystoscopy: new diagnostic tool for photodiagnosis of superficial bladder cancer – a multicenter study. *Journal of Urology*, 170(1), 226–9. https://doi.org/10.1097/01.ju.0000060782.52358.04

[86] Fukuhara, H., Inoue, K., Kurabayashi, A., Furihata, M. and Shuin, T. (2015) Performance of 5-aminolevulinic-acid-based photodynamic diagnosis for radical prostatectomy. *BMC Urology* 15(78). https://doi.org/10.1186/s12894-015-0073-y

[87] Moore, G. E., Peyton, W. T., French, L. A. and Walker, W. W. (1948). The clinical use of fluorescein in neurosurgery. *Journal of Neurosurgery*, *5*(4), 392–398.

[88] Diaz, R. J., Dios, R. R., Hattab, E. M., Burrell, K., Rakopoulos, P., Sabha, N., Hawkins, C., Zadeh, G., Rutka, J. T. and Cohen-Gadol, A. A. (2015). Study of the biodistribution of fluorescein in glioma-infiltrated mouse brain and histopathological correlation of intraoperative findings in high-grade gliomas resected under fluorescein fluorescence guidance. *Journal of Neurosurgery*, *122*(6), 1360–1369. https://doi.org/10.3171/2015.2.JNS132507

[89] Schwake, M., Stummer, W., Suero Molina, E. J. and Wölfer, J. (2015). Simultaneous fluorescein sodium and 5-ALA in fluorescence-guided glioma surgery. *Acta Neurochirurgica*, *157*(5), 877–879. https://doi.org/10.1007/s00701-015-2401-0

[90] Hernot, S., van Manen, L., Debie, P., Mieog, J. S. D. and Vahrmeijer, A. L. (2019). Latest developments in molecular tracers for fluorescence image-guided cancer surgery. *The Lancet Oncology*, *20*(7), e354–e367. https://doi.org/10.1016/S1470-2045(19)30317-1

[91] Fernández, M., Javaid, F. and Chudasama, V. (2018) 'Advances in targeting the folate receptor in the treatment/imaging of cancers', *Chemical Science*, 9(4), pp. 790–810. https://doi.org/10.1039/c7sc04004k

[92] Van Dam, G. M., Themelis, G., Crane, L. M. A., Harlaar, N. J., Pleijhuis, R. G., Kelder, W., Sarantopoulos, A., de Jong, J. S., Arts, H. J. G., van der Zee, A. G. J., Bart, J., Low, P. S. and Ntziachristos, V. (2011). Intraoperative tumor-specific fluorescence imaging in ovarian cancer by folate receptor-α targeting: First in-human results. *Nature Medicine*, *17*(10), 1315–1319. https://doi.org/10.1038/nm.2472

[93] Leamon, C. P. and Low, P. S. (1991) 'Delivery of macromolecules into living cells: A method that exploits folate receptor endocytosis', *Proceedings of the National Academy of Sciences of the United States of America*, 88(13), pp. 5572–5576. https://doi.org/10.1073/pnas.88.13.5572

[94] Low, P. S., Henne, W. A. and Doorneweerd, D. D. (2008) 'Discovery and development of folic-acid-based receptor targeting for imaging and therapy of cancer and inflammatory diseases', *Accounts of Chemical Research*, 41(1), pp. 120–129. https://doi.org/10.1021/ar7000815

[95] Nakajima, T., Mitsunaga, M., Bander, N. H., Heston, W. D., Choyke, P. L. and Kobayashi, H. (2011). Targeted, activatable, in vivo fluorescence imaging of Prostate-Specific Membrane Antigen (PSMA) positive tumors using the quenched humanized J591 antibody-indocyanine green (ICG) conjugate. *Bioconjugate Chemistry*, *22*(8), 1700–1705. https://doi.org/10.1021/bc2002715

[96] Ogawa, M., Kosaka, N., Longmire, M. R., Urano, Y., Choyke, P. L. and Kobayashi, H. (2009). Fluorophore-quencher based activatable targeted optical probes for detecting in vivo cancer metastases. *Molecular Pharmaceutics*, *6*(2), 386–395. https://doi.org/10.1021/mp800115t

[97] Chang, S. S. (2004). Overview of Prostate-Specific Membrane Antigen. *Reviews in Urology*, *6*, 13–18.

[98] Nguyen, Q. T. and Tsien, R. Y. (2013) 'Fluorescence-guided surgery with live molecular navigation - a new cutting edge.', *Nature Reviews Cancer*. Nature Publishing Group, 13, pp. 653–662. https://doi.org/10.1038/nrc3566

[99] Kobayashi, H. and Choyke, P. L. (2012) 'Target-cancer cell specific activatable fluorescence imaging probes: Rational Design and in Vivo Applications', *Accounts of chemical research*, 44(2), pp. 83–90. https://doi.org/10.1021/ar1000633

[100] Urano, Y., Sakabe, M., Kosaka, N., Ogawa, M., Mitsunaga, M., Asanuma, D., Kamiya, M., Young, M. R., Nagano, T., Choyke, P. L. and Kobayashi, H. (2011) Rapid cancer detection by topically spraying a γ- glutamyltranspeptidase-activated fluorescent probe. *Science Translational Medicine*, *3*(110). https://doi.org/10.1126/scitranslmed.3002823

[101] DSouza, A. V., Lin, H., Henderson, E. R., Samkoe, K. S. and Pogue, B. W. (2016). Review of fluorescence guided surgery systems: identification of key performance capabilities beyond indocyanine green imaging. *Journal of Biomedical Optics*, *21*(8), 080901. https://doi.org/10.1117/1.JBO.21.8.080901

[102] Spring, K. R. and Davidson, M. W. (no date) *Quantum Efficiency*. Available at: https://hamamatsu.magnet.fsu.edu/articles/quantumefficiency.html (Accessed: 30 January 2018).

[103] Dussault, D. and Hoess, P. (2004) 'Noise performance comparison of ICCD with CCD and EMCCD cameras', *Infrared Systems and Photoelectronic Technology*, 5563, p. 195. https://doi.org/10.1117/12.561839

[104] Scientifica (no date) *Cameras for fluorescence imaging: A comparative guide*. Available at: https://www.scientifica.uk.com/learning-zone/cameras-for-fluorescence-imaging (Accessed: 30 January 2018).

[105] Quest (no date) *The Quest Spectrum® | Fluorescence Imaging System*. Available at: https://www.quest-mi.com/products.html (Accessed: 24 March 2018).

[106] Anastasopoulou, M., Koch, M., Gorpas, D., Karlas, A., Klemm, U., Garcia-Allende, P. B. and Ntziachristos, V. (2016) Comprehensive phantom for interventional fluorescence molecular imaging. *Journal of Biomedical Optics*, 21(9). https://doi.org/10.1117/1.JBO.21.9.091309

[107] Gorpas, D., Koch, M., Anastasopoulou, M., Klemm, U., Ntziachristos, V., (2017) Benchmarking of fluorescence cameras through the use of a composite phantom. *Journal of Biomedical Optics*, 22(1). https://doi.org/10.1117/1.JBO.22.1.016009

[108] Zhu, B., Rasmussen, J. C., Litorja, M. and Sevick-Muraca, E. M. (2016) Determining the Performance of Fluorescence Molecular Imaging Devices Using Traceable Working Standards with SI Units of Radiance. *IEEE Transactions on Medical Imaging*, 35(3), pp. 802-811. https://doi.org/10.1109/TMI.2015.2496898

[109] He, L., Long Rodney, L., Antani, S. and Thoma R., G. (2012). Histology image analysis for carcinoma detection and grading. *Computer Methods and Programs in Biomedicine*, 107(3), pp. 538-556. https://doi.org/10.1016/j.cmpb.2011.12.007

[110] Volpi, D., Tullis, I. D. C., Laios, A., Pathiraja, P. N. J., Haldar, K., Ahmed, A. A. and Vojnovic, B. (2014). A novel multiwavelength fluorescence image-guided surgery imaging system. *Advanced Biomedical and Clinical Diagnostic Systems XII*, *8935*, 89350G. https://doi.org/10.1117/12.2038377

[111] Dickerscheid, D., Lavalaye, J., Romijn, L. and Habraken, J. (2013). Contrast-noise-ratio (CNR) analysis and optimisation of breast-specific gamma imaging (BSGI) acquisition protocols. *EJNMMI Research*, *3*(1), 1–9. https://doi.org/10.1186/2191-219X-3-21

[112] Bao, Q. and Chatziioannou, A. F. (2010). Estimation of the minimum detectable activity of preclinical PET imaging systems with an analytical method. *Medical Physics*, *37*(11), 6070–6083. https://doi.org/10.1118/1.3495817

[113] Hoogstins, C., Burggraaf, J. J., Koller, M., Handgraaf, H., Boogerd, L., van Dam, G. and Burggraaf, J. (2019). Setting Standards for Reporting and Quantification in Fluorescence-Guided Surgery. *Molecular Imaging and Biology*, *21*(1), 11–18. https://doi.org/10.1007/s11307-018-1220-0

[114] Pogue, B. W., Gioux, S. and Hoogstins, C. E. S. (2017). Image guided surgery using near-infrared fluorescence: road to clinical translation of novel probes for real time tumor visualization. *Molecular-Guided Surgery: Molecules, Devices, and Applications III*.

[115] RGB Photonics GmbH: Spectrometers. (no date). Retrieved June 11, 2018, from https://www.rgb-photonics.com/products/spectrometers/product/qmini/

[116] Thorlabs - FDS100-CAL Calibrated Si Photodiode, 350 - 1100 nm, 3.6 x 3.6 mm Active Area. (no date). Retrieved August 1, 2018, from https://www.thorlabs.com/thorproduct.cfm?partnumber=FDS100-CAL

[117] Photodiode Theory of Operation | Optoelectronic Components | LEDs, Laser Diodes & Detectors | AP Technologies UK. (no date). Retrieved January 15, 2018, from https://www.aptechnologies.co.uk/support/SiPDs/operation

[118] Paschotta, R. (2018). Photodiodes: Technology and Applications.

[119] Darmont, A. (2009). Spectral response of silicon image sensors, *4*(April), 1–13.

[120] Microchip Technology inc. (2011). MCP9808 Maximum Accuracy Digital Temperature Sensor Datasheet. *Microchip Technology Inc.*, *25*, 1–54.

[121] Microchip Technology inc. (2004). 24AA128/24LC128/24FC128 128K I2C™ CMOS Serial EEPROM, (6), 1–27.

[122] OSI Optoelectronics. (no date). Photodiode Characteristics and Applications, 3–5.

[123] Vishay Semiconductors. (2011). VEMD2523SLX01 Vishay Semiconductors, Silicon PIN Photodiode. *Data Sheet*, 1–5.

[124] Vaskuri, A., Petri, K., Baumgartner, H. and Kantamaa, O. (2018). Relationships between junction temperature, electroluminescence spectrum and ageing of light-emitting diodes. https://doi.org/10.1088/1681-7575/aaaed2

[125] Raypah, M. E., Devarajan, M. and Sulaiman, F. (2017). Modeling spectra of low-power SMD LEDs as a function of ambient temperature. *IEEE Transactions on Electron Devices*, *64*(3), 1180–1186. https://doi.org/10.1109/TED.2017.2656862

[126] Edmund Optics. (no date). 1000µm Aperture Diameter, Unmounted, Precision Pinhole. Retrieved from https://www.edmundoptics.co.uk/p/1000mum-aperture-diameter-unmounted-precision-pinhole/4547/

[127] Edmund Optics. (no date). Opal Diffusing Glass. Retrieved June 18, 2018, from https://www.edmundoptics.co.uk/f/opal-diffusing-glass/11914/

[128] Thorlabs. (no date). Neutral Density Filters: Absorptive/Reflective. Retrieved June 18, 2019, from https://www.thorlabs.com/navigation.cfm?guide_ID=2185

[129] Microchip Technology inc. (2012), PIC18F45K50-I/PT.

[130] MAX1169 Maxim. (no date). 2-Wire Serial ADC in a 14-Pin TSSOP in a 14-Pin TSSOP, 1–20.

[131] What Is LabWindows/CVI? - National Instruments. (no date). Retrieved January 10, 2018, from https://www.ni.com/en-gb/shop/electronic-test-instrumentation/programming-environments-for-electronic-test-and-instrumentation/what-is-labwindows-cvi.html

[132] Bull, D. R. (2014). *Communicating Pictures: A Course in Image and Video Coding*. *Communicating Pictures: A Course in Image and Video Coding*. Elsevier Ltd. https://doi.org/10.1016/C2012-0-01327-0

[133] Bott, S. R. J. and Kirby, R. S. (2002). Avoidance and management of positive surgical margins before, during and after radical prostatectomy. *Prostate Cancer and Prostatic Diseases*, *5*(4), 252–263. https://doi.org/10.1038/sj.pcan.4500612

[134] Maloney, B. W., McClatchy, D. M., Pogue, B. W., Paulsen, K. D., Wells, W. A. and Barth Jr., R. J. (2018). Review of methods for intraoperative margin detection for breast conserving surgery. *Journal of Biomedical Optics*, *23*(10). https://doi.org/10.1117/1.JBO.23.10.100901

[135] Shah, A. K. (2018). Postoperative pathologic assessment of surgical margins in oral cancer: A contemporary review. *Journal of Oral and Maxillofacial Pathology*. Medknow Publications. https://doi.org/10.4103/jomfp.JOMFP_185_16

[136] Würth, C., Pauli, J., Lochmann, C., Spieles, M. and Resch-Genger, U. (2012). Integrating sphere setup for the traceable measurement of absolute photoluminescence quantum yields in the near infrared. *Analytical Chemistry*, *84*(3), 1345–1352. https://doi.org/10.1021/ac2021954

[137] Hong, G., Tabakman, S. M., Welsher, K., Chen, Z., Robinson, J. T., Dai, P. H., Wang, H. and Zhang, B. (2011). Near-Infrared Fluorescence Enhanced (NIR-FE) Molecular Imaging of Live Cells on Gold Substrates**, pp. 1–13. https://doi.org/10.1002/anie.201100934

[138] Peng, X., Chen, H., Draney, D. R., Volcheck, W., Schutz-Geschwender, A. and Olive, D. M. (2009). A nonfluorescent, broad-range quencher dye for Förster resonance energy transfer assays. *Analytical Biochemistry*, *388*(2), 220–228. https://doi.org/10.1016/j.ab.2009.02.024

[139] Philip, R., Penzkofer, A., Bäumler, W., Szeimies, R. M. and Abels, C. (1996). Absorption and fluorescence spectroscopic investigation of indocyanine green. *Journal of Photochemistry and Photobiology A: Chemistry*, *96*(1–3), 137–148. https://doi.org/10.1016/1010-6030(95)04292-X

[140] Stammes, M. A., Bugby, S. L., Porta, T., Pierzchalski, K., Devling, T., Otto, C., Dijkstra, J., Vahrmeijer, A. L., de Geus-Oei, L.-F. and Mieog, J. S. D. (2018). Modalities for image- and molecular-guided cancer surgery. *British Journal of Surgery*, *105*(2), e69–e83. https://doi.org/10.1002/bjs.10789

[141] Zemax. (no date). OpticStudio | Optical, Illumination & Laser System Design Software - Zemax. Retrieved January 1, 2018, from https://www.zemax.com/products/opticstudio

[142] Roithner Lasertechnik. (no date). Roithner Lasertechnik - High Power Single Chip LEDs, SMD LEDs. Retrieved January 1, 2018, from http://www.roithner-laser.com/led_highsingle_smd.html

[143] Ya Lee, V. (2017). *Organosilicon Compounds*.

[144] Luo, C., Zuo, J., Yuan, Y., Lin, X., Lin, F. and Zhao, J. (2015). Preparation and properties of a high refractive index optical resin prepared via click chemistry method. *Optical Materials Express*, *5*(3), 462. https://doi.org/10.1364/ome.5.000462

[145] Yang, S., Kim, J.-S., Jin, J., Kwak, S.-Y., and Bae, B.-S. (2010). Thermal Resistance of Cycloaliphatic Epoxy Hybrimer Based on Sol-Gel Derived Oligosiloxane for LED Encapsulation. *Journal of Applied Polymer Science*, *117*, 2140–2145. https://doi.org/10.1002/app.31702

[146] Roithner Lasertechnik. (no date). High Power Single Chip LEDs, SMD LEDs. Retrieved June 16, 2018, from http://www.roithner-laser.com/led_highsingle_smd.html

[147] RPMC Lasers Inc. (no date). Solid State Lasers and Laser Diodes from RPMC Lasers Inc. Retrieved June 16, 2018, from https://www.rpmclasers.com/

[148] Thorlabs. (2015). 0.39 NA TECS Hard-Clad, Step-Index, Multimode Fiber, 0–1.

[149] Edmund Optics. (no date). 2.5mm 2X, 100mm Length, Low NA Tapered Light Pipe. Retrieved June 16, 2018, from https://www.edmundoptics.eu/p/25mm-2x-100mm-length-low-na-tapered-light-pipe/20360/

[150] Thorlabs part# LA1085-B, N-BK7 Plano-Convex Lens, Ø18.0 mm, f = 30.0 mm, AR Coating: 650-1050 nm; www.thorlabs.com/thorproduct.cfm?partnumber=LA1085-B.

[151] Thorlabs part# LJ1821L1-B plano-cylindrical lens; 22 x 20 mm, f= 50 mm, AR Coating: 650-1050 nm; https://www.thorlabs.com/newgrouppage9.cfm?objectgroup_id=2798

[152] Thorlabs. (no date). C330TMD-B f = 3.1 mm, NA = 0.7, Mounted Aspheric Lens, ARC: 600 - 1050 nm. Retrieved January 1, 2019, from https://www.thorlabs.com/thorproduct.cfm?partnumber=C330TMD-B

[153] Thorlabs. (no date). A240TM-B f = 8.0 mm, NA = 0.5, Mounted Aspheric Lens, ARC: 650 - 1050 nm. Retrieved January 1, 2019, from https://www.thorlabs.com/thorproduct.cfm?partnumber=A240TM-B

[154] Budzyn, G. and Rzepka, J. (2008). Back-reflection effects in a frequency-stabilized two-mode He-Ne laser. *Optics Communications*, *281*(22), 5592–5595. https://doi.org/10.1016/j.optcom.2008.07.082

[155] Malacara-Hernández, D. and Malacara-Hernández, Z. (2013). *Handbook of Optical Design* (3rd ed.).

[156] Wynne, A., Frisch, J. R., Britten, C. and Walters, K. B. (2020). Synthesis, characterization, and stability of poly(ethylene-co-acrylic acid) films surface functionalized with fluorescent moieties. *Reactive and Functional Polymers*, *152*(March). https://doi.org/10.1016/j.reactfunctpolym.2020.104598

[157] Gaigalas, A. K., Li, L., Henderson, O., Vogt, R., Barr, J., Marti, G., Weaver, J. and Schwartz, A. (2001). The development of fluorescence intensity standards. *Journal of Research of the National Institute of Standards and Technology*, *106*(2), 381–389. https://doi.org/10.6028/jres.106.015

[158] Starlight Xpress Ltd. (2015). The TRIUS SX-825 mono CCD camera, (1).

[159] 50mm C Series VIS-NIR Fixed Focal Length Lens | Edmund Optics. (no date). Retrieved January 10, 2018, from https://www.edmundoptics.com/p/50mm-c-series-vis-nir-fixed-focal-length-lens/22385/

[160] LDX Optronics Inc. (2018). 730nm-885nm Laser Diodes – Free Space, (636), 63366.

[161] Laser 2000. (no date). FF01-780/12-25 - 780/12 nm BrightLine® single-band bandpass filter. Retrieved June 17, 2019, from https://www.laser2000.co.uk/product/ff01-780§12-25

[162] Semrock - Part Number: BLP01-785R-25. (no date). Retrieved July 16, 2018, from https://www.semrock.com/FilterDetails.aspx?id=BLP01-785R-25

[163] Erdogan, T. (2011). Semrock Optical Filters: Non-normal Angles of Incidence. Retrieved July 16, 2018, from: https://www.semrock.com/Data/Sites/1/semrockpdfs/nonnormalanglesofincidence.pdf

[164] Keshava, N. (2003). A Survey of Spectral Unmixing Algorithms. *Lincoln Laboratory Journal*, *14*(1), 55–78. https://doi.org/10.1109/LGRS.2014.2326555

[165] Barber, P., Vojnovic, B., Atkin, G., Daley, F. M., Everett, S. A., Wilson, G. D. and Gilbey, J. D. (2003). Applications of cost-effective spectral imaging microscopy in cancer research. *Journal of Physics D: Applied Physics*, *36*.

[166] Atkin, G., Barber, P. R., Vojnovic, B., Daley, F. M., Glynne-Jones, R. and Wilson, G. D. (2005). Correlation of spectral imaging and visual grading for the quantification of thymidylate synthase protein expression in rectal cancer. *Human Pathology*. https://doi.org/10.1016/j.humpath.2005.08.016

[167] Behrooz, A., Waterman, P., Vasquez, K. O., Meganck, J., Peterson, J. D., Faqir, I., & Kempner, J. (2017). Multispectral open-air intraoperative fluorescence imaging. *Optics Letters*, *42*(15), 2964. https://doi.org/10.1364/ol.42.002964

[168] Janesick, J.R., (2007). *Photon transfer*, San Jose: SPIE press.

[169] Bernardes, D. V, Martioli, E. and Rodrigues, C. V (2018) 'Characterization of the SPARC4 CCDs', *Publications of the Astronomical Society of the Pacific*, 130(991).

[170] Stemmer Imaging. (no date). FPN - Fixed Pattern Noise. Retrieved June 14, 2018, from https://www.stemmer-imaging.com/en-gb/knowledge-base/fpn-fixed-pattern- noise/

[171] Texas Instruments (2000) 'Noise analysis of FET transimpedance amplifiers', (1), pp. 1–6. Available at: http://www.ti.com/lit/an/sboa060/sboa060.pdf.

[172] Stephen B Alexander 'Optical communication receiver design' co-published by SPIE and IEEE, 1997, ISBN 0-8194-2023-9

[173] Piston, D. W. (1998). Concepts in Imaging and Microscopy. Choosing objective lenses: The importance of numerical aperture and magnification in digital optical microscopy. *Biological Bulletin*, *195*(1), 1–4. https://doi.org/10.2307/1542768

[174] Paschotta, R. (no date). Numerical Aperture. Retrieved February 16, 2018, from https://www.rp-photonics.com/numerical_aperture.html

[175] Edmund Optics. (no date). Understanding Optical Specifications. Retrieved July 15, 2018, from https://www.edmundoptics.co.uk/knowledge-center/application-notes/optics/understanding-optical-specifications/

[176] Lichtman, J. W. and Conchello, J. (2005). Fluorescence microscopy. *Nature Methods*, *2*(12). https://doi.org/10.1038/NMETH817

[177] Garini, Y., Young, I. T. and McNamara, G. (2006). Spectral imaging: Principles and applications. *Cytometry Part A*, *69*(8), 735–747. https://doi.org/10.1002/cyto.a.20311

[178] Spring, K. R., Fellers, T. J. and Davidson, M. W. (no date). Resolution and Contrast in Confocal Microscopy. Retrieved July 14, 2018, from http://www.olympusconfocal.com/theory/resolutionintro.html

[179] Markvart, T. (2008). The thermodynamics of optical étendue. *Journal of Optics A: Pure and Applied Optics*, *10*(1). https://doi.org/10.1088/1464-4258/10/01/015008

[180] Welford, W. T. and Winston, R. (1978). The Optics of Non-Imaging Concentrators (New York: Academic)

[181] Medical Design and Outsourcing. (no date). The Power of LEDs Inside Medical Devices. Retrieved July 16, 2018, from https://www.medicaldesignandoutsourcing.com/the-power-of-leds-inside-medical-devices/

[182] Wendt, M. and Andriesse, J. W. (2006). LEDs in real lighting applications: From niche markets to general lighting. *Conference Record - IAS Annual Meeting (IEEE Industry Applications Society)*, *5*(c), 2601–2603. https://doi.org/10.1109/IAS.2006.256905

[183] Bhardwaj, J., Peddada, R. and Spinger, B. (2016). Advances in LEDs for automotive applications. *Light-Emitting Diodes: Materials, Devices, and Applications for Solid State Lighting* XX, 976811. https://doi.org/10.1117/12.2214205

[184] Schubert, E. F. (2018). Light-Emitting Diodes (3rd ed.).

[185] Hobbs, P. C. D. (2008). *Building Electro-Optical Systems: Making It All Work. Journal of Petrology* (2nd ed.). Wiley.

[186] Ghafouri-shiraz, H. (2003). Principles Of Semiconductor Laser Diodes And Amplifiers: Analysis And Transmission Line Laser Modeling.

[187] Pawley, J. B. (2006). More Than You Ever Really Wanted to Know About Charge-Coupled Devices. In *Handbook of Biological Confocal Microscopy* (3rd ed., pp. 918–931). New York: Springer Science + Business Media.

[188] Mullikin, J. C., van Vliet, L. J., Netten, H., Boddeke, F. R., Van der Feltz, G. and Young, I. T. (1994). Methods for CCD camera characterization. *IS&T/SPIE 1994 International Symposium on Electronic Imaging: Science and Technology*, *2173*, 73–84.

[189] Oxford Instruments. (no date). CCD Architecture | Full Frame CCD, Frame Transfer and Interline CCD. Retrieved February 28, 2018, from https://andor.oxinst.com/learning/view/article/ccd-sensor-architectures

[190] Vickers, J. (no date). Sensor Technology Primer: CCD, CMOS.

[191] Denvir, D. J. (2005). Electron Multiplying CCDs. Retrieved from http://www.emccd.com/